# Improvement of XFOIL lift and drag predictions


## Waldu Oosthuizen

orcid.org/0000-0002-1686-540X


Dissertation accepted in fulfilment of the requirements for the degree Master of Engineering in Mechanical Engineering at the North-West University

| | |
|---|---|
| Supervisor: | Dr J.J. Bosman |
| Co-supervisor: | Mr D. Human |
| Assistant-supervisor: | Dr J-H. Kruger |

| | |
|---|---|
| Graduation: | June 2023 |
| Student number: | 24973564 |

# Abstract

XFOIL is a fast and relatively accurate panel method to analyse 2D airfoil performance. XFOIL has proven itself over many years to be a powerful airfoil design and analysis tool. From the literature and through the various study cases in this report, it is clear that XFOIL has a tendency to overpredict lift and underpredict drag in certain cases. This inaccuracy in predictions becomes increasingly apparent when analysing thick airfoils and increasing Reynolds numbers, where the effect of high and low angles of attack also need to be considered.

In this research, improvements have been made to XFOIL by incorporating an interactive vortex panel method to predict lift and drag in better agreement with experimental results. It should be noted that experimental data does not represent the absolute truth, but is merely an indication of common flight predictions that might contribute to understanding actual flight performance. The reason for inaccurate predictions lay within assumptions made to allow for quicker converging to final answers. These assumptions were studied and are discussed in this research. Proposed improvements to XFOIL, identified through the literature review, were then implemented and validated against experimental data obtained from literature.

The improvements under scrutiny were developed by Ramanujam and Ozdemir (2017) and Ramanujam, Ozdemir, and Hoeijmakers (2016) for another panel method software based on XFOIL, called RFOIL. RFOIL is also a vortex panel method that was derived from XFOIL but was developed to better predict the performance of wind turbine airfoils. The proposed method focuses on the integral momentum quantities and updates the model assumptions in the lift calculation. Ramanujam, Ozdemir, and Hoeijmakers (2016) had studied the boundary layer quantities' momentum and displacement thickness, as predicted by XFOIL and stated that an underprediction of the quantities is the cause of the drag underprediction of XFOIL. Ramanujam and Ozdemir (2017) found that XFOIL utilises the inviscid solution to obtain the results for a viscous analysis. A new approach was developed to remedy this overprediction of lift by updating the vorticity strengths.

These improvements showed good agreement with experimental data on RFOIL but they have not been tested on XFOIL. The goal of this report is to implement those improvements proposed for RFOIL, into XFOIL and to then validate them to study the improvements in both lift and drag predictions. As with RFOIL, the proposed improvements increased the accuracy of the predictions in accordance with experimental data, but an inaccuracy still exists with thick airfoils as XFOIL is not suited for such analyses. This will also be shown in this report.

Keywords: Panel method, lift prediction, drag prediction, Boundary Layer Theory, Integral Boundary Layer method, critical amplification ratio, Squire-Young model, Potential flow, Linear Stability Theory, viscous-inviscid coupling

# Declaration

I, **Waldu Oosthuizen**, hereby declare that

1. I understand what plagiarism is and am aware of the University's policy in this regard.
2. I know that "plagiarism" means using another person's work and ideas without acknowledgement, and pretending that it is one's own. I know that plagiarism not only includes verbatim copying, but also the extensive (albeit paraphrased) use of another person's ideas without acknowledgement. I know that plagiarism covers this sort of use of material found in textbooks, journal articles, theses AND on the internet.
3. "Improvement of XFOIL lift and drag predictions" submitted in the fulfilment in the requirement for the Master's degree in Mechanical Engineering (M Eng) is my own original work.
4. Where other people's work has been used (either from a printed source, Internet or any other source), this has been properly acknowledged and referenced in accordance with departmental requirements.
5. I have not used work previously produced by another student or any other person to hand in as my own.
6. I have not allowed, and will not allow, anyone to copy my work with the intention of passing it off as his or her own work.

_ _ _ _ _ _ _ _ _ _ _ _ _ _ _ _ _ _ _ _ _ _ _ _

STUDENT DATE

# Acknowledgements

I would like to thank my supervisor Dr Johan J. Bosman for the admirable guidance and support that he has given me throughout my time under his watchful eye. He was always more than happy to help and give clear guidance where it was requested. He was not only a great academic advisor but also gave me moral advice on how to tackle situations where I felt defeated.

Along with Dr Bosman's guidance I would also like to thank Mr Danie Human, team leader of the NWU Solar Car. It has been an honour to have such great leaders guiding me to my final destination. Academic and spiritual guidance from my supervisors was fundamental to the completion of my work.

I would also like to thank my parents for the loving support and motivation that kept me motivated and moving forward.

Lastly, I would like to take this opportunity to thank my Lord and Saviour and Heavenly Father for granting me this opportunity and appointing everyone who guided me through this process,

# Contents

# List of Figures

# List of Tables

# Nomenclature

**Acronyms and Abbreviations**

| | |
|---|---|
| $LE$ | Leading Edge |
| $TE$ | Trailing Edge |
| AoA | Angle of Attack |
| BEP | Best Efficiency Point |
| CAD | Computer Aided Design |
| NACA | National Advisory Committee for Aeronautics |
| RMS | Root-Mean-Square |

**List of Symbols**

| | | |
|---|---|---|
| $\Delta$ | Change in parameter | [-] |
| $\delta$ | Boundary Layer thickness | m |
| $\delta^*$ | Displacement thickness | m |
| $\Gamma$ | Total vorticity strength | - |
| $\gamma$ | Local vorticity strength | - |
| $\Lambda$ | Total source strength | - |
| $\lambda$ | Local source strength | - |
| $\mu$ | Dynamic viscosity | $N \cdot s/m^2$ |
| $\nabla$ | Gradient operator | [-] |
| $\tau_w$ | Shear stress at the surface wall | $\frac{kg}{ms^2}$ |
| $\theta$ | Momentum thickness | m |
| $\zeta$ | Vorticity | [-] |
| $C_d$ | Total drag coefficient | [-] |
| $c_d$ | Local drag coefficient | [-] |
| $C_f$ | Total skin friction coefficient | [-] |
| $c_f$ | Local skin friction coefficient | [-] |
| $C_l$ | Total lift coefficient | [-] |
| $c_l$ | Local lift coefficient | [-] |
| $C_p$ | Pressure coefficient | [-] |
| $H^*$ | Enegry shape factor | [-] |

| | | |
|---|---|---|
| $H_k$ | Kinetic shape factor | [-] |
| $M_e$ | Mach number at the boundary layer edge velocity | [-] |
| $N$ | Number of panels on airfoil contour | - |
| $N_w$ | Number of panels on wake contour | - |
| $N_{crit}$ | Amplification factor | [-] |
| $p$ | Absolute pressure | Pa |
| $Re$ | Reynolds number | $[-]$ |
| $u$, $V_x$ | x-component stream velocity | $m/s$ |
| $V$ | Velocity | $m/s$ |
| $v$, $V_x$ | y-component stream velocity | $m/s$ |
| $v_e, u_e$ | Boundary Layer edge velocity | m/s |
| $V_n$ | Normal velocity vector | m/s |
| $V_\infty, U_\infty$ | Free stream velocity | m/s |

**List of Subscripts**

| | |
|---|---|
| 0 | Original point condition |
| $\infty$ | Free stream conditions |
| e | Boundary layer edge conditions |
| w | Wall surface conditions |
| x=$\infty$ | At far point down stream condition |

# 1. Chapter 1: Introduction

## 1.1. Introduction

XFOIL (Drela, 1989) is an interactive linear vortex panel method that enables researchers to study and analyse two-dimensional airfoil performance and which is also capable of subsonic flow analysis. What makes XFOIL such a powerful airfoil design and analysis tool is that it is fast, and allows for the manipulation of airfoil geometry through an interactive mixed-inverse scheme. XFOIL is also able to predict the onset of laminar to turbulent transition through an envelope $e^n$-critical amplification factor, with good accuracy with respect to experimental data, and is also able to predict the separation bubble downstream of an airfoil with a significant reduction in computational time and with good accuracy. According to Drela (1989) the analysis formulation was embedded in an interactive driver, which allows the designer to exercise inverse solver and a geometry-manipulation facility that improves the productivity of the designer.

The numerical accuracy of XFOIL decays when certain flight conditions or simulated conditions are reached. At a high transitional Reynolds number the separation bubble becomes more apparent, and the onset of flow separation increases with the increase in Reynolds number. Under flow separation conditions the numerical flow analysis accuracy dramatically reduces because of the collapse of the Kutta condition. This is caused by the air flowing from the pressure side to the suction side at the trailing edge, resulting in a non-parallel flow at the trailing edge.

Additionally, XFOIL results become less accurate when the thickness of the airfoil increases. As mentioned earlier, XFOIL uses a vortex panel method to calculate airfoil performance. This method is accurate at predicting flow analysis on thin airfoils with a small trailing edge thickness. As airfoil thickness increases, the accuracy of XFOIL decreases. This is also due to the non-parallel flow condition at the trailing edge, and the same applies to the trailing edge thickness. These conditions are characteristic of interactive potential flow methods and they are a fundamental problem with them.

In the following sections it becomes clear that it is possible to manipulate XFOIL's code to increase the accuracy of the polar predictions as proposed by Ramanujam and Ozdemir (2017), and Ramanujam, Ozdemir, and Hoeijmakers (2016). For XFOIL to be as accurate as possible and eliminate complex calculations, some assumptions had to be made to reduce computation time and additional costs. The improved method focuses directly on these assumptions and finds a different method to approach the problem and improve on the accuracy of XFOIL. These improvements do add to the computational time, but relative to conventional CFD software, still result in a much faster analysis and design tool.

## 1.2. Research Problem

Although XFOIL is a fast and powerful tool, some inaccuracies in the prediction of lift and drag are present. The relevant literature shows that XFOIL is indeed an adequate design and analysis tool but it can be improved upon. The problem lies within the XFOIL coding and assumptions with boundary layer equations, more specifically in the momentum thickness

assumptions. Another factor that plays a role is the assumption concerning the trajectory of the wake.

The drag of an airfoil is calculated from the momentum conservation along the flow direction. Due to the no-slip condition on the airfoil surface, the free stream velocity is reduced to zero at the airfoil surface and becomes increasingly larger in the normal direction until the free stream velocity is reached ($0.99U_\infty$). This layer of varying velocity is known as the boundary layer and is an important concept when calculating drag, as this momentum deficit is directly related to the skin friction drag of the airfoil.

XFOIL incorporates the flat plate theory to each individual panel to model viscous effects over the panel. The flat plate theory has its own limitations that lead to inaccurate drag predictions. These limitations include the fact that along the flat plate no adverse pressure gradient is present, compared to an airfoil. One main difference is that for the flat plate theory the thickness of the plate is considered to be zero. This assumption thus reduces the overall computational time, but it is also a factor in the inaccurate prediction of drag as the edge velocity is overpredicted. Ramanujam, Ozdemir, and Hoeijmakers (2016) outlined that the method underpredicts the momentum thickness and in turn leads to an underprediction of the airfoil drag. A correction is then proposed to correct this underprediction of the momentum thickness in the wake.

The same goes for the wake trajectory, influencing lift predictions, where an inviscid wake trajectory is used to calculate the lift coefficient at a specified angle of attack, which is theoretically not correct. The inviscid wake will have less accurate predictions than a viscous wake as in general, viscous effects will decrease the lift produced by the airfoil and reduce the downwash of the air leaving the airfoil (Ramanujam and Ozdemir, 2017). This reduced downwash will change the wake trajectory and include the viscous effect of the flow. This was achieved by letting the resulting edge velocity update the vorticity strengths, as outlined in Ramanujam and Ozdemir (2017).

## 1.3. Research aim and objectives

The aim of this research is to apply changes to the XFOIL code to include the viscous wake trajectory and update the less accurate current boundary layer momentum thickness assumptions. The objectives of this research are;

- Through literature and documentation, to get a fundamental understanding of the XFOIL code as well as the applied theories and assumptions. This includes the studies done by Drela (1989) to give an overview of what theories and mathematical models were used to develop XFOIL.
- Complete a literature review on research aimed at improving the drag and lift predictions of XFOIL and also on research showing specific limitations of the code.
- Obtain reliable wind tunnel performance data for specific airfoils.
- Evaluate XFOIL standard drag and lift predictions against wind tunnel data. This will show the need for improvements, give some insight into what the possible causes for the inaccuracies are, and also the magnitude of the improvements that have to be made.
- Obtain a suitable computer operating system environment as well as a compatible Fortran compiler for easy modifications and compiling of the XFOIL code.
- At this stage the proposed modifications are implemented within the XFOIL code, both improved lift and drag predictions. The final objective is then to compare the newly

calculated XFOIL results of the selected airfoils against the obtained experimental data.

## 1.4. Research Method

First, the motivation for this research is shown by comparing the standard XFOIL predictions against the experimental airfoil performance data.

This was done by using the unedited version of XFOIL to perform a test condition simulation of the airfoils. A sensitivity test was completed beforehand to establish the correct number of panels required to obtain the highest order of accuracy. The $N_{crit}$ value was obtained from the experimental data and was also changed to meet the test conditions.

The proposed approaches by Ramanujam and Ozdemir (2017), and Ramanujam, Ozdemir, and Hoeijmakers (2016) were implemented into XFOIL and validated against experimental results. For this, it was necessary to make changes to the XFOIL source code and recompile the updated code. A Linux operating system (OS) was used to compile the XFOIL source code as it proved to be a simpler option to compile the XFOIL source codes than on Windows. A VirtualBox software program was installed which allowed one to install a separate operating system onto a host OS. The Linux OS, openSUSE, was installed onto the VirtualBox to allow for the compiling of the XFOIL source code on Windows host software. https://www.overleaf.com/project/61164a4aeb48fa2ffa536d97/detacher To verify whether the XFOIL on Linux was successfully installed and correctly compiled, a simple verification test was carried out using a NACA0012 airfoil. An aerodynamic performance analysis was carried out on the standard Windows OS XFOIL and on the non-improved version of the Linux OS version. These different versions were then compared and it was clear that the Linux version gave the same values as those obtained from the standard Windows OS version. Thus, from this simple verification test it was established that XFOIL was correctly compiled and installed on the Linux OS, when compared to the standard the Window OS XFOIL version.

After the previous stage had been accomplished, it was time to move on to the editing of the XFOIL files. Initially, the drag improvements were implemented, as they were the first obtained from the literature and they also seemed to be the easiest to be done. After that, the next step was to implement the proposed lift predictions. This improvement proved to be a more complex problem to solve; the reason for this will be explained in the following sections. As mentioned earlier, some changes had to be brought into the XFOIL coding; this was done during the implementation of the proposed improved lift predictions.

The next step was to validate these new lift and drag predictions against wind tunnel experimental data. The Linux OS XFOIL version was used to predict five airfoil aerodynamic performances, to analyse their improved lift and drag predictions. This study was only focused on the lift and drag predictions of XFOIL, therefore these values are of concern. A study was then done to analyse the values of these new predictions against the standard XFOIL predictions and against experimental data.

# 2. Chapter 2: Literature study

The focus of the literature survey is to understand the fundamental numerical model of XFOIL. It utilises a panel method that is derived from the potential flow theory and a stream function ($\psi$) is formulated to describe the flow around the airfoil. This function is fundamental to solving the flow conditions required to perform a flow analysis. From the literature, ways were investigated on how to solve this stream function, to obtain useful parameters. These parameters include the calculation of the vorticity strengths over the contour of the airfoil. To understand how the vorticity strengths are calculated is of great importance in calculating lift, as lift is an integral function of the vorticity strengths that are superimposed over the airfoil panels (the circulation theory of lift). Other important aspects of potential flow, which were later used throughout the code modification process, are discussed in this literature study.

The Drela (1989) articles proved to be of great importance as these were written to explain the XFOIL code and mathematical modelling of inviscid and viscous flow conditions. They also show the coupling of these two flow conditions to obtain a flow solution for an airfoil geometry. These articles also gave some insight into the transition prediction method, which is discussed later in this chapter.

From the literature, previous work done on vortex panel methods was identified and studied in detail. Two important studies that were obtained are the studies done by Ramanujam, Ozdemir, and Hoeijmakers (2016) and Ramanujam and Ozdemir (2017), who proposed an improvement to vortex panel methods' prediction of drag and lift. These research articles form the basis of the current work and more detail is given in the following chapters.

To add to the study, the transition prediction model is discussed where XFOIL utilises an envelope $e^n$-method. This transition prediction method is governed by the linear stability theory and implemented through the Orr-Somerfeld equations. This amplification factor value, $N_{crit}$, is used to account for wind tunnel quality and is a function of the turbulence intensity associated with each wind tunnel.

## 2.1. Potential flow

To apply potential flow to an airfoil, it is divided into a finite number of panels and placed inside a uniform flow field. Flow elements are then superimposed over the panel distribution of the airfoil. These flow elements are known as the source and vortex flows. A single stream function is then formed, as a summation of the flow elements, to calculate the influence of the uniform flow field and the source and vortex flows at an arbitrary point in the flow field around the airfoil.

In this section some basic incompressible potential flow theory has been studied to give an overview of how a panel method calculates different parameters, with a focus on the vorticity strengths. For a flow analysis of a two-dimensional viscous fluid, the properties of the fluid are solved for by the Navier - Stokes equations (Bongers, 2006).

$$\frac{\partial u}{\partial x} + \frac{\partial v}{\partial y} = 0 \tag{2.1}$$

$$\frac{\partial u}{\partial t} + u\frac{\partial u}{\partial x} + v\frac{\partial u}{\partial y} = \frac{1}{\rho}\frac{\partial p}{\partial x} + v(\frac{\partial^2 u}{\partial x^2} + \frac{\partial^2 u}{\partial y^2}) \tag{2.2}$$

$$\frac{\partial v}{\partial t} + u\frac{\partial v}{\partial x} + v\frac{\partial v}{\partial y} = \frac{1}{\rho}\frac{\partial p}{\partial y} + v(\frac{\partial^2 v}{\partial x^2} + \frac{\partial^2 v}{\partial y^2}) \tag{2.3}$$

Eqn. (2.2) and Eqn. (2.3) are known as the 'momentum' equations (Anderson, 2016) in their respective x and y direction of flow, while Eqn. (2.1) is known as the 'mass conservation' equation. These equations are complex to solve, but ways have been found to simplify this solution and break it down into a simpler form. Two main assumptions are that the flow should be irrotational and incompressible in nature.

### 2.1.1. Irrotational flow

The vorticity of flow is described as the curl of the velocity, defined in Eqn. (2.4),

$$\zeta = \nabla \times \vec{V} \tag{2.4}$$

For flow to satisfy the assumption of being irrotational, no vorticies should be present in the flow, thus vorticity must be zero (Anderson, 2016),

$$\nabla \times \vec{V} = 0 \tag{2.5}$$

from vector identity one recalls that the curl of the gradient of a scalar ($\psi$) is equal to zero,

$$\nabla \times \nabla\psi = 0 \tag{2.6}$$

One can finally obtain a solution of $\vec{V}$ with the irrotational flow assumption and the vector identity.

$$\vec{V} = \nabla\psi \tag{2.7}$$

with,

$$u = \frac{\partial \psi}{\partial x}, v = \frac{\partial \psi}{\partial y}, v_n = \frac{\partial \psi}{\partial n} \tag{2.8}$$

The above equations make it possible to calculate the velocity of the airflow in the x, y and normal direction. XFOIL uses the normal velocity definition, that is a derivative of the stream function in the normal direction, to calculate the vorticity strengths.

### 2.1.2. Incompressible flow

For flow to be considered incompressible means that throughout the process the density of the fluid is constant and does not change with time (Anderson, 2016).

$$\frac{\partial p}{\partial t} + \nabla \cdot (\rho\vec{V}) = 0 \tag{2.9}$$

Thus, it seems that the solution to Eqn. (2.9) with a constant density, $\rho$. simplifies the equation to Eqn. (2.10), the incompressible mass conservation.

$$\nabla \cdot \vec{V} = 0 \tag{2.10}$$

The solution to the velocity potential is obtained by Laplace's equation, which is obtained by substituting Eqn. (2.7) into the incompressible mass conservation equation.

$$\nabla^2 \psi = 0 \tag{2.11}$$

With it now being possible to solve for the velocity potential, we can then calculate velocity with Eqn. (2.7) and Eqn. (2.8). Eqn. (2.11) is also a linear equation. This means that one can utilise the principle of superposition to account for different elementary flow solutions.

### 2.1.3. Uniform flow

A condition of uniform flow is set in XFOIL for the free stream and is incorporated within the stream function to account for the effects of the free stream on the airfoil. This flow element is represented by flow lines that are parallel to one another and can change flow direction, at an angle $\alpha$, known as the angle of attack. At each point of a two-dimensional velocity field, the magnitude of the velocity field and the direction are constant throughout all the points of the flow field (Anderson, 2016). One first has to derive a stream function to describe the uniform flow mathematically for analysis purposes. This is done by writing the x and y components of the uniform flow at an angle of attack.

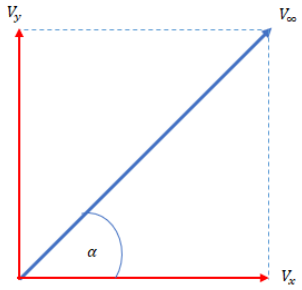


**Figure 2.1.** Free stream velocity vector with x and y components

With $V_x = V_\infty \cos(\alpha)$ and $V_y = V_\infty \sin(\alpha)$. To obtain the uniform flow stream function, one must integrate $\vec{V} = \nabla \psi_u$ (Anderson, 2016). After integration has been completed Eqn. (2.12) is obtained, known as the uniform flow stream function element.

$$\psi_u = V_\infty cos(\alpha)x + V_\infty sin(\alpha)y \tag{2.12}$$

### 2.1.4. Source/Sink flow

A sink or source flow is represented as an infinitesimal small point, in a velocity flow field, from which mass flows radiate outward in the case of a source point, and inward in the case of a sink flow (Anderson, 2016). In XFOIL, the source flow is superimposed over the airfoil and wake panels. The outward flow effect of the source represents the displacement effect of the boundary layer in the flow.

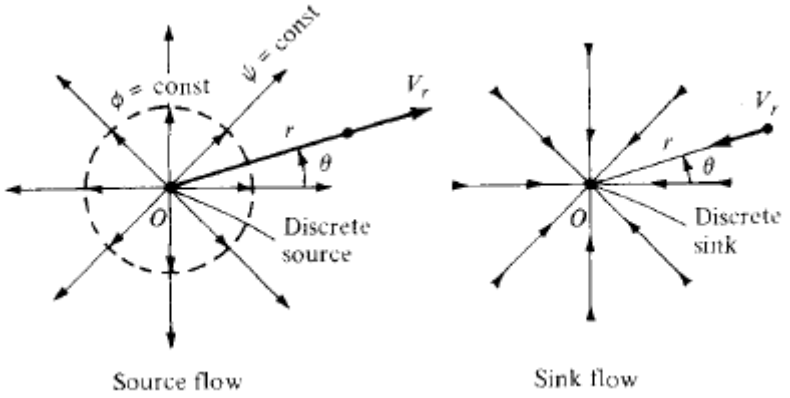


**Figure 2.2.** Sink/Source representation (Anderson, 2016)

To derive the sink/source flow requires the same method, only the direction of flow is different where it is modelled as a + or − sign to indicate sink or source flow. First, it is important to recognise that the source/sink strength is given as, $\Lambda$. The stream function for a source flow is given in Eqn. (2.13). (The sink flow only has a negative sign as mass is subtracted from the flow field.)

$$\psi_s = \frac{\Lambda}{2\pi} \ln (r_p) \tag{2.13}$$

The symbol $r_p$ is important to notice as this is the distance between the source/sink position, $O(x_0; y_0)$ to an arbitrary point $P(x_p; y_p)$. If we use Pythagoras' theorem, we can then derive an equation for the values $r_p$.

$$r_p = ((x_p - x_0)^2 + (y_p - y_0)^2)^{\frac{1}{2}} \tag{2.14}$$

It should be noted that for $V_r = \frac{\Lambda}{2\pi r}$ and for $V_\theta = 0$. To derive the velocity components one derives Eqn. (2.13) and substitutes Eqn. (2.14) into the same equation, we obtain,

$$V_x = \frac{\Lambda(x_p - x_0)}{2\pi r_p^2} \tag{2.15}$$

$$V_y = \frac{\Lambda(y_p - y_0)}{2\pi r_p^2} \tag{2.16}$$

### 2.1.5. Vortex

Another panel-imposed flow element is the vortex flow element. For an airfoil to generate lift, circulation of the flow is required. To accomplish this, XFOIL imposes vortex flows on the node points of all the panels across the airfoil. This allows for the circulation of air around the airfoil and lift is then virtually generated in the process. In XFOIL, the vorticity strengths differ panel to panel in a linear way, hence the name 'linear vortex panel' method.

Vortex flow in a flow field is represented by a circular flow of a fluid around a infinitesimally small point (Anderson, 2016). The vorticity strength is given as, $\Gamma$, and the potential flow of a vortex is given as,

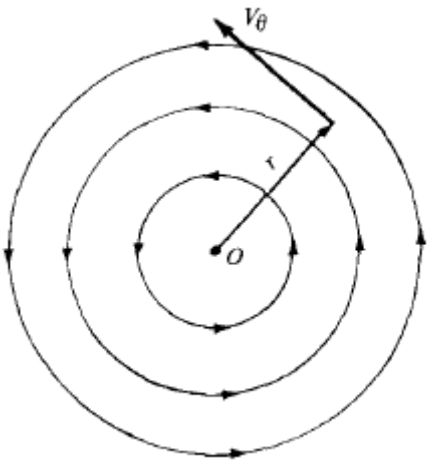


**Figure 2.3.** Vortex representation (Anderson, 2016)

$$\psi_v = -\frac{\Gamma}{2\pi}\theta \tag{2.17}$$

The derivation of the velocity components are complex and extensive, therefore, only a brief description of how to obtain them is shown with the final solution given in the end. First, to obtain the x and y components of the velocity the derivative of the potential flow of a vortex in respect of the x and y components (Anderson, 2016), that is, $\frac{\partial \psi_v}{\partial x}$ and $\frac{\partial \psi_v}{\partial y}$, is taken.

The angle $\theta$ is described in the following figure, that is the angle between the horizontal y axis and the arbitrary point $(x_p; y_p)$. After derivation we obtain the following equations,

$$V_x = \frac{\Gamma(y - y_0)}{2\pi r^2} \tag{2.18}$$

$$V_y = \frac{\Gamma(x - x_0)}{2\pi r^2} \tag{2.19}$$

### 2.1.6. Panelling with source and vortex flows

The mathematical model of a smooth curve that has been broken up into $N$ number of panels with superimposed potential flow elements is discussed. In this section the derivation of the total source and vortex strengths over the airfoil contour is outlined at an arbitrary point in the flow field. This part extends up to the end on how the vorticity strengths are calculated with panel methods. It is possible to write a potential flow equation for a arbitrary point under the influence of multiple sources and vortexes. In the case of XFOIL, multiple sources and vorticies over the airfoil contour are superimposed upon each panel. The reason for this is that the displacement effect, due to the boundary layer, is represented by the potential source flow (Drela, 1989). This means that the source and vortex distribution follows a curve that can be divided into $N$ number of panels.

With the principle of superposition, you are able to account for all the sources and vortexes over the airfoil contour, $ds$. So, for an arbitrary point $P(x_p; y_p)$ at distance $r_{p_j}(s_j)$ of panel $S_j$ under the influence of multiple potential source and vortex flows, $\psi_s$ and $\psi_v$ respectively, we are able to find the potential flow function of this velocity field. A summation of the flow elements that

has been superimposed onto the airfoil contour, is required to account for all these influences on the panels (Anderson, 2016).

$$\psi_s = \Sigma_{j=1}^{N} \frac{\lambda_j}{2\pi} \int_j \ln r_{pj} ds_j \tag{2.20}$$

$$\psi_v = \Sigma_{j=1}^{N} \frac{\gamma_j}{2\pi} \int_j \theta_j ds_j \tag{2.21}$$

### 2.1.7. Calculation of the vorticity strengths

Consider Fig. 2.6, an airfoil divided into $N$ number of panels, that is placed within a uniform velocity flow field with an angle of attack of $\alpha$. The stream function, $\psi$, can then be written as a summation of all the flow elements present. Eqn. (2.22) shows the stream function for this case.

$$\psi = V_\infty x + V_\infty y + \Sigma_{j=1}^{N} \frac{\lambda_j}{2\pi} \int_j \ln r_{pj} ds_j + \Sigma_{j=1}^{N} \frac{\gamma_j}{2\pi} \int_j \theta_j ds_j \tag{2.22}$$

Important to note is that the second term, the source term, has a constant magnitude over a panel, but varies from panel to panel. Also, in this case the vorticity strengths are constant and do not vary from panel to panel. XFOIL assumes a linear vorticity, in which the vorticity strengths vary from panel to panel in a linear way. The differences between these approaches do add to the complexity, but similar matrices are used to calculate the vortex strengths.

It should be noted that the medium through which the airfoil is moving, does not pass through the solid body, but flows over the airfoil surface. This constraint is not only realistic, but it also enables the calculation of the vorticity strengths. To avoid the mass flowing through the panels a constraint is required to prohibit this. In Anderson (2016) you can find Eqn. (2.23), that explains this constraint.

$$\vec{V} \cdot \hat{n} = V_n = 0 \tag{2.23}$$

With this equation it is possible to derive an equation from the stream function to solve for the vorticity strengths by taking the derivative of the stream function with respect to the normal component at each panel and setting it equal to zero as in Eqn. (2.24) (as no mass flows through the body).

$$V_n = \frac{\partial \psi}{\partial n} = 0 \tag{2.24}$$

one can the rewrite Eqn. (2.22) as an expression for the normal velocity on panel $i$.

$$V_{n,i} = V_\infty x_i + V_\infty y_i + \Sigma_{j=1}^{N} \frac{\lambda_j}{2\pi} \int_j \frac{\partial}{\partial n_i} \ln r_{ij} ds_j + \Sigma_{j=1}^{N} \frac{-\gamma}{2\pi} \int_j \frac{\partial \theta_{ij}}{\partial n_i} ds_j = 0 \tag{2.25}$$

The integral terms of both the source and vortex distributions are known as the geometric integrals and can be written as (Anderson, 2016),

$$I_{ij} = \int_j \frac{\partial}{\partial n_i} \ln r_{ij} ds_j \tag{2.26}$$

$$K_{ij} = \int_j \frac{\partial \theta_{ij}}{\partial n_i} ds_j \tag{2.27}$$

This Eqn. (2.25) with Eqn. (2.26) and Eqn. (2.27), can now be rewritten as Eqn. (2.28),

$$V_{n,i} = V_\infty x_i + V_\infty y_i + \frac{\lambda_i}{2} + \Sigma_{j=1,j\neq 1}^{N} \frac{\lambda_i I_{ij}}{2\pi} + \Sigma_{j=1,j\neq 1}^{N} \frac{-\gamma K_{ij}}{2\pi} = 0 \tag{2.28}$$

This equation can then be solved to obtain the solutions of the vorticity strengths.

#### The Kutta condition

The Kutta condition is fundamental to the potential flow as it prohibits the movement of the stagnation point at the trailing edge. The Kutta condition enforces a restriction to stop the air from moving from the pressure side to the suction side at the trailing edge. This condition only allows for air to leave the trailing edge of an airfoil parallel to one another, avoiding the unnatural flow of air curling over from the pressure side to the suction side at the trailing edge (Schlichting et al., 2003).

$$V_{t,N} + V_{t,1} = 0 \tag{2.29}$$

The system of equations in Eqn. (2.28) and Eqn. (2.29) are solved simultaneously in a matrix of $A\mathbf{x} = b$ configuration. Matrix $A$ in this case is known as the influence matrix and matrix $b$ is the effect of the uniform potential flow, $V_\infty x + V_\infty y$. Matrix $\mathbf{x}$ will be solved for, containing the solution to the source strengths and vorticity strengths

$$A = \begin{bmatrix} I_{ij}, \\ J_{ij}, \\ K_{ij}, \\ L_{ij} \end{bmatrix}, x = \begin{bmatrix} \lambda_j \\ \gamma \end{bmatrix}, b = \begin{bmatrix} V_\infty x_i + V_\infty y_i \end{bmatrix} \tag{2.30}$$

This matrix is solved with a full Newton method to obtain the vorticity strengths and source strengths and is standard to all potential flow calculations. As mentioned, the difference between this panel method and a linear vortex panel method is that the assumption was that the vortexes are constant and do not vary from panel to panel.

## 2.2. Boundary layer theory

The flat plate theory lays the basis for some of XFOIL's mathematical modelling. The Boundary Layer Theory was studied to give insight into the fundamental assumptions surrounding it. Fig. 2.4 illustrates the case of air flowing uniformly from the right and flow over the surface of the plate. An interaction is observed between the viscous air and the surface of the plate. This interaction arises from the shear stress present in the flow due to the presence of the wall, described by Eqn. (2.31), (Schlichting et al., 2003).

$$\tau_w = \mu \left( \frac{\partial u}{\partial y} \right)_w \tag{2.31}$$

This shear stress between the solid body and the fluid is caused by the "*no-slip*" condition on the surface of the plate. It is because of this condition that the air at the surface of the plate

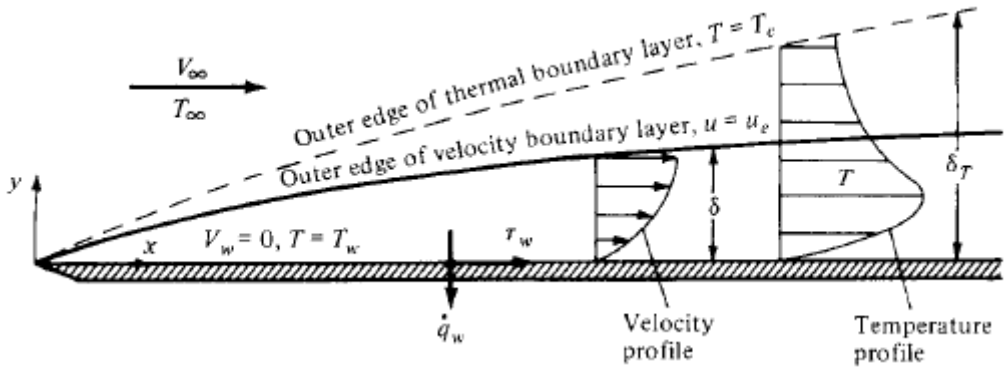


**Figure 2.4.** Boundary layer over a flat plate (Schlichting et al., 2003)

and the air adjacent to the surface have a zero velocity (the no-slip condition). As one moves upward, normal to the plate surface, the air velocity increases until it is equal to the free stream velocity. The deficit in mass flow from $y = 0$ where $v = 0$, up to where the layer edge velocity $v_e = 0.99V_\infty$, is known as the *Boundary Layer* that is formed over the surface (Schlichting et al., 2003). For the flat plate theory there is no adverse pressure gradient over the plate. This is due to the fact that the angle of attack of the flow is zero and the plate has a thickness that is considered to be zero with the edge velocity $v_e = V_\infty$. According to Anderson (2016), the edge velocity of the boundary layer of an object moving through a fluid, is obtained from the inviscid flow solution.

### 2.2.1. Boundary layer thickness

The first property of the boundary layer under discussion, is the velocity boundary layer thickness, $\delta$, which increases at each point along the $x$-direction. As explained earlier, a velocity profile is observed within the boundary layer. This profile varies from point to point in the $x$-direction. The variation falls between, $y = 0$ at the surface of the plate up to $y = \delta$ at the edge of the boundary layer. This velocity profile is defined as $v = v(y)$, according to Anderson (2016). This can also be seen in Fig. 2.4.

Blasius (1907) set out to simplify the Navier-Stokes equations to allow for the calculation of the boundary layer thickness of an incompressible laminar flow over a flat plate and obtained the following expression for the boundary layer thickness,

$$\delta = \frac{5x}{\sqrt{Re_x}} \tag{2.32}$$

One can find this equation in Schlichting et al. (2003). This equation was derived on the assumption that $\delta << c$, with $c$ being the chord length of the airfoil. Anderson (2016) also stated that the laminar boundary layer over a flat plate grows parabolically with increasing distance from the leading edge.

### 2.2.2. Displacement thickness

The displacement thickness is defined as the distance at which the air flowing parallel to the wall is displaced outward due to the development of the boundary layer. The physical interpretation of this property, according to Anderson (2016), is shown in Fig. 2.5. In a flow case with inviscid flow (left-hand side of Fig. 2.5), the streamline is parallel to the flow, and no displacement of

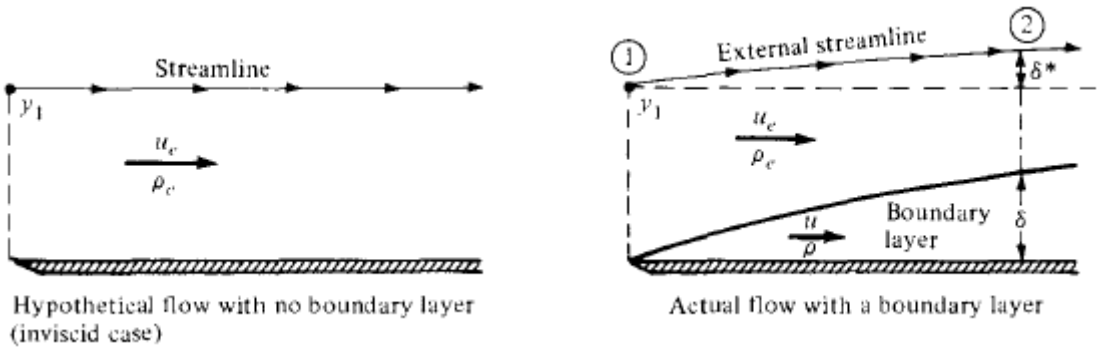


**Figure 2.5.** Displacement external flow streamline due to the presence of the boundary layer (Anderson, 2016).

this line is observed as the flow does not interact with the wall surface. On the right-hand side of Fig. 2.5, a viscous fluid is observed flowing over the wall surface also an interaction between the fluid and the plate. Schlichting et al. (2003) and Anderson (2016) stated that this decrease in velocity flow in the boundary layer acts as a obstruction to the incoming free stream flow, thus the free stream air is displaced, as shown in Fig. 2.5. This also leads to the displacement of the previously mentioned streamline, effectively giving rise to the concept of the *effective body*.

The definition of the displacement thickness, in terms of Fig. 2.5 is given by Eqn. (2.33)(Schlichting et al., 2003 and Anderson, 2016),

$$\delta^* = \int_0^{y_1} \left(1 - \frac{\rho v}{\rho_e v_e}\right) dy \tag{2.33}$$

According to Anderson (2016) the free stream does not see the surface of the body, but sees the effective body of the surface. Therefore, in order to obtain $\rho_e$, $v_e$, at the edge of the boundary layer, on the actual body, one must carry out an inviscid flow solution. Anderson (2016) also stated that to solve for $\delta^*$ you need the profiles of $v$ and $\rho$ from the boundary layer flow solution, but $\rho_e$ and $v_e$ are dependent on the displacement thickness and this leads to an iterative solution. In addition, Anderson (2016) gives an outline of the procedure on how to accurately determine the displacement thickness. A brief description is given:

1. Evaluate the properties $\rho_e$ and $v_e$ of the inviscid solution of the actual body.
2. With the above properties one must then solve the boundary layer equations at each point on the airfoil contour.
3. Now you are able to calculate $\delta^*$ with Eqn. (2.33). Anderson (2016) warns that this is not an accurate estimation of the displacement thickness. The reason for this is that this property is evaluated from the actual curve and not from the effective body's curve. This displacement thickness will function as an intermediate effective body, to calculate the new effective body.
4. A new inviscid solution is carried out on this intermediate $\delta^*$ to obtain new values of $\rho_e$ and $v_e$.
5. Repeat steps 2 to 4 until a converged solution is obtained.

   This procedure is different from how XFOIL models the boundary layer. A transpiration model is used for inviscid/viscid modelling of the boundary layer, which is a non-physical

boundary condition since it adds mass in the system to simulate the boundary layer Smith et al. (2011).

### 2.2.3. Momentum thickness

Momentum thickness, $\theta$, is an index that is proportional to the deficit in mass momentum due to the presence of the boundary layer (Anderson, 2016). He continued by saying that this height is described as a hypothetical stream which carries the deficit momentum flow at free stream conditions. The momentum thickness, $\theta$, is defined in Eqn. (2.34),

$$\theta = \int_0^{y_1} \frac{\rho v}{\rho_e v_e} \left(1 - \frac{v}{v_e}\right) dy \tag{2.34}$$

According to Schlichting et al. (2003) the momentum thickness, $\theta$, is directly proportional to the skin friction drag coefficient from the leading edge to the trailing edge, over the chord of an airfoil and can be defined as,

$$\theta \propto \frac{1}{c} \int_0^c (c_f)\, dx = C_f \tag{2.35}$$

## 2.3. Linear Stability Theory

According to Bongers (2006), the linear stability theory provides a way to predict the natural growth of disturbances in a laminar boundary layer. Tollmien (1930), Schlichting et al. (2003) and others, were the developers of this theory that considers a laminar boundary layer under small superimposed disturbances. In 1936 Ingram (1936) found that turbulence, present within the free stream, played a role in the laminar to turbulent transition. The author stated this is due to the fluctuation in the boundary layer that causes local flow separations. This is followed by the transition from laminar to a turbulent boundary layer. Bongers (2006) also stated that in flows where transition is dominated by the Tollmien Schlichting waves, this linear growth plays a role in the transition of the boundary layer (Tollmien, 1930, Schlichting et al., 2003). The basis of the linear stability theory is the Orr-Somerfeld Eqn. (2.36) equation, which has been derived from the Navier-Stokes equations with parameters of fluctuations.

$$(\overline{u} - \overline{c})\left[\psi'' - \alpha_*^2 \psi\right] - \overline{u}'' = \frac{-i}{\alpha_* Re_\theta}[\psi'''' - 2\alpha_*^2 \psi'' + \alpha_*^4 \psi] \tag{2.36}$$

With $\overline{U} = \frac{u}{U}$, $\overline{c} = \frac{c}{U}$ and $\alpha_* = \overline{\alpha}\theta$.

In terms of XFOIL, this theory is used to track the natural growth of disturbances in the boundary layer. After XFOIL is able to track the highest growth of the disturbances, transition is most likely to occur in this location.

### 2.3.1. The critical amplification ratio, $e^N$, method

The $A = A_0$ criterion of wave amplification was developed as a way to measure the amplification of the disturbances, with $A_0$ defined as the unknown initial amplitude of the wave at $x_0$ and with $A$ known as the wave amplitude, as explained by Bongers (2006).

As a solution to the Orr-Somerfled equation, Eqn. (2.36), the value of spatial growth rate ,$-\alpha_i$, is obtained. This value gives insight into the state of the waves and determines the amplification

or damping of the waves. An equation for the amplification ratio can now be derived to organise and manage the growth of decay rate of amplification. This equation is defined as,

$$\frac{A}{A_0} = e^{N_{crit}}; \qquad N_{crit} = \int_{x_0}^{x} (-\alpha_i) dx \tag{2.37}$$

One can now write Eqn. (2.37) in a non-dimensionalised form, as Bongers (2006) explained,

$$N_{crit} = \frac{1}{\nu} \int_{\frac{x_0}{c}}^{\frac{x}{c}} (Tv) dx; \qquad T = \frac{-\alpha_i \theta}{Re_\theta} \tag{2.38}$$

In order to calculate the amplification rate, $T$, with the $e^{N_{crit}}$, the stability diagrams for the specific velocity profile must be known. As a final note, the $N_{crit}$ value is dependent on the free stream flow turbulence associated with the quality of wind tunnel airflow, and not an arbitrary number. According to Bongers (2006), it should be treated as a factor to bring experiments and theory into agreement. In other words, the flow conditions within the potential uniform flow is assumed to be laminar which is not the case for wind tunnels where the airflow experiences some level of turbulence. This is reflected in the measured turbulence intensity of a wind tunnel. This phenomenon can have effects on the boundary layer as premature transition is characterised by an increase in the turbulence intensity. By correlating the amplification factor to the wind tunnel turbulence intensity one can account for the effects of a turbulence level in a uniform flow. The reason is to ensure reliability of the theoretical results.

## 2.4. XFOIL

In the article by Drela (1989), the developer discussed the mathematical modelling of XFOIL and provided an extensive and detailed explanation. As mentioned previously, XFOIL is a software that uses a linear-vorticity panel method. This means that the vorticity strength varies from panel to panel in a linear way with a Karman-Tsien compressibility correction incorporated (this correction breaks down when entering sonic conditions), allowing compressible predictions. Source and vortex distributions are superimposed on each panel node of the airfoil with only a source distribution on the wake. The source distributions on the airfoil and wake allow for the modelling of viscous effects on the uniform potential flow. The displacement of the inviscid flow is then used to model the boundary layer with a wall transpiration condition which couples the viscid flow with the inviscid flow Smith et al. (2011). The boundary layer and wake effects are described by a two-equation lagged dissipation integral with an envelope $e^n$ transition criterion to determine the transition point. The boundary layer and transition (viscous) equations are then solved simultaneously with the potential flow (inviscid) equations and allowed to converge to a final solution through a full Newton method.

### 2.4.1. Inviscid formulation

A two-dimensional inviscid flow field is constructed and together with the vortex and source distributions that are present on the airfoil contour, the following stream function is obtained for an arbitrary point in the flow field (Drela, 1989),

$$\psi(x,y) = u_\infty y + v_\infty x + \frac{1}{2\pi} \int \gamma(s) \ln r(s,x,y) ds + \frac{1}{2\pi} \int \sigma(s) \theta(s,x,y) ds \tag{2.39}$$

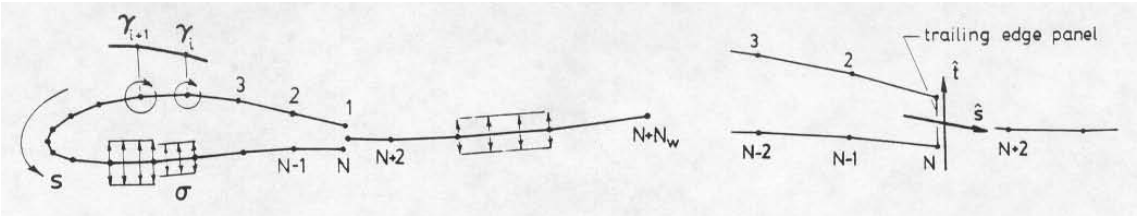


**Figure 2.6.** XFOIL panelling with superimposed source and vortex distributions (Drela, 1989)

where s is the coordinates along the vortex and source sheet, r is the magnitude of the vector from s to the point (x,y), $\theta$ is the angle of r, with $u_\infty = q_\infty \cos\alpha$ and $v_\infty = q_\infty \sin\alpha$ as the free stream velocity components. The airfoil and wake are then discretised into $N$ panel nodes of the airfoil and $N_w$ panel node points on the wake. Each panel node on the airfoil has a linear vorticity distribution defined as $\gamma_i (1 < i < N)$ ) and a source distribution on the airfoil and wake, defined as $\sigma_i (1 < i < N + N_w + 1)$ associated with it. The source strength will then be calculated and related to the viscous layer quantities through the source-influence matrix.

On the right-hand side of Fig. 2.6, the trailing edge source and vortex strength can be seen, with $\hat{s}$, the unit vector, bisecting the trailing edge and $\hat{t}$ the unit vector along the trailing edge. Drela (1989) also incorporated the uniform source strength, $\sigma_{TE}$, and vortex strength, $\gamma_{TE}$, to the trailing edge gap. He then defined these equations as,

$$\sigma_{TE} = \frac{1}{2}(\gamma_1 - \gamma_N)|\hat{s} \times \hat{t}| \qquad \gamma_{TE} = \frac{1}{2}(\gamma_1 - \gamma_N)|\hat{s} \cdot \hat{t}| \tag{2.40}$$

From Fig. 2.6 it is clear that $\hat{s}$ is bisecting trailing edge unit vector angle and unit vector $\hat{t}$ is tangential to the trailing edge surface. With this information and with Eqn. (2.39), the following expression for the stream-function is obtained by Drela (1989),

$$\begin{aligned}\psi(x,y) = u_\infty y + v_\infty x + \frac{1}{4\pi}\sum_{j=1}^{N+N_w+1} \psi_j^\sigma(x,y) 2\sigma_j \\ + \frac{1}{4\pi}\sum_{j=1}^{N-1} \psi_j^{\gamma+}(x,y)(\gamma_{j+1} + \gamma_j) + \psi_j^{\gamma-}(x,y)(\gamma_{j+1} - \gamma_j) \\ + \frac{1}{4\pi}(\psi_N^\sigma(x,y)|\hat{s} \times \hat{t}| + \psi_N^{\gamma-}(x,y)|\hat{s} \cdot \hat{t}|(\gamma_1 - \gamma_N)\end{aligned} \tag{2.41}$$

Fig. 2.7 shows Eqn. (2.39) in terms of local panel coordinates $\bar{x}$ - $\bar{y}$ and from Fig. 2.7, Eqn. (2.42) to Eqn. (2.44) can be defined,

$$\psi_j^{\gamma+}(x,y) = \bar{x}_1 \ln r_1 - \bar{x}_2 - \bar{x}_1 + \bar{y}(\theta_1 - \theta_2) \tag{2.42}$$

$$\psi^{\gamma-}(x,y) = [(\bar{x}_1 + \bar{x}_2)\psi_j^{\gamma+} + r_2^2 \ln r_2 - r_1^2 \ln r_1 + \frac{1}{2}\bar{x}_1 - \bar{x}_2^2)]\frac{1}{\bar{x}_1 - \bar{x}_2^2} \tag{2.43}$$

$$\psi_j^\sigma(x,y) = \bar{x}_2\theta_2 - \bar{x}_1\theta_1 + \bar{y}\ln\frac{r_1}{r_2} \tag{2.44}$$

The following system of equations is the result of requiring that the stream-function be equal to some constant $\psi_0$ at each node of the airfoil (Drela, 1989),

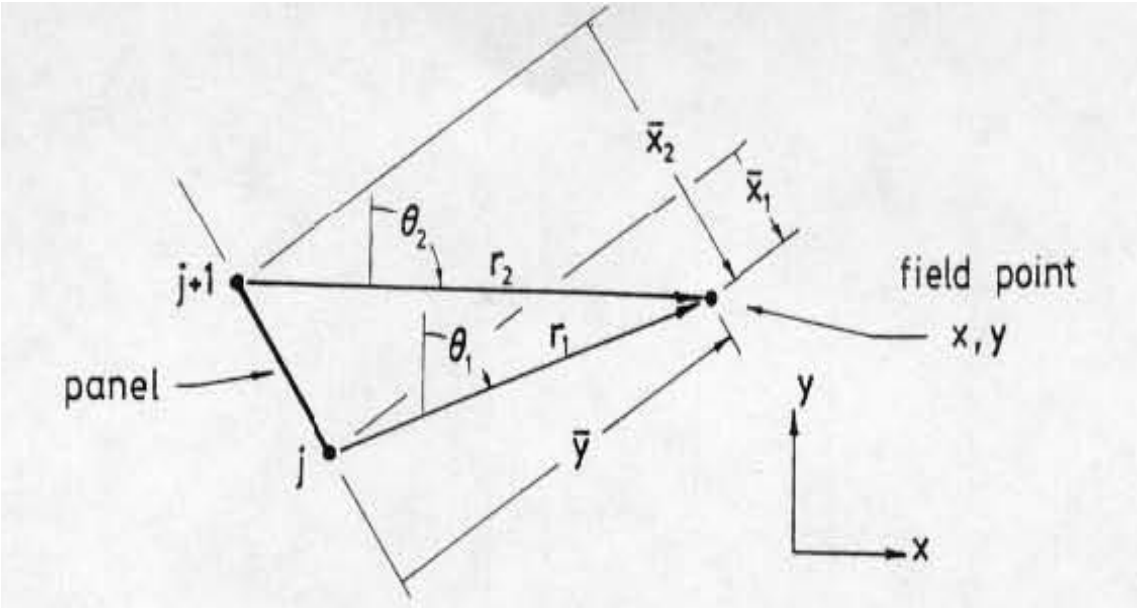


**Figure 2.7.** Local panel coordinates (Drela, 1989)

$$\sum_{j=1}^{N} a_{ij}\gamma_{ij} - \psi_0 = -u_\infty y_i + v_\infty x_i - \sum_{j=1}^{N+N_w+1} b_{ij}\sigma_{ij} \qquad 1 \leqslant i \leqslant N \tag{2.45}$$

The matrices $a_{ij}$ and $b_{ij}$ are determined from the unit stream functions (Eqn. (2.42) to Eqn. (2.44)) if all the airfoil panel nodes $x_i$,$y_i$ and the wake nodes are known, according to (Drela, 1989). Eqn. (2.45), together with the Kutta condition,

$$\gamma_1 + \gamma_N = 0 \tag{2.46}$$

yields a linear (N+1) x (N+1) system of equations for the N node values $\gamma_i$ and the airfoil surface stream function, $\psi_0$ Drela (1989). If an analysis is performed with known geometry this system of equations from Eqn. (2.45) and the Kutta condition, Eqn. (2.46), can readily be solved by Gaussian elimination. This then gives the solution to the airfoil surface vorticity values as (Drela, 1989),

$$\gamma_i = cos\alpha\gamma_{0i} + sin\alpha\gamma_{90i} + \sum_{j=1}^{N+N_w-1} b'_{\sigma_j} \qquad 1 \leqslant i \leqslant N \tag{2.47}$$

where $\gamma_0$ and $\gamma_9 0$ are the vortex distributions corresponding to a free-stream angle of attack of 0° and 90° and with $b'_{ij} = \frac{b_{ij}}{a_{ij}}$ as the source-influence matrix. From Eqn. (2.47) when setting $\sigma = 0$ an inviscid solution is obtained at a specified angle of attack. With viscous calculations, the source strength is known, so Eqn. (2.47) should be augmented with the boundary layer equations to obtain a solvable closed system (Drela, 1989).

To avoid the problem with a sharp trailing edge, where the $i = 1$ and $i = N$ coincide, Eqn. (2.45), where $i = N$, is replaced with,

$$(\gamma_3 - 2\gamma_2 + \gamma_1) - (\gamma_{N-2} - 2\gamma_{N-1} + \gamma_N) = 0 \tag{2.48}$$

### 2.4.2. Viscous formulation

Drela (1989) implemented the standard compressible integral momentum and kinetic energy shape parameter equation for the viscous formulation, along the streamwise direction, $\zeta$. These equations are defined as,

$$\frac{d\theta}{d\zeta} + (2 + H - M_e)\frac{\theta}{u_e}\frac{du_e}{d\zeta} = \frac{C_f}{2} \tag{2.49}$$

$$\theta\frac{dH^*}{d\zeta} + (2H^{**} + H^*(1 - H))\frac{\theta}{u_e}\frac{du_e}{d\zeta} = 2C_D - H^*\frac{C_f}{2} \tag{2.50}$$

Drela (1989) included a third equation for a turbulent boundary layer, the lag equation for the maximum shear stress coefficient, $C_\tau$. As closure to the boundary layer equations, Drela (1989) includes the following boundary layer closure equations,

$$\begin{aligned} H^* &= H^*(H_k, M_e, Re_\theta) \\ H^{**} &= H^{**}(H_k, M_e) \\ C_f &= C_f(H_k, M_e, Re_\theta) \\ C_D &= C_D(H_k, M_e, Re_\theta) \end{aligned} \tag{2.51}$$

From the above equations $H^*$ and $H_k$, the kinetic shape parameter, is defined as,

$$H^* = \frac{\delta^*}{\theta} = \frac{\int_0^\infty \frac{u}{U}\left(1 - \left(\frac{u}{U}\right)^2\right) dy}{\int_0^\infty \frac{u}{U}\left(1 - \left(\frac{u}{U}\right)\right) dy} \tag{2.52}$$

and

$$H_k = \frac{H - 0.29M_e^2}{1 + 0.113M_e^2} \tag{2.53}$$

From Eqn. (2.53) it is important to note that for incompressible flows $M_e = 0$ this leads to $H_k = H$, as can be seen from the same equation.

#### Laminar boundary layer closure

XFOIL employs the Falken-Skan one-parameter profile family for laminar flow to derive (Drela, 1989).

$$H^* = \begin{cases} 1.515 + 0.076\frac{(4 - H_k)^2}{H_k}, & H_k < 4 \\ 1.515 + 0.4\frac{(H_k - 4)^2}{H_k}, & H_k > 4 \end{cases} \tag{2.54}$$

$$Re_\theta\frac{C_f}{2} = \begin{cases} -0.067 + 0.01977\frac{(7.4 - H_k)^2}{H_k - 1}, & H_k < 7.4 \\ -0.067 + 0.0022\left(1 - \frac{1.4}{H_k - 6}\right)^2, & H_k > 7.4 \end{cases} \tag{2.55}$$

$$Re_\theta\frac{2C_D}{H^*} = \begin{cases} 0.207 + 0.00205(4 - H_k)^{5.5}, & H_k < 4 \\ 0.207 - 0.003\frac{(H_k - 4)^2}{(1 + 0.02(H_k - 4)^2)}, & H_k > 4 \end{cases} \tag{2.56}$$

According to Drela (1989), the density thickness shape parameter $H^{**}$, has a fairly small effect at transonic flows. Thus the equation is given as,

$$H^{**} = \left( \frac{0.064}{H_k - 0.8} + 0.251 \right) M_e^2 \tag{2.57}$$

Interactive boundary layer techniques are presented with some difficulties which arise in the laminar boundary closures referred to as the "strong interaction problem". According to Smith et al. (2011), these interactions exist in the trailing edge and separation where neither the viscous nor the inviscid flow is dominant locally and is referred to as the "Goldstein singularity". Within these regions, numerical interaction between the viscous and inviscid flow fails (Katz and Plotkin, 2001). The laminar boundary layer closure equations reach a singularity at the point where the value of $H_k$ reaches its minimum value of 4, the previously mentioned Goldstein singularity (Smith et al., 2011). XFOIL circumvents this problem by solving the boundary layer and the inviscid flow simultaneously with a Full-Newton method.

### Turbulent boundary layer closure

Drela (1989) derived the turbulent closure relations from the skin friction and velocity profile of Swafford (1983). By doing so, he obtained the following closure equations,

$$H_k = \begin{cases} 1.505 + \frac{4}{Re_\theta} + \left( 0.165 - \frac{1.6}{Re^{\frac{1}{2}}} \right) \frac{(H_0 - H_k)^{1.6}}{H_k}, & H_k < H_0 \\ 1.505 + \frac{4}{Re_\theta} + (H_K - H_0)^2 \left[ \frac{0.004}{H_k} + \frac{0.007 \log Re_\theta}{\left( H_k - H_0 + \frac{4}{\log Re_\theta} \right)^2} \right], & H_k > H_0 \end{cases} \tag{2.58}$$

where the values of $H_0$ are given as follows,

$$H_0 = \begin{cases} 4, & Re_\theta < 400 \\ 3 + \frac{400}{Re_\theta}, & Re_\theta > 400 \end{cases} \tag{2.59}$$

The dissipation coefficient and equivalent normalised wall slip velocity are determined with Eqn. (2.60) and Eqn. (2.61), as described below,

$$C_D = \frac{C_f}{2} U_s + C_\tau (1 - U_s) \tag{2.60}$$

$$U_s = \frac{H^*}{2} \left( 1 - \frac{4}{3} \frac{H_k - 1}{H} \right) \tag{2.61}$$

Where $C_f$ is determined by the local boundary layer parameters. The turbulent boundary layer is defined as,

$$\delta = \theta \left( 3.15 + \frac{1.72}{H_k - 1} \right) + \delta^* \tag{2.62}$$

The empirical $G - \beta$ locus is used in the formulation and is defined as,

$$G = A \sqrt{1 + B\beta} \tag{2.63}$$

with $A = 6.7$ and $B = 0.75$ in the case of XFOIL, this is also one of the differences between XFOIL and RFOIL. The wake of an airfoil under XFOIL flow analysis, is defined as only one viscous layer, which means that only one $\theta$ and one $\delta^*$ are present at each node point on the wake contour. The wake momentum and wake displacement thickness is described as $\theta_{wake} = \theta_{upper} + \theta_{lower}$ and $\delta^*_{wake} = \delta^*_{upper} + \delta^*_{lower} + h_{TE}$, with $h_{TE}$ known as the trailing edge height. With this a value for $C_\tau$ can now be determined,

$$C_{\tau wake} = \frac{C_{\tau upper}\theta_{upper} + C_{\tau lower}\theta_{lower}}{\theta_{upper} + \theta_{lower}} \tag{2.64}$$

### 2.4.3. XFOIL transition prediction

In the laminar region Drela (1989), replaced the shear stress lag equation with the equation that governs the growth of the amplitude, $\hat{n}$ (also referred to as the $N_{crit}$ value) of the most-amplified Tollmien-Schlichting wave. In his article on the XFOIL mathematical model, Drela (1989) stated that a separation bubble is characterised by steep gradients in the edge velocity and the momentum thickness at the position of reattachment. This results in a jumping of these values, $\Delta u_e$ and $\theta$ in the small extent of the reattachment region. This phenomenon is illustrated in Fig. 2.8.

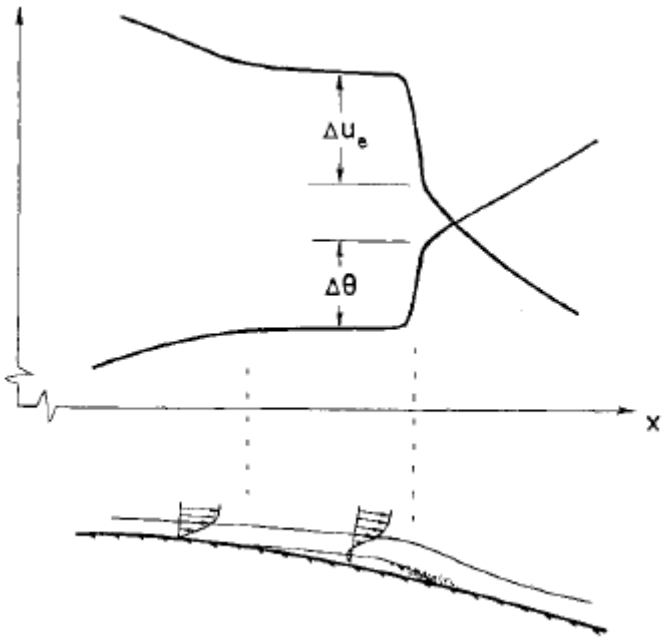


**Figure 2.8.** Jumps of boundary layer properties at reattachment (Drela, 1989)

According to Drela (1989), Eqn. (2.65) is used to relate the jumps over a small extent of the reattachment region and is derived by integrating the integral momentum equation over a small streamwise distance and disregarding the skin friction.

$$\frac{\Delta\theta}{\theta} = -(2 + H - M_e^2)\frac{\Delta u_e}{u_e} \tag{2.65}$$

From Eqn. (2.65) one can note that as $H$ rapidly increases down stream, the momentum thickness will jump inside the laminar boundary layer. This jump will also lead to an increase in drag, thus the importance of finding the correct location of transition.

This method of transition prediction employs a spatial-amplification theory, based on the Orr-Sommerfled equations (Drela, 1989). As previously stated, this method makes the assumption that transition occurs at a point where the the Tollmien-Schlichting waves are at their most unstable state. This amplification factor is related to the boundary layer properties. The spatial amplification rates of the Orr-Sommerfled equation have been solved for a wide range of shape parameters and unstable flow, resulting in unstable frequencies. These integrated amplification rates are approximated by a straight line, which can be seen in Fig. 2.9,

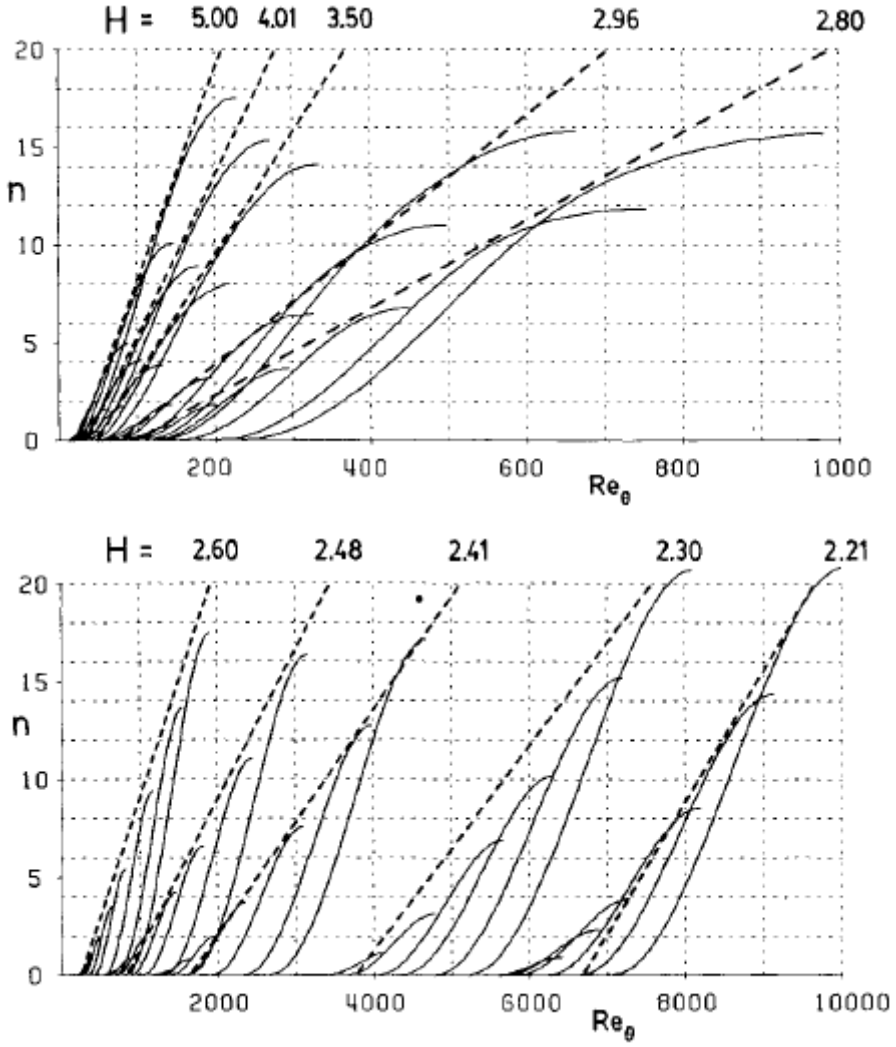


**Figure 2.9.** Envelope approximation

Bongers (2006) did extensive research on the transition model of XFOIL and implemented an improved method of predicting the transition point, whereas Drela (1989) only included an envelope version of the critical amplification ratio. In his study on this subject he presented the so called "Drela" method, in the XFOIL coding, as,

$$\frac{\partial N}{\partial \zeta} = \frac{AF \cdot DADR}{\theta} \cdot RFAC \tag{2.66}$$

where $AF$, $DADR$, and $RFAC$ are calculated as shown,

$$AF = -0.05 + 2.7\frac{1}{H+k-1} - 5.5\left(\frac{1}{H+k-1}\right)^2 + 3\left(\frac{1}{H+k-1}\right)^3 \tag{2.67}$$

$$DADR = 0.028(H_k - 1) - 0.0345e^{-(3.87\frac{H_k}{H_k-2}-2.52)^2} \tag{2.68}$$

$$RFAC = \begin{cases} 0, & RNORM < 0 \\ 3 \cdot RNORM^2 - 2 \cdot RNORM^3, & 0 \leq RNORM \leq 1 \\ 1, & RNORM \geq 1 \end{cases} \tag{2.69}$$

$$RNORM = \frac{^{10}\log Re_\theta - (^{10}\log Re_{\theta_{crit}}) - 0.08}{2 \cdot 0.08} \tag{2.70}$$

$$^{10}\log Re_{\theta_{crit}} = 2.492\left(\frac{1}{H_k-1}\right)^{0.43} + 0.7\left(\tanh\left(14\left(\frac{1}{H_k-1}\right) - 9.24\right) + 1\right) \tag{2.71}$$

These equations outline the relation between $^{10}\log Re_\theta$ and $H$ to the so called "Drela" method of transition prediction.

### 2.4.4. Viscous-inviscid coupling

Drela (1989), simply related the airfoil surface velocity, $u_e$ to the vorticity, on the top of the airfoil, to $\gamma$ and the bottom of the airfoil to $-\gamma$. He also derived a stream-function of the wake and related it to the vorticity on the airfoil and source on the airfoil. He thus obtained the following equations. For the vorticity distribution over the airfoil he declared,

$$u_{ei} = \pm\gamma_i \qquad 1 \leq i \leq N \tag{2.72}$$

$$u_{ei} = \bigtriangledown\Psi \cdot \hat{n} \tag{2.73}$$

$$= u_\infty \hat{n_y} - v_\infty \hat{n_x} + \Sigma_{j=1}^{N} c_{ij}^{\gamma}\gamma_i + \Sigma_{j=1}^{N+N_w-1} c_{ij}^{\sigma}\sigma_j \qquad N+1 \leq i \leq N+N_w \tag{2.74}$$

As previously mentioned, the interaction of the viscous layer on the potential flow is modelled by the wall transpiration condition if the local source strength sigma is equal to the local gradient of the mass deficit $m = U_e\delta^*$. By combining eqns. 2.72, 2.73 and 2.74 with the local source strength, $\sigma_i = \frac{dm}{d\epsilon} = \frac{M(i+1)-M(i)}{S(i+1)-S(i)}$, a generalised equation for the potential flow solution over the airfoil and wake is obtained (Drela, 1989). The influence of the viscous layer on the potential flow solution around the airfoil is modelled for the mass deficit on the airfoil and wake, with,

$$u_{ei} = u_{inv} + \Sigma_{j=1}^{N+N_w-1} d_{ij}m_j \qquad 1 \leq i \leq N+N_w \tag{2.75}$$

Where $d_{ij}$ embodies the effect of the local $m_j$ near the trailing edge on the global $u_{ei}$ (Drela, 1989). The Goldstein singularity poses a challenge when coupling the viscous flow with the inviscid flow solution. To remedy this singularity problem, Drela (1989), applied the two-integral method, which has proven to be an accurate method (Smith et al., 2011).

### 2.4.5. Karman-Tsien compressibility correction

To allow for the analysis of transonic flow, Drela incorporated a comperssibility flow correction derived by Karman-Tsien. This allows for the approximation of compressible flow parameters from incompressible flow parameters, $q_{inc}$, $C_{Pinc}$ by,

$$C_P = \frac{C_{Pinc}}{\beta + \frac{\lambda(1-\beta)C_{Pinc}}{2}} \qquad q = \frac{q_{inc}(1-\lambda)}{1-\lambda(\frac{q}{q_\infty})^2_{inc}} \tag{2.76}$$

with $\beta = \sqrt{1-M_\infty^2}$ and $\lambda = \frac{M_\infty^2}{(1+\beta)^2}$

### 2.4.6. The Newton solution procedure

The Newton solution plays a important part in the simultaneous solution to the inviscid equations together with the boundary layer formulations, and allows these equations to converge to the final viscous answer. Drela (1989) derived a simple Newton method and wrote the nonlinear equations, that needs to be solved, as,

$$\mathbf{F}(\mathbf{Q}) = 0 \tag{2.77}$$

where $\mathbf{F}$ is the vector of equations and $\mathbf{Q}$ is the vector of variables. At some iteration level $p$, this Newton solution can be written as,

$$\mathbf{F}^p + \left[\frac{\partial \mathbf{F}}{\partial \mathbf{Q}}\right]^p \delta\mathbf{Q}^p = 0 \tag{2.78}$$

$$\mathbf{Q}^{p+1} = \mathbf{Q}^p + \delta\mathbf{Q}^p \tag{2.79}$$

This linearised Newton system, in Eqn. (2.78), is a very large and spare tri-diagonal coefficient matrix, since the grids in this scheme are regular. The unknown vector, $\delta\mathbf{Q}$, is grouped into subvectors, containing the iterates of $\delta\theta$, $\delta m_j$ and within the laminar boundary layer, $\delta N_{crit}$. This Newton system is solved iteratively by a Gaussian elimination method. The Newton system is defined as the following form,

$$\left[J_{ij}\right] \begin{bmatrix} \delta\theta_j \\ \delta m_j \\ \delta Ncrit_j \ \ or \ \ \delta C_{\tau j} \end{bmatrix} = \left[-R_i\right] \qquad 1 \le i \le N + N_w \tag{2.80}$$

Drela (1989) made the choice of using $\delta m$ as one of the Newton variables, due to its being less complex to solve and able to allow for accurate predictions, since only in the case of $\delta m_j$, are the columns in $J_{ij}$ full. The columns of $\delta\theta$, $\delta C_\tau$ and $\delta N_{crit}$ are near the diagonal. A custom solver is then used to solve this system for one iteration of the global Newton solution.

## 2.5. The Squire-Young drag calculation model

The mathematical model utilised for predicting drag is known as the Squire-Young drag prediction model. This model is used to calculate drag at a reference point in the downstream of the wake, usually taken as one chord length downstream of the airfoil trailing edge. Coder

and Maughmer (2013) explained that through integration of an integral kinetic-energy equation (with the use of specific families of laminar and turbulent profiles, like the Falkner-Skan profile for the laminar regime) one can determine the value of the boundary layer shape factor, $H$, and the momentum thickness, $\theta$, at all streamwise locations in the boundary layer. The authors also stated that momentum thickness at the trailing edge is reflective of the momentum losses in the boundary layer; this condition at the trailing edge does not reflect a proper control-volume momentum balance. Rather, one usually applies the Squire-Young formula to the trailing edge condition on the upper and lower surfaces of the airfoil trailing edge to evaluate their contributions to the drag coefficient. This model for drag calculation can be written as,

$$C_d = 2\left(\frac{\theta_{TE}}{c}\right)\left(\frac{U_{TE}}{U_\infty}\right)^{\frac{5+H_{TE}}{2}} \tag{2.81}$$

for incompressible flow. Eqn. (2.81) is an extrapolation of the momentum deficit at the trailing edge to the deficit that would exist in a wake far downstream (Coder and Maughmer, 2013). It is further explained that the extrapolated quantities of Eqn. (2.81) are intended to represent the drag that would be calculated with a true control-volume momentum balance such that the calculated drag includes the skin friction drag and any total-pressure losses in the boundary layer. From this study the authors were able to confirm that this drag prediction model is also less sensitive to spurious drag that arise in the far downstream boundary layer.

## 2.6. Previous work done on linear vortex panel methods

Studies that have been previously done to improve upon lift and drag predictions of vortex panel methods such as XFOIL, are discussed. These proposed improvements were implemented into XFOIL, as will become clear in future sections and more detail including the proposed methods will be discussed. These improvements were developed for another vortex panel method, RFOIL, that was derived from XFOIL. RFOIL differs from XFOIL with some changes to the $G-\beta$ locus coefficients, including different profile families incorporated into RFOIL to allow for better wind turbine airfoil performance analysis. Not much about the RFOIL program can be found, as it is not an open source program, although some studies have mentioned improved velocity profile families (Bongers, 2006). Nevertheless, both XFOIL and RFOIL utilise a vortex panel method and thus the assumptions apply to both programs. It was concluded that the improvements to RFOIL lead to improved drag and lift predictions. Thus, the purpose of the study is to see if the improvements will improve upon XFOIL's lift and drag predictions when implementing these changes to XFOIL.

### 2.6.1. Improvements to drag predictions

The fundamental problem with drag calculations using interactive boundary layer methods is that there is an inherent underprediction of boundary layer quantities which causes inaccurate drag predictions. The edge velocities are overpredicted, which causes underprediction of the momentum and displacement thicknesses (Ramanujam, Ozdemir, and Hoeijmakers, 2016). In XFOIL, the standard method for the calculation of the drag coefficient is given in Eqn. (2.82),

$$c_d = \frac{2[\theta_\infty]_{x=\infty}}{L} \tag{2.82}$$

with $L$ being the chord length of an airfoil, but the formulation of the momentum thickness in XFOIL is taken with reference to the edge velocity, instead of the free stream velocity. Furthermore, the momentum thickness is in term of the streamwise coordinates $\zeta$ and $\eta$, instead of Cartesian coordinates (Ramanujam, Ozdemir, and Hoeijmakers, 2016). These two definitions of momentum thickness are not the same and may not be necessarily equal to the actual drag on the airfoil. This assumption is reasonable in the far downstream location where $\zeta \sim x$ and $\eta \sim y$ coincide. Consider Fig. 2.10.

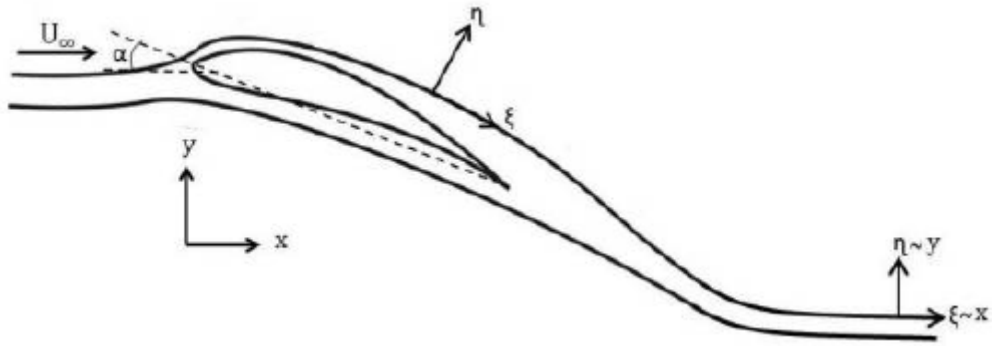


**Figure 2.10.** Streamwise and Cartensian directions (Ramanujam, Ozdemir, and Hoeijmakers, 2016)

The relation for drag follows from the momentum conservation along the incident flow direction, the x- direction (Ramanujam, Ozdemir, and Hoeijmakers, 2016). This argument is explained by the fact that there is a significant difference between a flat plate and an airfoil in terms of the pressure distribution around the airfoil. This pressure gradient parallel and normal to the airfoil surface, is caused by an airfoil being of finite thickness and the flat plate is considered to have a thickness of zero. In addition, an important effect of angle of attack is that there is an inflow on the airfoil, which is zero for the flat plate theory. As a consequence, according to Ramanujam, Ozdemir, and Hoeijmakers (2016), the region outside the boundary layer has a significant pressure gradient in the normal to streamline direction. Due to the presence of this pressure gradient, the velocity outside the boundary layer, varies in the normal direction. For the flat plate case, the edge velocity is equal to the free stream at every point outside the boundary layer, this allows for neglecting the viscous effects in that region. This assumption results in an overprediction of the edge velocity that leads to an underprediction of the integral quantities' displacement and momentum thickness (Ramanujam, Ozdemir, and Hoeijmakers, 2016), refer to Fig. 2.5.

In order to calculate the error in drag $\Delta\theta$, the error in momentum thickness must be calculated at the end of the wake Ramanujam, Ozdemir, and Hoeijmakers, 2016 The error is defined as the difference between the actual momentum loss thickness, $\theta_\infty$, based on the free stream velocity, and the predicted momentum loss thickness, $\theta_e$, which is based on the velocity at the edge of the boundary layer, $U_e$.

### Results from drag improvement

Ramanujam, Ozdemir, and Hoeijmakers (2016), investigated these improvements against experimental data of various airfoils, including thicker airfoils for wind turbine applications. The purpose of the current study is to reflect on thin airfoils, as XFOIL's accuracy deteriorates with an increase in the airfoil thickness. The flow analysis was performed at incompressible flow conditions, thus $M_\infty = 0$, and natural transition with a free stream turbulence intensity of 0.07% ($N_{crit} = 9$). A noticeable improvement in drag predictions for the NACA 0012 (Fig. 2.11

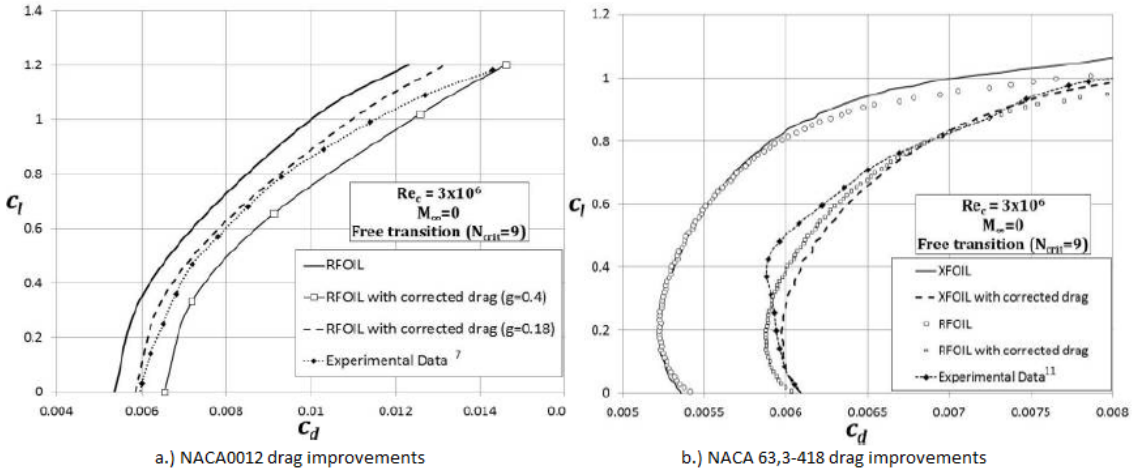


a.) NACA0012 drag improvements

b.) NACA 63,3-418 drag improvements

**Figure 2.11.** Comparison of Lift-Drag polars for thin airfoils (Ramanujam, Ozdemir, and Hoeijmakers, 2016)

a.) and NACA $63_3$-418 (Fig. 2.11 b.) airfoils was documented.

### 2.6.2. Improvements to lift predictions

Ramanujam and Ozdemir (2017) proposed a way to improve the lift predictions of an XFOIL-based software. A new approach to improving lift predictions was discussed, with no detail on how this was accomplished. The reason why vortex panel methods are less accurate at predicting the correct maximum lift value was the main focus. A new approach to the problem was discussed and leaves the reader to make the changes without much detail given. Nevertheless, it is possible to edit the source code to calculate these improved lift predictions. First, it is important to understand how XFOIL executes a simulation to better understand how this improvement can give more accurate answers, Fig. 2.12 shows this process in a flowchart format.

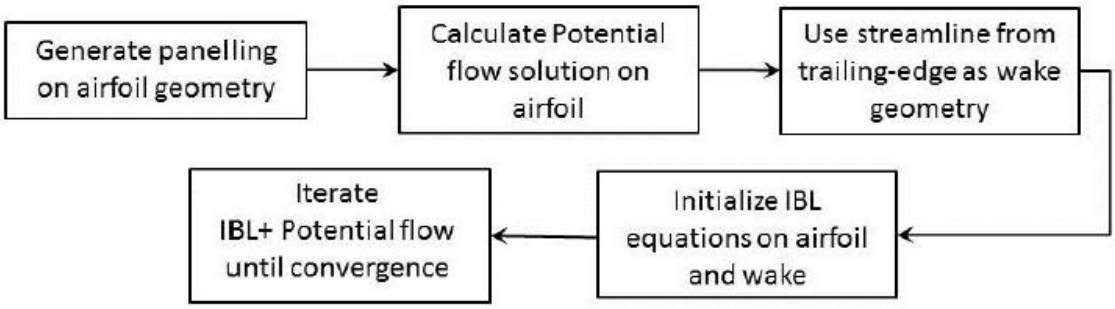


**Figure 2.12.** XFOIL flowchart (Ramanujam and Ozdemir, 2017)

An XFOIL flow analysis requires an airfoil geometric input, in the form of x and y coordinates. The airfoil contours are then broken up into a finite number of panels and node points. The user can prompt an inviscid or viscous analysis. Note that for a viscous analysis the inviscid flow will also be calculated and converged with the viscous calculations to attain 'viscous' results (Ramanujam and Ozdemir, 2017). After panel generation has been finalised, the inviscid case is obtained by solving the potential flow equations to obtain the vorticity strengths at each panel node on the airfoil. With the vorticity strength now known, the dividing streamline is calculated and is used as the building block of the wake trajectory. Note, that this wake is

based on the inviscid solution to the flow. The Integral Boundary Layer (IBL) equations are initialised on the airfoil and wake with a source distribution superimposed on the airfoil contour that represents the viscous layers and displacement effects of the boundary layer. The potential flow equations and IBL are then allowed to converge through a full Newton method to acquire the final solution (Ramanujam and Ozdemir, 2017).

According to Drela (1989) if an angle of attack, $\alpha$, is specified, the wake trajectory for the viscous solution is taken from the inviscid solution. This means that a viscous solution is calculated form an inviscid wake. This statement is not correct, as viscous effects will influence the vorticity distributions and change the wake trajectory and finally decrease the lift prediction (Drela, 1989).

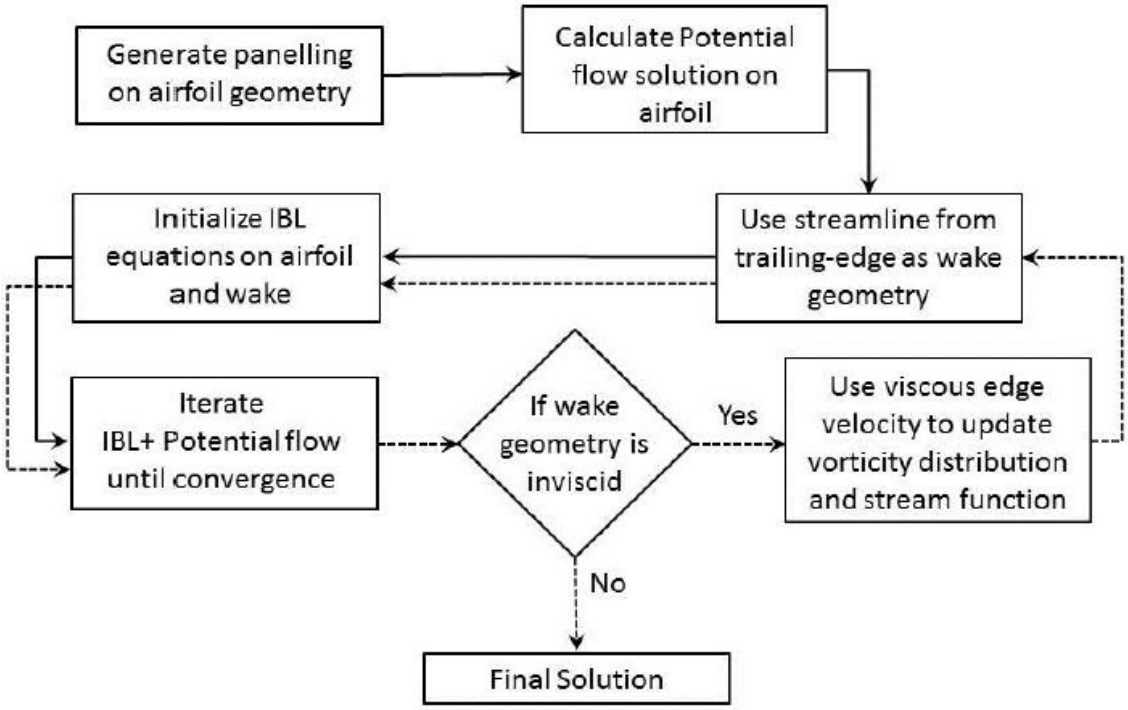


**Figure 2.13.** Proposed improvement flowchart (Ramanujam and Ozdemir, 2017)

Ramanujam and Ozdemir, 2017 then proposed a new approach to include the viscous effects and these included a viscous wake. The new approach was to initially calculate the boundary layer solution with the inviscid wake geometry and use the resulting edge velocity to update the vorticity distribution. This then updated the wake trajectory to include the viscous effects. This change in the wake trajectory is an indication of the change in the flow field as the wake trajectory is a function of the flow field at the trailing edge of the airfoil. With the new wake trajectory, the solution can then be repeated to obtain the full viscous solution. Fig. 2.13 illustrates the proposed improved approach to obtain results that are in better agreement with experimental data.

Not much detail is presented on how this was achieved; the authors merely proposed a new approach. With methodical inspection of the source codes, the way to achieve this is revealed. Eqn. (2.47) is important as it is the system of equations that calculates the vorticity strength distribution over the airfoil panels. This is the key point where the viscous edge velocity can be used to update the vorticity strength distributions.

### Results from lift improvement

Ramanujam and Ozdemir (2017), completed the analysis and validation of this improved method under incompressible flow conditions ($M_\infty = 0$) with a natural transition condition and a free stream turbulence intensity of 0.07%, setting $N_{crit} = 9$. The study showed that even for thin airfoils like the NACA $63_3 - 418$, there is a noticeable improvement in the lift predictions. The effect of increasing the airfoil thickness led to severe overprediction of the lift coefficient. These proposed changes significantly improved the lift predictions within the linear lift region and are in better agreement with experimental data.

The NACA $63_3 - 418$ case study (Fig. 2.14) showed that with the new improved method of lift prediction, the maximum lift is underpredicted and the airfoil stalls earlier when compared to experimental data. Ramanujam and Ozdemir (2017) noted that this observation is not completely true, because the original RFOIL method drag prediction is almost identical to the improved method. This indicates that the airfoil stalls at the same angle of attack in both methods, contradicting the experimental data. This discrepancy in predicting the onset of stall, that were present in all their study cases, is described as a problem with the closure relations for turbulent flow, which regulate the onset of flow separation (Ramanujam and Ozdemir, 2017).

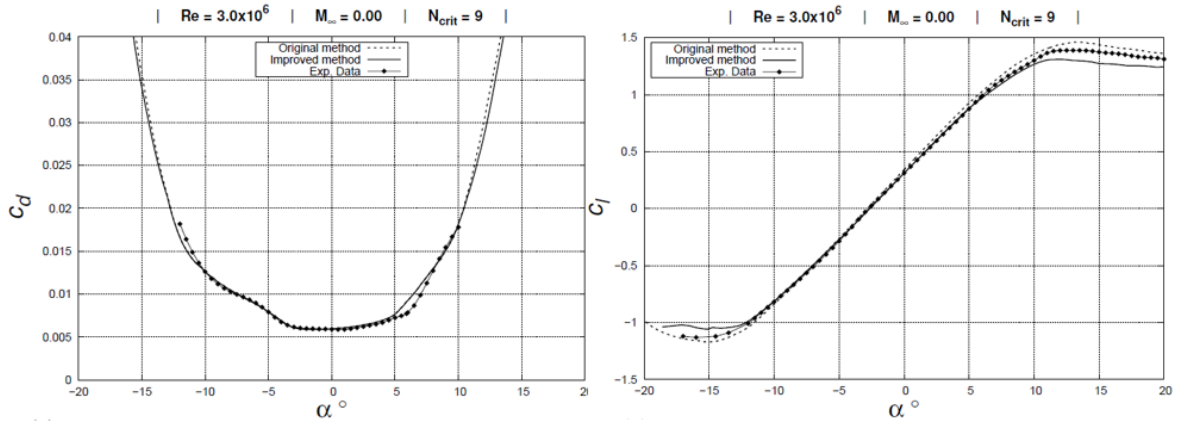


a.) Corrected drag prediction with wake update

b.) Improved lift prediction with wake update method

**Figure 2.14.** NACA $63_3$-418 improved polar predictions (Ramanujam and Ozdemir, 2017)

This discrepancy is an existing shortcoming of the existing vortex panel methods that has been masked by the lift overprediction problem (Ramanujam and Ozdemir, 2017). This problem was noticed in the analysis of thicker airfoils (Fig. 2.15) as well, where the lift prediction has not been completely resolved. For these airfoils the maximum lift is not being underpredicted as seen in the other cases. The discrepancy seemed to relate to the trailing edge height, $h_{TE}$.

Ramanujam and Ozdemir (2017) gave insight into the overprediction of lift problem, stating that there are two aspects to this problem. First, this is due to the inviscid solution which has been improved upon and secondly, due to the trailing edge panel method formulation, where a source strength is associated with the trailing edge panel. The latter leads to a behaviour where mass is ejected from the trailing edge, resulting in a reduction in base pressure, affecting the pressure distribution on the airfoil surface as well as in the wake.

It was shown that the wake update approach made noticeable improvements, as was observed in the study cases on thin and thick airfoils. The post-stall lift and drag predictions are still not accurate with the improved method as this type of computational method for predicting flow becomes inaccurate as the boundary layer becomes too thick when separation sets in (Ramanujam and Ozdemir, 2017), leading to a general inaccuracy in the results near and post-stall.

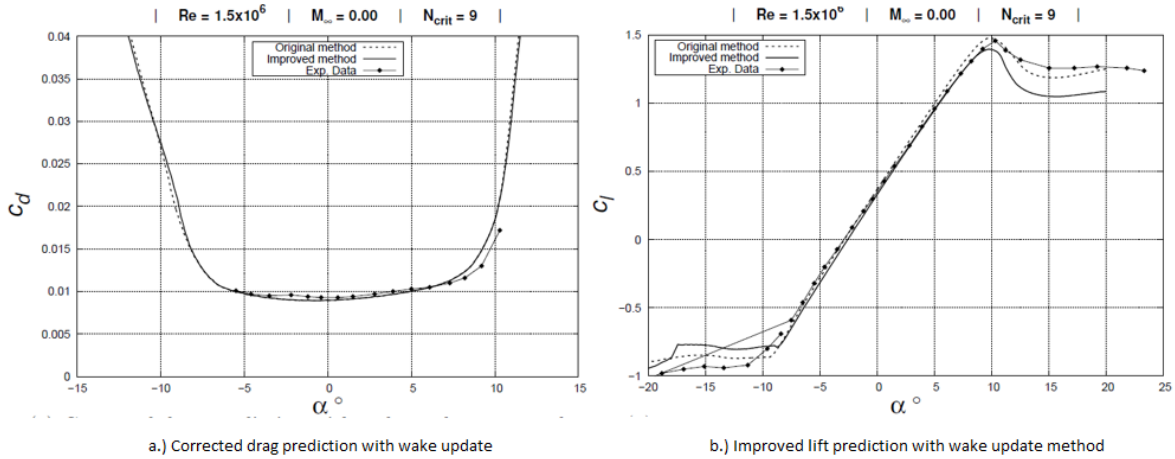


a.) Corrected drag prediction with wake update

b.) Improved lift prediction with wake update method

**Figure 2.15.** AH 93-W-300 improved polar predictions (Ramanujam and Ozdemir, 2017)

## 2.7. Conclusion

In the first section of the literature study, a background into potential flow theory was given which allowed for insight into basic flow calculations which lay the foundation of how these calculations are done in XFOIL. The algorithm of XFOIL is complex and with this knowledge a fundamental understanding of the program structure was obtained so that changes could be implemented.

Some changes which are suggested by literature involve substantial alterations to the structure and sequencing of the calculations. In future sections, this will be discussed in more detail. From the literature study it is clear that it is possible to improve upon the lift and drag predictions given by XFOIL (vortex panel methods). There were logical explanations for the original algorithm strategies which led to larger deviations from experimental data as shown by Ramanujam, Ozdemir, and Hoeijmakers (2016) and Ramanujam and Ozdemir (2017). These proposed improvements were implemented to the program RFOIL and validated against experimental data showing noticeable improvements. Drela (1989) supplied open source information on XFOIL that simplifies the process of implementing changes to the source code.

# 3. Chapter 3: Standard XFOIL validation

In this chapter, an investigation has been done to study the sensitivity of XFOIL results relating to the number of panels that are generated over the airfoil contour. XFOIL allows for the calibration of lift and drag predictions by taking the free stream turbulence intensity into account. This has been achieved by defining the turbulence intensity as a function of the amplification factor. The value of the amplification factor is not a number that can be arbitrarily selected, rather it should reflect on the wind tunnel's quality.

Panels are generated over the airfoil contour and the operator is able to edit the panel configuration by changing the total number of panels and panel density distributions. From the literature survey it is shown that the results of XFOIL are sensitive to the number of panels that have been specified. Therefore, an investigation is required to establish the number of panels needed to obtain accurate lift and drag predictions, to reflect on the accuracy of XFOIL lift and drag predictions as well as the number of panels related to the geometry of the airfoil. Thus, if a small number of panels is used, one can obtain inaccurate predictions. The reason for this is that the geometry of the airfoil is less captured from this small number of panels leading to sharp edges in the geometry. By increasing the number of panels more of the airfoil geometry is captured, thus increasing the reliability of the predictions.

This investigation includes a panel sensitivity study and a amplification factor study to calibrate the software to provide reliable solutions. The validation cases were performed at Reynolds numbers ranging from $1\times10^6$ to $3\times10^6$. The airfoils that were employed for the method validation is the NACA 0012, NACA $63_3$-418, FX61-163, FX66-S-196 and the E603 airfoils. The FX61-163, FX66-S-196 and E603 airfoils find their application in the sailplane industry and the NACA $63_3$-418 airfoil, in the wind turbine industry. These airfoils are thin, with low thickness to chord ratios, and will be validated against their respective experimental data obtained from various sources. These sources include wind tunnel data obtained from the university of Stuttgart, NACA LTT facility and data obtained from TU Delft experiments.

It has been mentioned previously, that wind tunnel measurements do not represent the ultimate truth of flight characteristics of an airfoil, but they are flawed, as uncertainties arise in wind tunnel experiments. Both the numerical and experimental data are used together to better understand actual flight performance. Numerical methods have flaws, such as the Goldstein singularity that arises near, at and after flow separation, which makes the prediction of the onset of flow separation difficult.

Unfortunately, the uncertainties in wind tunnel testing are very difficult to access. The reason relates to measurement procedures, which typically differ between tunnels. In addition, traditional error analyses cannot be applied straightforwardly because some error sources cannot be quantified directly and even can strongly depend on the test object. For example: the spectral distribution of the turbulence intensity can be important for transition on an airfoil with a long laminar run, whereas a slightly different airfoil (or the same one at another angle of attack) may be more insensitive to the same free-stream disturbance.

At high angles of attack, experimental measurements are not as accurate compared to smaller angles due to the larger distance between the total pressure hole for flow measurements in the wake (Fuglsang, Antoniou, and Sørensen, 1998). Also, the theoretical airfoil may differ from

the testing airfoil, which in the case of the previous study has been manufactured to a tolerance of 1 mm. Corrections had to be made on the downwash and streamline curvature as they result in a change in the angle of attack due to the appearance of an induced velocity normal to the flow direction and the airfoil section (Fuglsang, Antoniou, and Sørensen, 1998). Fuglsang and Bove (2008) showed that minor imperfections of the bushings with taps in the walls caused a small scattering of the results, which had to be corrected mathematically to calculate lift. Both the numerical methods and experimental measurements have flaws in their final measurement or predicted results. When both methods suggest similar tendencies, it might contribute to the understanding of actual flight performances.

## 3.1. NACA 0012 airfoil: Wind tunnel data vs XFOIL predictions

This is a thin, symmetrical airfoil, with a thickness of 12% relative to the chord length and which is used in wind turbine applications due to its good lift-to-drag ratio. The experimental data was obtained from experiments done by Miley (1982), who studied and documented airfoil experimental data. The author's work was published in Miley (1982) and it enabled engineers to use the data for two-dimensional validation purposes. This particular experimental analysis was completed at the University of Stuttgart at wind tunnel IAG #1. The experiment was performed at a Reynolds number of $3\times10^6$ with a turbulence level of 0.03%. This performance analysis was conducted at an angle of attack range from 0° up to 12°. Within this range this airfoil obtained a lift-to-drag ratio of 86.

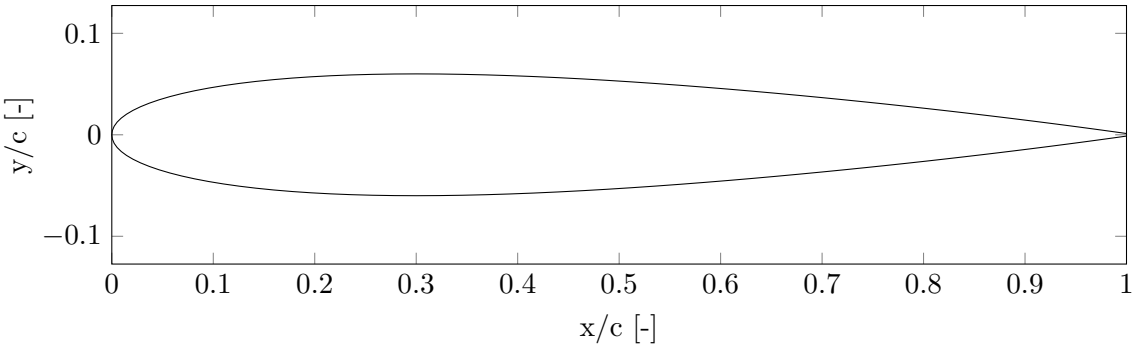


**Figure 3.1.** NACA 0012 airfoil

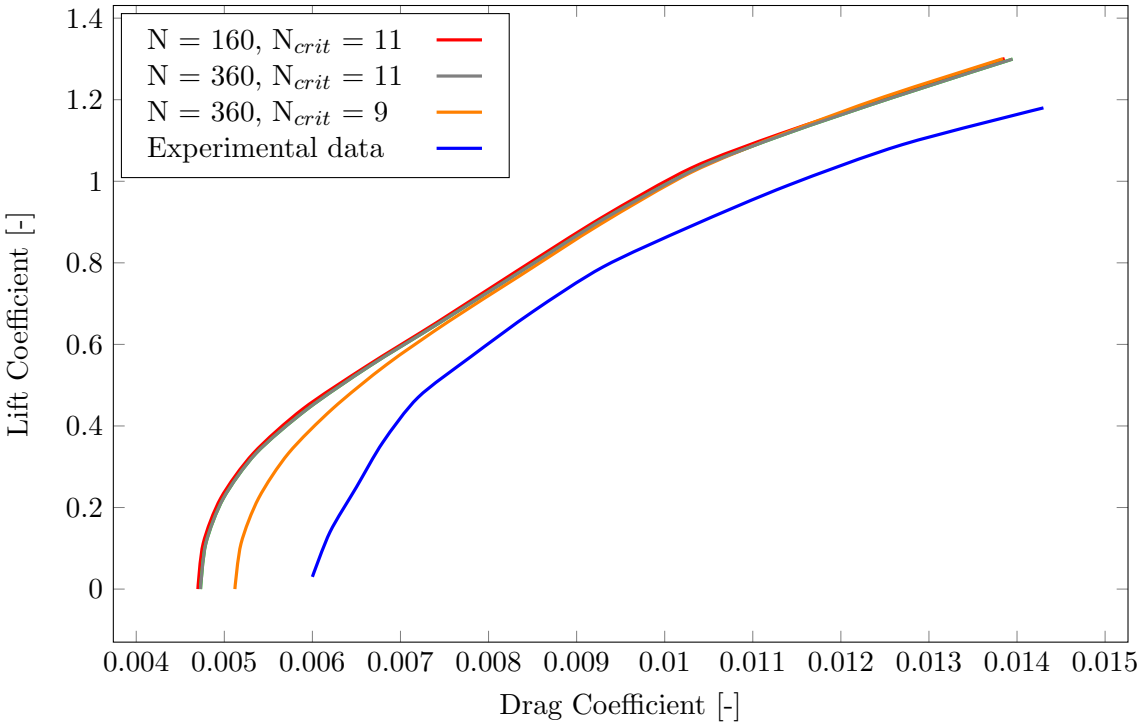


**Figure 3.2.** NACA 0012: Experimental data against the panel sensitivity analysis with $N_{crit} = 11$ and Re = $3^6$

Note in Fig. 3.2 that the values are close in range and do not have a significant change against the experimental data. Thus, this airfoil is not sensitive towards the number of panels, as the following airfoils will show.

### 3.1.1. NACA 0012: Discussion of validation results

From the investigation it is clear that XFOIL is more than capable of analysing thin airfoils, especially with a geometrically symmetrical shape. In Fig. 3.2 the convergence of the values with an increase in panel numbers is observed. This increase in accuracy is within 1%, concluding than this airfoil's performance in predicting polar predictions is insensitive to the change in panel numbers. It is generally known that increasing the number of panels will give higher accuracy, as more detail of the geometrical shape is captured.

A study on the sensitivity of XFOIL towards the amplification factor, $N_{crit}$, was completed and is shown in Fig. 3.2. The value of the amplification factor is, as mentioned earlier, a reflection of the wind tunnel quality. This means that a turbulence level of 0.03% is equal to a $N_{crit}$ value of 11. These values are then compared to the standard XFOIL amplification factor of 9. Fig. 3.2 clearly shows the difference in predictions with an amplification factor of 11. This results in an under prediction of lift and drag according to the experimental data.

XFOIL was able to accurately predict the shape of the lift vs drag predictions of the experimental data, but with a slight offset from the experimental data. This shows the need for improving XFOIL, to ensure values are in closer proximity to the experimental data. It is also important to note that the analysis of this airfoil was performed at 1° increments as no adverse changes were observed in the shape of the curve of XFOIL's predictions.

## 3.2. NACA $63_3$-418 airfoil: Wind tunnel data vs XFOIL predictions

This airfoil finds its application in the wind turbine industry. The current airfoil along with the previous one, is thin in reference to other wind turbine airfoils, which are up to 40% thicker. This particular airfoil has a thickness of 18% and a camber of 2%. The experimental data was obtained from experiments done by Abbott and A.H. (1959). Their work was included in their book which was first published in 1949 and republished in 1959. The experiments were performed at a Reynolds number of $3\times10^6$ and at an angle of attack range from -6° up to 11°. Within this range the authors obtained a maximum lift-to-drag ratio of 126, remarkably higher than the symmetrical airfoil.

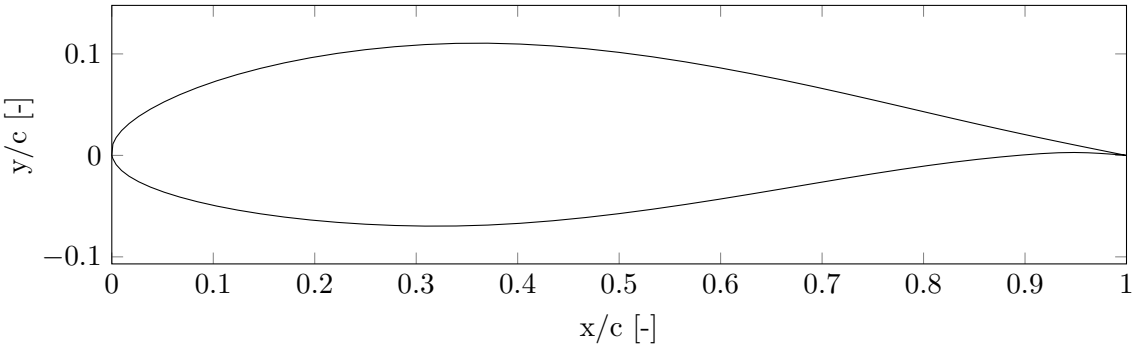


**Figure 3.3.** NACA $63_3$-418 airfoil

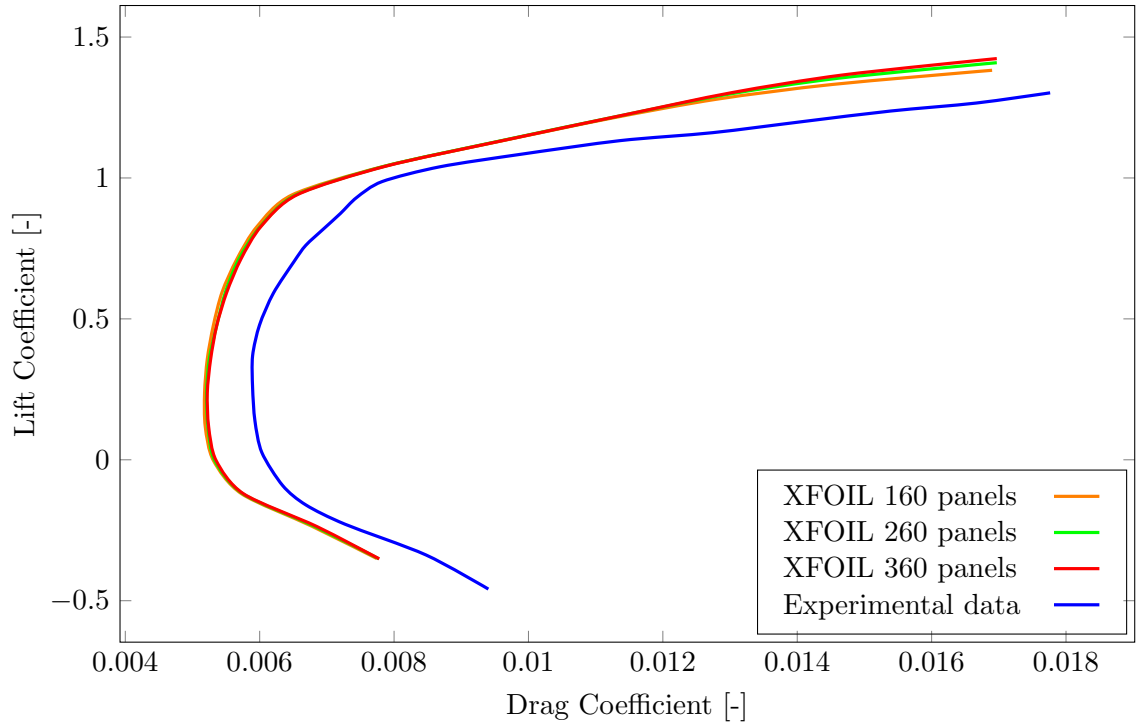


**Figure 3.4.** NACA 63,3-418: Experimental data and the panel sensitivity analysis with $N_{crit} = 9$ at Re = $3\times10^6$

Note that an increase in the number of panels does not have adverse effects on the prediction of lift and drag polars. At high angles of attack, significant changes can be observed, but this might be associated with the tendency of XFOIL's lift and drag predictions to decay at stall conditions.

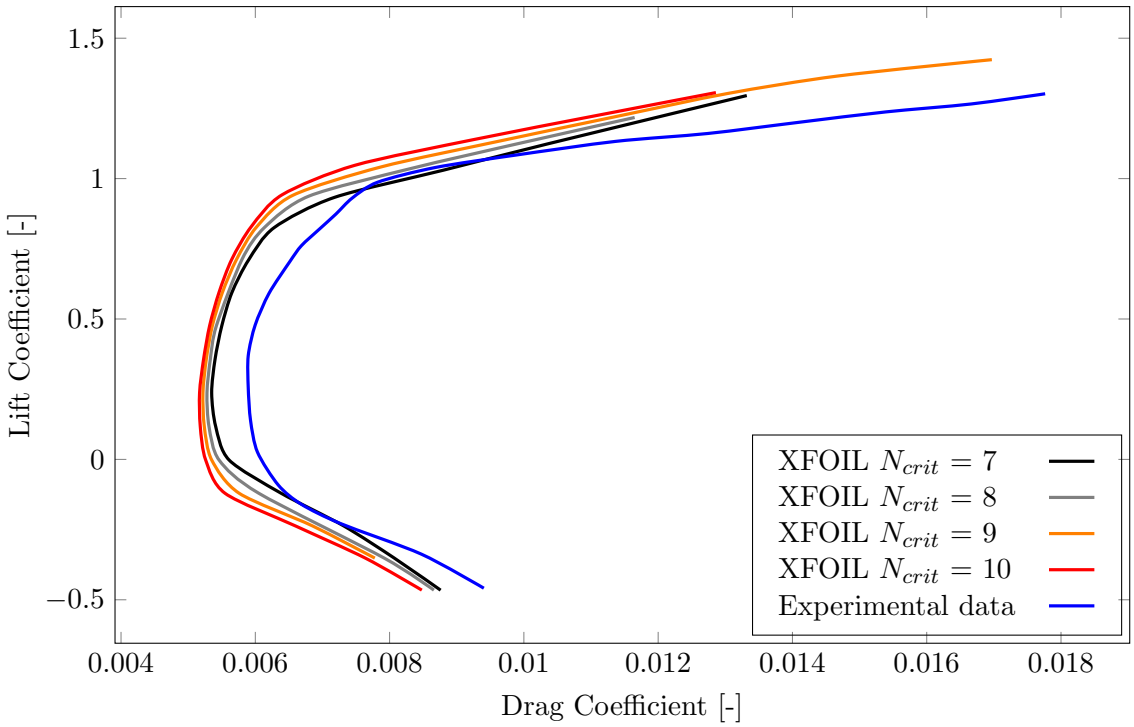


**Figure 3.5.** NACA 63,3-418: Experimental data with multiple $N_{crit}$ values at Re = $3{\times}10^6$

### 3.2.1. NACA 63,3-418: Discussion of validation results

Once again, the panel sensitivity investigation shows that the analysis of the airfoil performance and its results are insensitive to the number of panels over the airfoil contour. At high angles of attack there is a remarkable difference in lift and drag predictions and in such situations XFOIL is most inaccurate due to the collapse of the Kutta condition, superimposed on the trailing edge.

In Fig. 3.4 convergence is clear with an increase in panel numbers. Also recognisable is the offset of XFOIL predictions to the experimental data, in Fig. 3.4. This is rather similar to the offset observed in the NACA 0012 case. From the experimental data, recorded by Abbott and A.H. (1959), no turbulence level value was given to compare the standard XFOIL amplification factor to, thus the effect of increasing and decreasing the amplification factor was investigated. When increasing the $N_{crit}$ value to 10, a decrease in the accuracy of the predictions was noticed as drag became more underpredicted. The reason for this is that transition is predicted further downstream which leads to reduced drag at the specified angles of attack. When the $N_{crit}$ value was decreased to a value of 8, drag is less underpredicted, but a divergence in lift predictions from the experimental data is observed. Another observation made was that if the $N_{crit}$ value was decreased even further, the offset of the XFOIL predictions was still present.

One can observe that once again XFOIL was able to capture the lift vs drag curve shape, in reference to the experimental data. but it is at an offset of the experimental data. This suggests a fundamental problem with XFOIL predictions as outlined in **Chapter 2**. Also, the deviation at high angles of attack causes a divergence from the experimental data. This observation has already been explained.

## 3.3. FX61-163 airfoil: Wind tunnel data vs XFOIL predictions

The next airfoil under investigation, is a Wortmann airfoil. This airfoil is used as the root wing of the ASW-19 Standard Class sailplane, manufactured by Alexander Scheicher Segelflugzeugbau. The airfoil has a maximum thickness of 16.3% with a camber of 2.6%. The wind tunnel experiment was conducted at a Reynolds number of $1{,}5{\times}10^6$ at an angle of attack range from -5° up to 11°. The XFOIL analysis with smaller 0,5° increments obtained the same overall shape in comparison with the experimental data. This airfoil was examined with the standard XFOIL $N_{crit}$ value against the wind tunnel, corresponding to a turbulence level of 0.04% which gives a $N_{crit} = 10.32$.

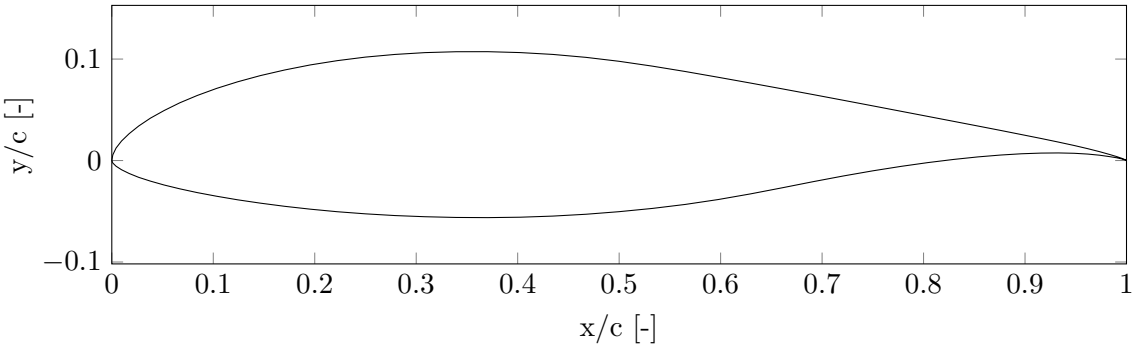


**Figure 3.6.** Wortman FX61-163 airfoil

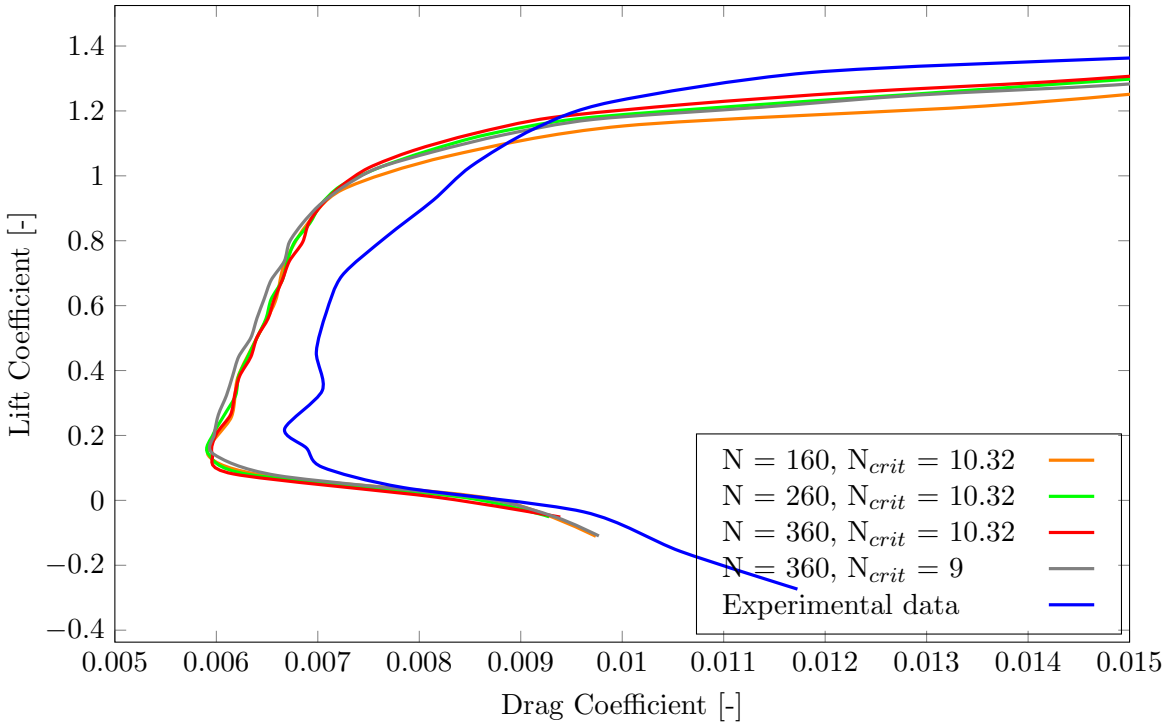


**Figure 3.7.** FX61-163: Experimental data against the panel sensitivity analysis with $N_{crit} = 10.32$ and $N_{crit} = 9$ at Re = $1{,}5{\times}10^6$

### 3.3.1. FX61-163: Discussion of validation results

With the analysis of this airfoil the dependence of the number of panels was especially noticed at stall conditions. A higher number of panels ensured a tendency toward the experimental data. However, no significant difference in lift vs drag predictions was observed at the linear lift region and at low angles of attack. This indicates that the airfoil is able to approximate the trailing edge better at the same angle of attack, with a higher number of panels.

It is clear from this study, including the previous cases, that XFOIL can accurately predict the over shape of the lift vs drag curve. This is once again evident from Fig. 3.7. Also, observable is the offset that arises which was also observed in the previous cases.

The effect of the change in the amplification factor was also studied compared to the standard XFOIL practice with the quality of the wind tunnel taken into account, as in Fig. 3.7. It seems as if the change in the value of the amplification factor does not have a major effect on the predictions. Nevertheless, This will be the standard practice throughout this report, to compare the standard XFOIL amplification value against the quality correlated value of the wind tunnel.

## 3.4. FX66-S-196 airfoil: Wind tunnel data vs XFOIL predictions

This airfoil is designed by Prof. F.X. Wortmann for the University of Stuttgart (Gooden, 1979) for the application in the sailplane industry. The experimental data was obtained from an experiment done at the University of Stuttgart wind tunnel, the data was published by Gooden (1979). This airfoil has a thickness of 19% and a camber of about 3%. The experiments were conducted at a Reynolds number of $2\times10^6$ and the data at a angle of attack ranging from -5° up to 8.5°. Within this range this airfoil reached a maximum lift-to-drag ratio of 125. According to Lasauskas and Naujokaitis (2009), the wind tunnel quality is high, resulting in a low turbulence level of up to 0.04%.

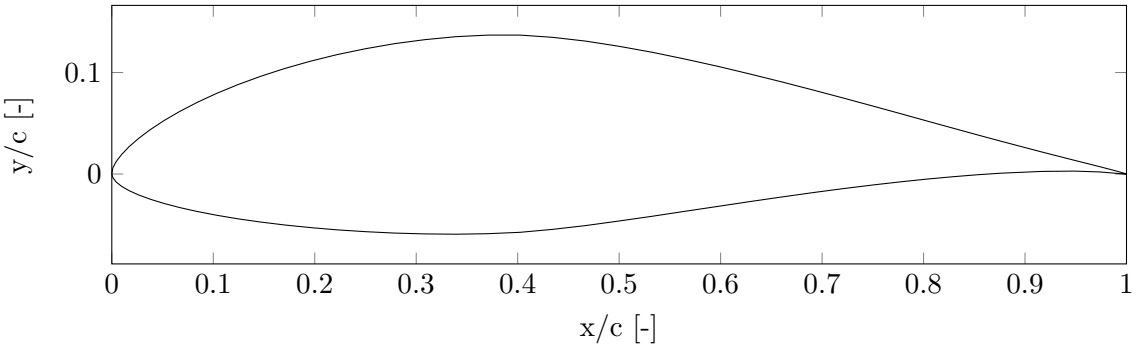


**Figure 3.8.** Wortmann FX66-S-196 airfoil

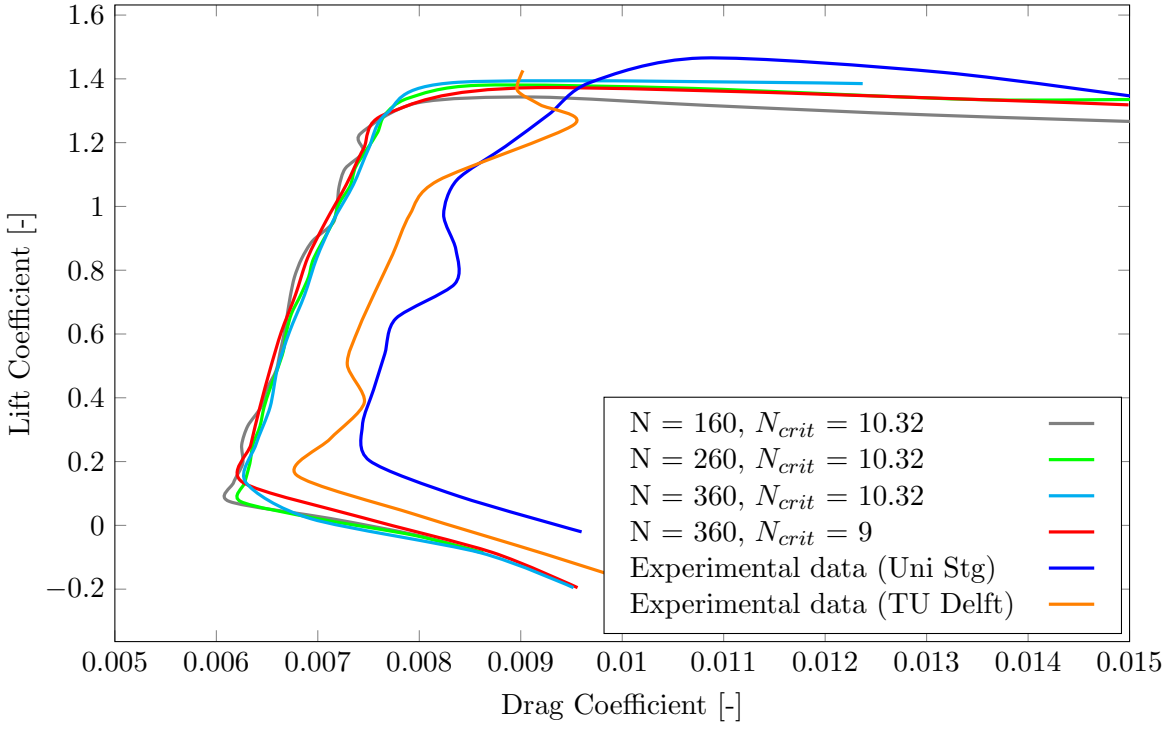


**Figure 3.9.** FX66-S-196: Experimental data with $N_{crit} = 9$ and $N_{crit} = 10.32$ at Re = $2\times10^6$

### 3.4.1. FX66-S-196: discussion of validation results

Convergence to a more accurate prediction of the polar plots is clear From Fig. 3.9. Increasing the number of panels, results in improved predictions of the lift and drag predictions at stall conditions. This becomes clear when considering Fig. 3.9. Another tendency of XFOIL is evident, which is yet again the presence of the offset of the predicted values to the experimental data. By increasing the number of panels one can observe that the increase in panels has little effect on the low angle of attack range or on the linear lift region, but at high angles of attack the predicted values tend towards the experimental data.

The wind tunnel turbulence level was measured as 0.04%, resulting in an amplification factor of 10.32. This value of $N_{crit}$ for the experimental condition was then compared to the standard XFOIL amplification value. The results can be seen in Fig. 3.9. From this graph it is evident that the increase in amplification value causes the XFOIL lift vs drag curve to tend towards the experimental data with a widening of the predicted value in the low and high angles of attack regions. No significant difference is observed within the linear lift region. It is noticeable that as the amplification factor is increased, the shape of the curve of the experimental data is similar to what is calculated by XFOIL, but with the offset of the XFOIL values to the experimental data.

## 3.5. E603 airfoil: Wind tunnel data vs XFOIL predictions

The airfoil E603 is designed by R. Eppler for the Astir sailplane (Lasauskas and Naujokaitis, 2009). This sailplane has a 15 m wing span with an aspect ratio of 18.2 m capable of carrying a payload of 195 kg. The airfoil is designed with a thickness of 19% and a camber of 3.6%. Wind tunnel experiments were conducted on this airfoil and were published in Althaus (1996). The wind tunnel experiments were conducted at a Reynolds number of $1\times10^6$ at the University of Stuttgart. In a study done by Lasauskas and Naujokaitis (2009), the wind tunnel turbulence level of 0.04% was recorded but this was not adjusted in their investigations. Lasauskas and Naujokaitis (2009) explained the reason for this was that the amplification factor has a different meaning in the PROFIL05 software developed by R. Eppler, compared with XFOIL's envelope transition prediction method. The effect of the change in the amplification factor value was studied in this report and is shown in Fig. 3.11.

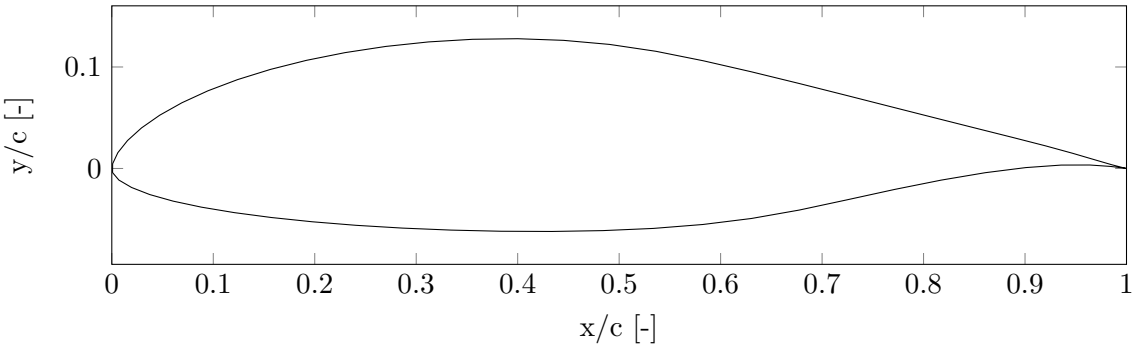


**Figure 3.10.** Eppler-603 airfoil

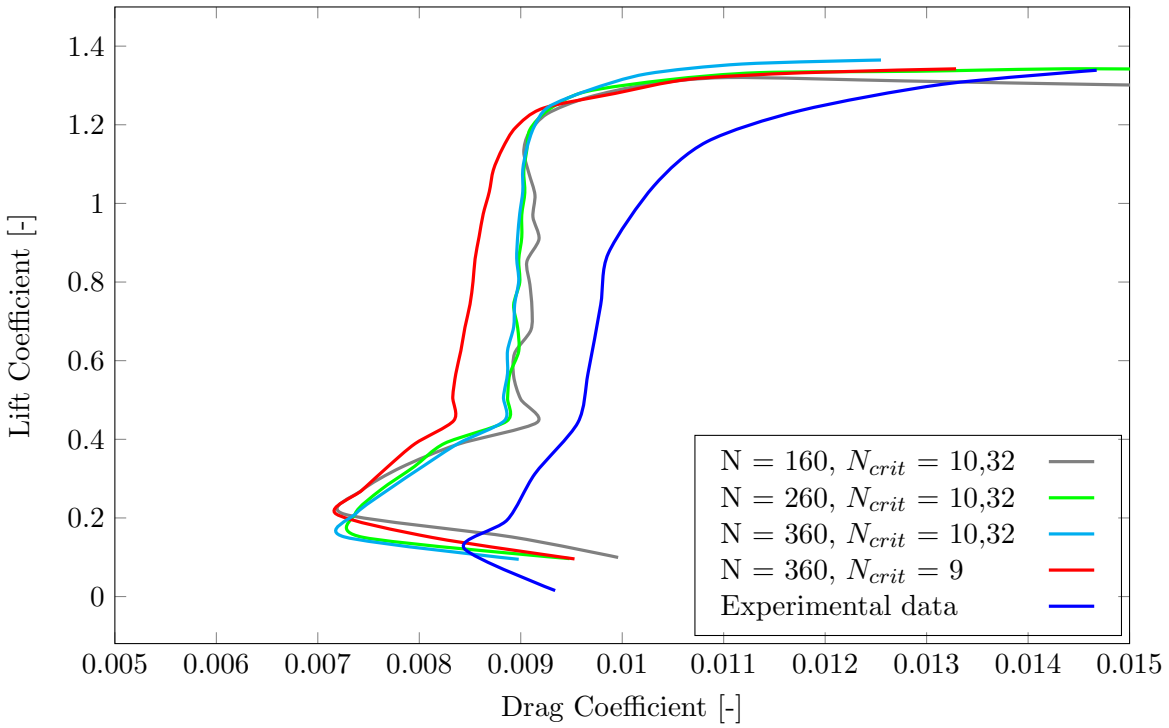


**Figure 3.11.** E603: Experimental data against $N_{crit} = 9$ and $N_{crit} = 10.32$ at Re = $1\times10^6$

### 3.5.1. E603: discussion of validation results

From Fig. 3.11 the effect of increasing the number of panels is clear. The most notable is observed in Fig. 3.11, with 360 panels. The difference is quite obvious and points out the reason why a panel sensitivity investigation is required. By increasing the number of panels a more accurate solution is obtained. This increase in the number of panels does not have a significant effect on the linear lift region predictions, but it has a major effect in capturing the overall shape of the experimental data. The increase in panel numbers results in a more accurate prediction in the high angles of attack region, at stall conditions. It also allows for more accurate prediction at low angles of attack.

It is also observed that the XFOIL predictions and the experimental data are not quite in accordance, and yet again XFOIL is predicting inaccurate predictions, as is evident from Fig. 3.11. The offset of XFOIL predictions and experimental data is clear. Also, the effect of the amplification value, in Fig. 3.11, is evaluated. The effect is quite clear, with a tendency towards the experimental data. This increase in XFOIL predictions is a reflection of the quality of the wind tunnel, leading to a less accurate capture of the overall shape of the experimental data.

## 3.6. Conclusion

In conclusion, to ensure the highest level of accuracy, it is important to remember that an increase in the number of panels will allow for a higher accuracy of predictions in XFOIL. Thus, for further evaluation, the number of panels set on the analysis of an airfoil in XFOIL will be conducted at a number of panels of at least 360, ensuring the highest order of accuracy. This is evident from the validation study of the original XFOIL program, conducted in this section. Additionally, there is no limit to the available resources required to perform the analysis on. Thus, the maximum number of panels allowable on the software was used.

Each individual case will be analysed at different angle of attack increments, so as to ensure that complex shapes of the lift vs drag curve are captured. In the case of the NACA 0012 and NACA $63_3 - 418$ airfoils, the angle of attack increments will be at $1^\circ$ increments. This is because the overall lift-to-drag shape is not that complex when compared with the FX61-163, FX66-S-196 and E603 cases, that find their application in the design of sailplanes.

In addition, the validation of these airfoils shows that XFOIL struggles to accurately predict the performance of sailplane airfoils. This is due to the fact that sailplane airfoils are designed to create maximum lift with low drag. The result is an airfoil with strong curvature over the top and bottom. This is where XFOIL's fundamental mathematical models, panel configurations and assumptions are less efficient, as the program is less accurate at performance predictions with strong pressure gradients over the top and bottom of the airfoil. As will be seen in later sections and as was discussed in **Section 2.6**, fundamental issues with mathematical assumptions lead to the inaccurate predictions of XFOIL.

# 4. Chapter 4: Improvements made to XFOIL

From the investigations in the previous chapters it was realised that XFOIL requires some updates to its model to allow for lift and drag predictions to be in better agreement with experimental data. In this chapter, the proposed improvements to the XFOIL source code will be discussed, as explained by Ramanujam, Ozdemir, and Hoeijmakers (2016) and Ramanujam and Ozdemir (2017). An overview was given in **Section 2.6**. Details on what the authors did to improve upon the less accurate assumptions will be become clear in this section for the drag improvements. A mathematical correction was derived to allow for improved drag predictions. It was shown that underprediction of the boundary layer quantities were the cause of the discrepancy in the momentum thickness calculations. For the proposed improved lift predictions it was noted that an inviscid solution is used to find the solutions to a viscous analysis. Both methods require knowledge of potential flow, as these updates are not changes to manipulate and randomly change values to improve XFOIL prediction, but are logical and scientifically correct.

The proposed drag improvements are based on mathematical changes as a corrected momentum thickness is calculated from a formula derived by Ramanujam, Ozdemir, and Hoeijmakers (2016).The proposed lift improvements are presented as a recalling of the calculated edge velocity. This is then used to update the vorticity strengths to include a viscous wake trajectory.. Some of the source codes had to be changed to allow for a condition to be met before continuing with normal calculations. All the work done here was done meticulously as XFOIL utilises FORTRAN to perform its calculations and it is easy to inadvertently change code that is best left alone. A complete inspection of the source code was required to obtain the location of the lift and drag calculations. Important aerodynamic assumptions are also necessary and to be kept in mind. Parameters are described in various '.INC' files within the source codes, to assist the parameter hunting process. More detail on how this is obtained is given in the following subsections.

Note that the purpose of this section is to give insight into how the implementation of these intended improvements were done. The validation of this new improved method will follow in later chapters of the dissertation.

## 4.1. XFOIL program execution

To better understand how and where these improvements were implemented to XFOIL, an overview of the XFOIL program execution steps is given to clarify the process. First, the software requires some user inputs to initiate an aerodynamic flow analysis. These are standard steps taken when performing a flow analysis in XFOIL. The user supplies the program with airfoil coordinates as input data. Panels are then generated over the airfoil contour and can be adjusted by the user in the 'PPAR' function. After this process the influence matrix is set up. To perform a flow analysis, the user can prompt the 'oper' operation to initiate an inviscid solution. An angle of attack input then establishes the stream function and the source and vortex distributions are superimposed onto the airfoil contour. The user can then initiate the viscous solutions by prompting 'visc' and adjusting the Reynolds number. With the viscous flow analysis active, an angle of attack is required as input to the viscous solution. In Fig. 4.1 an illustration is shown of the subroutine execution of XFOIL to perform a viscous flow analysis. The exact subroutines in XFOIL can be found in **Appendix A**.

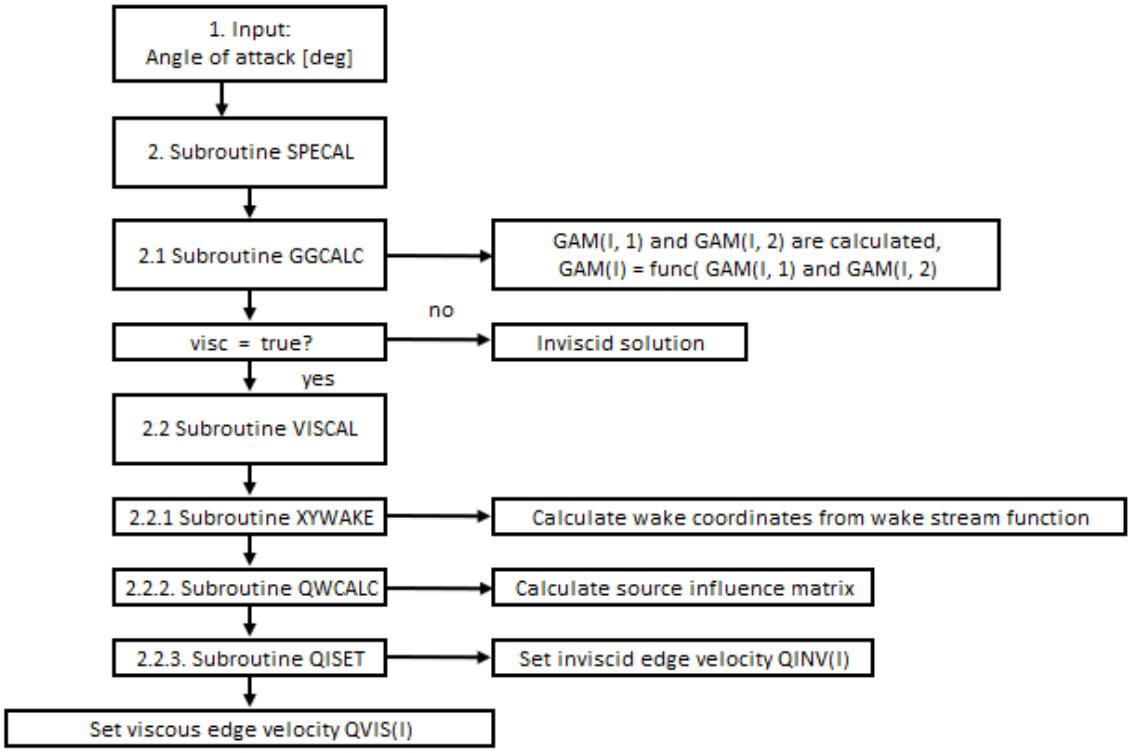


**Figure 4.1.** XFOIL program execution steps

If an angle of attack is specified, XFOIL then utilises subroutine 'SPECAL' to perform calculations. 'SPECAL' then calculates the values of the vorticity strength at the top of the airfoil as well as at the bottom. If only an inviscid solution is required, vorticies with the unknown strengths are then superimposed on each panel through $GAM(I) = f\left(GAM(I,1),\ GAM(I,2)\right)$, recall Eqn. (2.47). This value, $GAM(I)$, represents and invisid solution of the vortex strengths.

If the viscous analysis is prompted, XFOIL then utilises the subroutine 'VISCAL' to calculate and set the viscous parameters. First, to initiate the viscous calculation, a wake is required. Subroutine 'XYWAKE' calculates the wake coordinates from the wake stream function, which in itself is a function of the vortex strengths. The subroutine 'QWCALC' is then utilised to set up the source influence matrix and calculate the viscous parameters. From Fig. 4.1, it is clear that from the calculated inviscid matrix, the edge velocity is obtained. These parameters are then recalled into the 'xfoil.f' source file to calculate the drag and lift coefficients and other

polar parameters.

## 4.2. Drag improvements implementation

As mentioned by Ramanujam, Ozdemir, and Hoeijmakers (2016), there is an overall tendency of panel methods to overpredict the boundary layer edge velocity that causes an underprediction of the momentum thickness, $\theta$. Therefore, the error in momentum thickness, $\Delta\theta$ was proposed to correct $\theta$ at a point (1 chord length behind the trailing edge) in the far downstream wake. It was argued that the momentum thickness definition is different from what is calculated by XFOIL, at that point. The definition of momentum thickness is given as the momentum loss in the x- and y-directions and not a function of the streamwise direction, nor a function of the boundary layer edge velocity, but a function of the freestream velocity, in the far downstream wake. Thus, the proposal was that the error in momentum thickness prediction is the difference between the actual momentum thickness and the predicted momentum thickness.

$$\Delta\theta = \theta_\infty - \theta_e \tag{4.1}$$

which is then rewritten as,

$$\Delta\theta = \int_0^\delta \frac{u}{U_\infty}\left(1 - \frac{u}{U_\infty}\right) dy - \int_0^\delta \frac{u}{U_e}\left(1 - \frac{u}{U_e}\right) dy \tag{4.2}$$

This equation can then be simplified to,

$$\Delta\theta = \left(\frac{U_e}{U_\infty} - 1\right)\left[\theta_e + \frac{U_e}{U_\infty}(\delta_e^* + \theta_e - \delta)\right] \tag{4.3}$$

The authors noted that $\delta_e^* = \int_0^\delta \left(1 - \frac{u}{U_e}\right) dy$ and also that in XFOIL, $H_1 = \frac{\delta - \delta_e^*}{\theta_e}$. Again, Eqn. (4.3) can be rewritten to obtain,

$$\Delta\theta = \theta_e\left(1 - \frac{U_e}{U_\infty}\right)\left[\frac{U_e}{U_\infty}(H_1 - 1) - 1\right] \tag{4.4}$$

Drela, 1989 used a simplified form of $H_1$,

$$H_1 = 3.15 + \frac{1.72}{H_k - 1} \tag{4.5}$$

This expression is based on experiments that correlate the expression, $H_1 = \frac{\delta - \delta_\infty^*}{\theta_\infty}$, thus, using the edge velocity-based values will result in an overprediction of the $H_1$ value (Ramanujam, Ozdemir, and Hoeijmakers, 2016). From Eqn. (4.5) it is clear that the value of $H_1$ is only dependent on the kinetic shape parameter, $H_k$, which is the same as the shape factor with incompressible flows. It has been mentioned that for the value where $H_1$ tends to unity, the value of $H$ becomes significantly high, which occurs at the far downstream position where the value of $H$ tends to unity. A correction to the value of $H_1$ was suggested, by introducing a constant multiplier, $g$, to $H_1$, with condition $g < 1$. This expression is shown in Eqn. (4.6),

$$\Delta\theta = \theta_e\left(1 - \frac{U_e}{U_\infty}\right)\left[\frac{U_e}{U_\infty}(gH_1 - 1) - 1\right] \tag{4.6}$$

This equation can then be rewritten into its final form and then substituted into the Squire-Young drag model.

$$\theta_\infty = \theta_e + \Delta\theta = \theta_e \left(1 + \left(1 - \frac{U_e}{U_\infty}\right)\left(\frac{U_e}{U_\infty}(gH_1 - 1) - 1\right)\right) \tag{4.7}$$

The correction multiplier value, g, is dependent on the turbulent boundary layer method that is used by the solver. The authors then derived an expression for this value.

$$g = \frac{A^2 B}{42.084(1 + x_{C_{\tau EQ}})} \tag{4.8}$$

with A and B the values of the $G-\beta$ equilibrium locus, and $x_{C_{\tau EQ}}$ is the equilibrium shear stress coefficient multiplier for the wake, which in the case of XFOIL is equal to one. This results in the value of $g$ being equal to 0,4 for the XFOIL solver. A detailed view of the improvement can be found in **Appendix A.1**, as implemented into XFOIL source codes.

## 4.3. Lift improvements implementation

The lift improvements were not supplied with direct code, instead the reader is given a new approach to the perceived improved lift predictions. This method includes a viscous wake trajectory to allow for predictions that are in better agreement with experimental results. If angle of attack is specified, the wake trajectory is taken from an inviscid solution at the specified angle of attack (Drela, 1989). In general, viscous effects reduce the lift produced by an airfoil (Ramanujam and Ozdemir, 2017). The new approach that had been proposed was to initially calculate the boundary layer solution with the inviscid wake trajectory and then use the resulting edge velocity distribution to update the vorticity distribution and subsequently the stream function. A detailed explanation is located in **Appendix A.1.2**, and it includes the XFOIL source code and show how these changes were implemented.

To explain what changes had to be made to XFOIL to include this viscous wake trajectory, consider Fig. 4.1. When an angle of attack is specified, XFOIL then utilises the subroutine 'SPECAL' to find the inviscid solution. It is clear from Fig. 4.1, that at this point the vorticity strengths had been calculated. If the viscous solution is invoked, the program then utilises the subroutine 'VISCAL' to find the viscous solution to calculate the viscous edge velocity. To include this edge velocity, one makes use of Eqn. (2.72), to update the vorticity strengths.

The new approach also requires some editing of the normal execution of XFOIL routines. A change had to be made on how the program executed its calculations to include the viscous wake. This was achieved by allowing the program to prompt an angle of attack. When the user specifies the angle of attack, XFOIL must perform its usual calculations until the quantity QVIS(I) is calculated. This quantity, QVIS(I) is known as the viscous edge velocity and is superimposed on each point, I, on the airfoil contour. After this step is completed, the program then has to check if the value of QVIS(I) exists. If it does, the vorticity distribution, GAM(I), should then be updated to the edge velocity, QINV(I), through Eqn. (2.72). To achieve this the program has to recall the subroutine 'SPECAL' and update GAM(I) with the edge velocity. From there on XFOIL can continue its normal execution steps to perform an aerodynamic analysis. By implementing this new approach, one is able to obtain a viscous wake, because with the new vorticity distribution a new stream function is calculated and the trajectory of the wake is changed. A reduced downwash of the wake was expected and recorded by Ramanujam and Ozdemir (2017).

## 4.4. Method verification

To verify that the that the proposed methods have been implemented correctly, a verification step was done to make sure this was the case. Ramanujam, Ozdemir, and Hoeijmakers (2016) and Ramanujam and Ozdemir (2017) implemented these changes to RFOIL and validated the method. In this study, the methods were implemented in XFOIL. The major difference between XFOIL and RFOIL is that RFOIL can better predict the performance of thick airfoils. The verification step was divided into two subsections, namely, the verification of drag and lift.

### 4.4.1. Improved drag method verification

Ramanujam, Ozdemir, and Hoeijmakers (2016) proposed a formulation to correct the underpredicted momentum thickness at a point in the wake downstream (1 chord length). In XFOIL, the drag coefficient of an airfoil is calculated by application of the Squire-Young model in the wake. This method is referred to as far-field drag estimation because the drag is calculated in the wake. From Le Roux and Bosman (2019), far-field methods of drag estimation are insensitive to discrepancies in drag, as near-field methods are overly sensitive to grid definition that yield artificial drag within the total drag estimation. From Ramanujam, Ozdemir, and Hoeijmakers (2016) and Eqn. (4.7) the formulation of the corrected momentum thickness is given. By applying the Squire-Young model of drag estimation, this new equation is obtained,

$$c_d = \frac{2}{c}(\theta)\left(\frac{u_e}{U_\infty}\right)^{\frac{5+H_{TE}}{2}} = \frac{2}{c}(\theta_e + \Delta\theta)\left(\frac{u_e}{U_\infty}\right)^{\frac{5+H_{TE}}{2}} \tag{4.9}$$

The parameters $\theta$, $\frac{u_e}{U_\infty}$ and $H_{TE}$ are included in the equation to determine the drag coefficient. The verification analysis was done at an angle of attack of 4°, with Re = $3{\times}10^6$ and $N_{crit}$ = 9.

| Airfoil | NACA 0012 |
|---|---|
| $\theta$ | $3.181 \times 10^{-3}$ |
| $\frac{u_e}{U_\infty}$ | 0.993 |
| $H_k$ | 1.046 |
| $H_1$ | 40.375 |

**Table 4.1.** XFOIL calculated parameters for $Re = 3 \times 10^6$ and $N_{crit} = 9$ at 4°

Substituting these values for each parameter, as calculated by XFOIL, into the correction equation Eqn. (4.6), the value of the delta theta is determined to be equal to $3.063 \times 10^{-4}$. This value corrects the underprediction of the momentum thickness at a distance downstream in the wake. The obtained value of $\Delta\theta$, is then added to the XFOIL predicted momentum thickness, $\theta_e$; the Squire-Young model is then applied to calculate the corrected drag coefficient.

$$c_d = \frac{2}{1}(3.181 \times 10^{-3} + 3.063 \times 10^{-4})(0.993)^{\frac{5+1.046}{2}} = 0.00683 \tag{4.10}$$

When running an analysis in XFOIL with the new method and the same flow conditions, the same value is obtained as what was expected and calculated here by hand. Ramanujam, Ozdemir, and Hoeijmakers (2016) validated the proposed drag correction method implemented into XFOIL against experimental data but did not change the value of $N_{crit}$ to match the turbulence intensity of the wind tunnel. The results obtained from their validation can be used to verify whether the method had been correctly implemented in the current investigation using the same value of $N_{crit}$. During the verification investigation the lift improvements had not

yet been implemented and it can be observed that the new method has no effect on the lift predictions of XFOIL. This was to be expected as the method is only a numerical correction of the momentum thickness at a point in the wake where the streamwise and normal coordinates are equivalent to the $x$ and $y$ directions.

The new method was then verified against a range of angles of attack, corresponding to the range of results obtained by Ramanujam, Ozdemir, and Hoeijmakers (2016). The analysis was done from $-4°$ up to $12°$ with the same flow conditions ($Re = 3\times10^6$ and $N_{crit} = 9$). The results from the verification step can be observed in Fig. 4.2. The results show that the results from Ramanujam, Ozdemir, and Hoeijmakers (2016) and from the current study are in agreement with one another, suggesting that the method was successfully implemented in XFOIL.

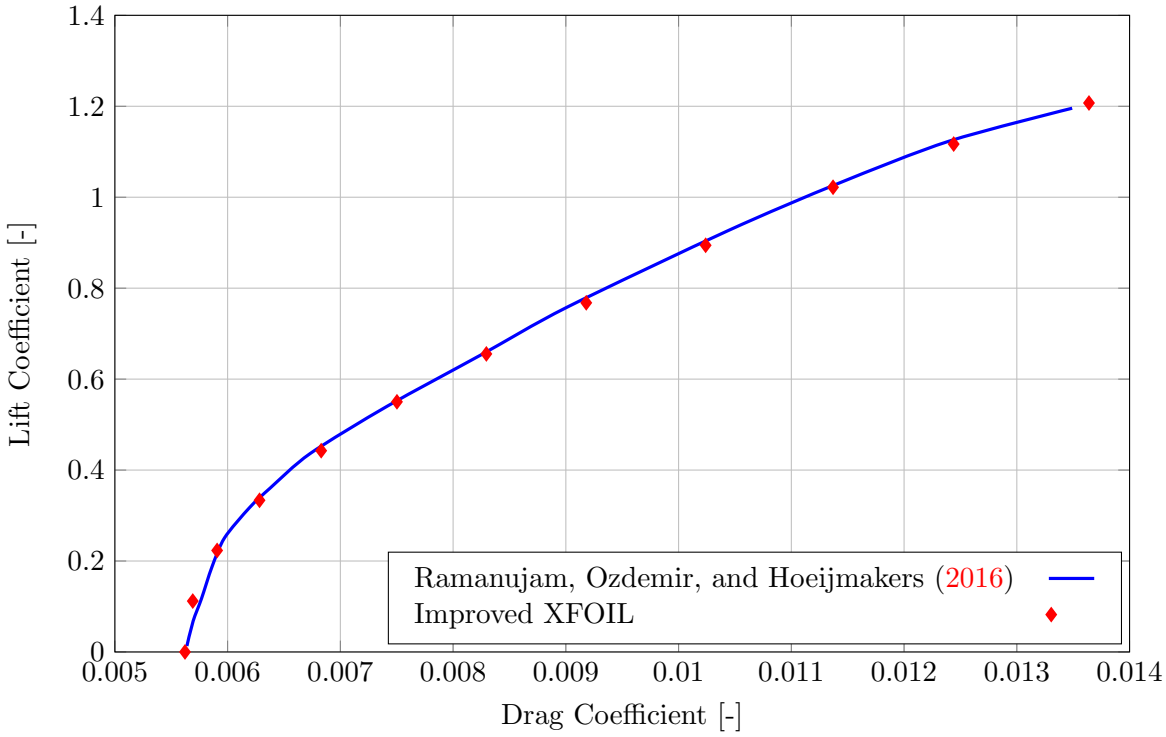


**Figure 4.2.** Verification results with $Re = 3 \times 10^6$ and $N_{crit} = 9$

### 4.4.2. Improved lift method verification

To verify the new approach that had been implemented to XFOIL, it was necessary to verify whether the changes in the source code perform as was expected and conform to the method proposed in Ramanujam and Ozdemir (2017). Thus, an update to the vorticity strengths was expected and was observed during the verification steps. The approach is to use the resulting edge velocity to update the vorticity strength distribution. To achieve this, the value of QINV(I) should update the GAM(I) parameter. This was achieved by allowing XFOIL to perform a normal aerodynamic analysis, then use the resulting QINV(I) to update the vorticity strength distribution, GAM(I). This solution seems to be simple but it required intensive study of the XFOIL source files to obtain and implement these changes. Other lift-improving studies are shown in **Chapter 6** under the subsection Recommendations.

Referring to **Appendix A.1.2**, the source code of how GAM(I) is calculated by XFOIL is shown in lines 2819 and 2820. Initially, XFOIL was allowed to perform its usual calculations. The code from Fig. A.3, shows that XFOIL must complete the analysis a second time to allow for the updating of the vorticity strengths. When the second loop is initiated, the program

should then use the QINV(I) value to update the GAM(I) distribution. To verify that this is the case one must consider the value of GAM(I) as it is updated. The following equations are used to calculate the GAM(I);

$$GAM(I) = GAMU(I,1)cos(\alpha) + GAMU(I,2)sin(\alpha) \tag{4.11}$$
$$GAM\_A(I) = -GAMU(I,1)sin(\alpha) + GAMU(I,2)cos(\alpha) \tag{4.12}$$

The values of GAMU(I,1) and GAMU(I,2) are calculated from the influence matrix. These values are calculated initially. The effect of the angle of attack on the GAM(I) distribution is then modelled by the above equations. To implement the update of the vorticity strengths, the equations are changed at the second iteration:

$$GAM(I) = QINV(I)cos(\alpha) + QINV(I)sin(\alpha)$$
$$GAM\_A(I) = -QINV(I)sin(\alpha) + QINV(I)cos(\alpha)$$

For verification purposes the airfoil HPH y n1 will be used for the analysis with Re = $1.5 \times 10^6$, $N_{crit} = 9$ at angle of attack = 4° and 14°. The first step in calculating lift prediction is determining the values of GAMU(I,1) and GAMU(I,2), which is calculated by XFOIL, at an angle of 4°. One can then calculate the expected value with the initial equations, for example,

$$\begin{aligned} GAM(1) &= GAMU(1,1)cos(4^\circ) + GAMU(1,2)sin(4^\circ) \\ &= 0.8385cos(4^\circ) + (-0.0572)sin(4^\circ) \\ &= 0.8324 \end{aligned}$$

This value is equal to the value produced by XFOIL. The full range of values for GAM(I) is calculated using the same equations for I = 1 to 360. The following table shows the expected value of GAM(I) against the XFOIL predicted value.

| I | QINVU(I,1) | QINVU(I,2) | Expected GAM(I) | XFOIL GAM(I) |
|---|---|---|---|---|
| 1 | 0,8385 | -0,0572 | 0,8324 | 0,8324 |
| 60 | 1,3147 | 0,7918 | 1,3668 | 1,3668 |
| 100 | 1,3665 | 1,5049 | 1,4681 | 1,4681 |
| 160 | 1,0947 | 5,7465 | 1,4929 | 1,4929 |
| 200 | -0,9939 | 9,6497 | -0,3183 | -0,3183 |
| 260 | -0,9921 | 1,3761 | -0,8937 | -0,8937 |
| 300 | -0,9914 | 0,8031 | -0,9329 | -0,9329 |
| 360 | -0,8385 | 0,0572 | -0,8324 | -0,8324 |

**Table 4.2.** Expected GAM(I) against XFOIL calculated values with first iteration calculations at $\alpha = 4^\circ$

The expected value is equal to the value predicted by XFOIL. At this angle of attack and vorticity strength distribution the lift coefficient prediction is equal to 1.061. This value is also obtained when performing a flow analysis, with the same flow conditions, on an unedited version of XFOIL. After the first iteration has been completed, the value of QINV(I) is obtained. With this value now known, the updated GAM(I) can be calculated,

$$\begin{aligned} GAM(1) &= QINV(1)cos(\alpha) + QINV(1)sin(\alpha) \\ &= 0.8324cos(4°) + 0.8324sin(4°) \\ &= 0.8885 \end{aligned}$$

With the full range of values of I, the expected value of the new GAM(I) can be calculated (Table 4.3). Note that XFOIL sets the value of QINV(I) = GAM(I), which gives the inviscid solution to a viscous analysis. According to Ramanujam and Ozdemir (2017), the resulting edge velocity distribution should be used to update the vorticity strengths. The following table shows the expected value of the new GAM(I) distribution against the XFOIL calculated value for the full range of I.

| I | QINV(I) | Expected updated GAM(I) | XFOIL updated GAM(I) |
|---|---|---|---|
| 1 | 0,8324 | 0,88846 | 0,88846 |
| 60 | 1,3668 | 1,45879 | 1,45879 |
| 100 | 1,4681 | 1,56695 | 1,56695 |
| 160 | 1,4929 | 1,59341 | 1,59341 |
| 200 | -0,3183 | -0,33974 | -0,33974 |
| 260 | -0,8937 | -0,95389 | -0,95389 |
| 300 | -0,9329 | -0,99573 | -0,99573 |
| 360 | -0,8324 | -0,88846 | -0,88846 |

**Table 4.3.** Expected GAM(I) against XFOIL calculated value with second iteration calculations at $\alpha = 4°$

The new values of GAM(I) produce a lift prediction of 1.061, the same value as obtained from the first iteration of the improved XFOIL. At a lower angle of attack the effect of the new approach is small, influencing only the lift predictions at higher angles of attack, reducing the maximum lift predicted. Also, this step can only be repeated once, as convergence to the final answer becomes an issue.

At an angle of 14° the effect of the new GAM(I) is more apparent, as can be seen from Fig. 5.25. When the same approach is used to update the vorticity strength at an angle of 14°, the following results are obtained.

| I | QINVU(I,1) | QINVU(I,2) | Expected GAM(I) | XFOIL GAM(I) |
|---|---|---|---|---|
| 1 | 0,8385 | -0,0572 | 0,7997 | 0,7997 |
| 60 | 1,3147 | 0,7918 | 1,4672 | 1,4673 |
| 100 | 1,3665 | 1,5049 | 1,6899 | 1,6899 |
| 160 | 1,0947 | 5,7465 | 2,4524 | 2,4524 |
| 200 | -0,9939 | 9,6497 | 1,3701 | 1,3701 |
| 260 | -0,9921 | 1,3761 | -0,6298 | -0,6298 |
| 300 | -0,9914 | 0,8031 | -0,7676 | -0,7676 |
| 360 | -0,8385 | 0,0572 | -0,7997 | -0,7997 |

**Table 4.4.** Expected GAM(I) against XFOIL calculated value with first iteration calculations at $\alpha = 14°$

With the first iteration of calculations a lift coefficient of 1.584 is obtained, corresponding to predictions of the unchanged version of XFOIL. With the second iteration of the calculations the following results are obtained, shown in Table 4.5, resulting in a 2.6% reduced lift prediction of 1.543.

| I | QINV(I) | Expected updated GAM(I) | XFOIL updated GAM(I) |
|---|---|---|---|
| 1 | 0,7997 | 0,9694 | 0,9694 |
| 60 | 1,4672 | 1,7786 | 1,7786 |
| 100 | 1,6899 | 2,0486 | 2,0486 |
| 160 | 2,4524 | 2,9728 | 2,9728 |
| 200 | 1,3701 | 1,6609 | 1,6609 |
| 260 | -0,6298 | -0,7634 | -0,7634 |
| 300 | -0,7676 | -0,9305 | -0,9305 |
| 360 | -0,7997 | -0,9694 | -0,9694 |

**Table 4.5.** Expected GAM(I) against XFOIL calculated value with second iteration calculations at $\alpha = 14°$

This study confirms that the changes to the XFOIL source code were correctly implemented as proposed by Ramanujam and Ozdemir (2017) and the results show that similar tendencies were observed. This approach was able to reduce the maximum predicted lift and was validated against experimental data to investigate the accuracy of the new method. The change in the vorticity strength was also made clear at each validation case, to verify that the method performed as expected.

### 4.4.3. Conclusion

The verification investigation was done to verify if the methods proposed by Ramanujam, Ozdemir, and Hoeijmakers (2016) and Ramanujam and Ozdemir (2017) were correctly implemented. Experimental data was excluded to show that the methods do not force numerical values to conform to experimental results. For the drag correction, the investigation merely showed that XFOIL's current definition of momentum thickness might not be equal to the actual definition of momentum thickness and provided a correction to obtain results that coincide with the actual momentum thickness definition, in the wake (Ramanujam, Ozdemir, and Hoeijmakers, 2016). An investigation was done on the NACA 0012 airfoil with $Re = 3 \times 10^6$ and $N_{crit} = 9$ and it was observed that the drag correction was implemented successfully, obtaining results that are in agreement with the results in Ramanujam, Ozdemir, and Hoeijmakers (2016). The implementation of the lift approach was verified and performed as was expected and proposed by Ramanujam and Ozdemir (2017). An update to the vorticity strengths, with the resulting edge velocity, was achieved as proposed. The results obtained are equivalent to what was outlined and a decrease in the maximum lift was achieved. Neither of the methods forces the numerical values to be in better agreement with experimental results, but addresses XFOIL's current lift and drag prediction methods and proposes corrections to include the viscous edge velocity distribution and actual momentum thickness definition.

## 4.5. Effects of the improved method on flow parameters

A study was completed to investigate the effects of the improved method on flow parameters. These parameters include the momentum thickness, displacement thickness, and the amplification ratio. The NACA 2412 airfoil was selected, and a flow analysis was completed on a standard XFOIL program, which was compared to the improved XFOIL predictions. Experimental results were excluded from this investigation as the results from both methods were compared to one another and to reflect on the effects of the improved method.

The flow analysis was done at a Reynolds number of $2 \times 10^6$, the reason is that this current study is focused on flow with high Reynolds numbers, as is the case of sailplane flight applications. The amplification ratio was set to $N_{crit} = 9$, which is a standard practise in XFOIL flow analysis at an angle of attack of $-7°, 0°, 9°$. To establish the number of panels required to obtain a converged answer, a panel study was done. The results are shown in Table 4.6,

| | $\alpha = -7°$ | | $\alpha = 0°$ | | $\alpha = 12°$ | |
|---|---|---|---|---|---|---|
| N | $C_L$ | $C_D$ | $C_L$ | $C_D$ | $C_L$ | $C_D$ |
| 160 | -0.5350 | 0.00855 | 0.2407 | 0.00548 | 1.4649 | 0.01661 |
| 260 | -0.5345 | 0.00861 | 0.2406 | 0.00550 | 1.4647 | 0.01659 |
| 300 | -0.5345 | 0.00861 | 0.2405 | 0.00549 | 1.4648 | 0.01658 |
| 360 | -0.5346 | 0.00860 | 0.2405 | 0.00550 | 1.4646 | 0.01668 |
| 400 | -0.5345 | 0.00860 | 0.2405 | 0.00550 | 1.4645 | 0.01661 |

**Table 4.6.** Convergence study (Re $= 2 \times 10^6$) with $N_{crit} = 9$

One can observe from Table 4.6, that at an angle of attack of 0° a converged answer was reached from a panel number of 360 panels also, from 300 panels a converged lift prediction was reached, but the drag prediction converged from 360 panels. At this angle of attack no flow separation is present over the NACA 2412 airfoil and the lift predictions of XFOIL is stable. This is not the case at flow separation, as the results of XFOIL decay at flow separation (see **Chapter 2**, Goldstein Singularity). This resulted in an oscillation of lift and drag predictions ($\alpha = -7°$ case) and also effects the convergence of the values ($\alpha = 12°$ case).

To circumvent this oscillation and non-convergence of the values, one can change the panel configuration by adjusting the bunching parameters of the panels. This was done by setting the Panel bunching parameter to 2, TE/LE panel density ratio to 0.3 and adjusting the panel area refinement at the top and bottom side to capture critical areas, in this case the trailing edge. The results are shown in Table 4.7,

| | $\alpha = -7°$ | | $\alpha = 0°$ | | $\alpha = 12°$ | |
|---|---|---|---|---|---|---|
| N | $C_L$ | $C_D$ | $C_L$ | $C_D$ | $C_L$ | $C_D$ |
| 160 | -0.5352 | 0.00859 | 0.2408 | 0.00544 | 1.4665 | 0.01650 |
| 260 | -0.5348 | 0.00859 | 0.2406 | 0.00548 | 1.4648 | 0.01660 |
| 300 | -0.5345 | 0.00860 | 0.2405 | 0.00549 | 1.4646 | 0.01659 |
| 360 | -0.5346 | 0.00860 | 0.2405 | 0.00550 | 1.4635 | 0.01664 |
| 400 | -0.5346 | 0.00860 | 0.2405 | 0.00550 | 1.4635 | 0.01664 |

**Table 4.7.** Panel bunching study (Re $= 2 \times 10^6$) with $N_{crit} = 9$

By observation of Table 4.7, a clear convergence of the lift and drag prediction is noticed. At an angle of attack of $-7°$ convergence was reached at a higher value as was predicted by Table 4.6. This was not observed at the angle of attack of $-12°$ as the predicted lift coefficient was lower than was predicted previously. For the angle of attack 0°, the values converged to the same values as in the previously case, supporting the case that XFOIL's lift and drag predictions are less stable near flow separation.

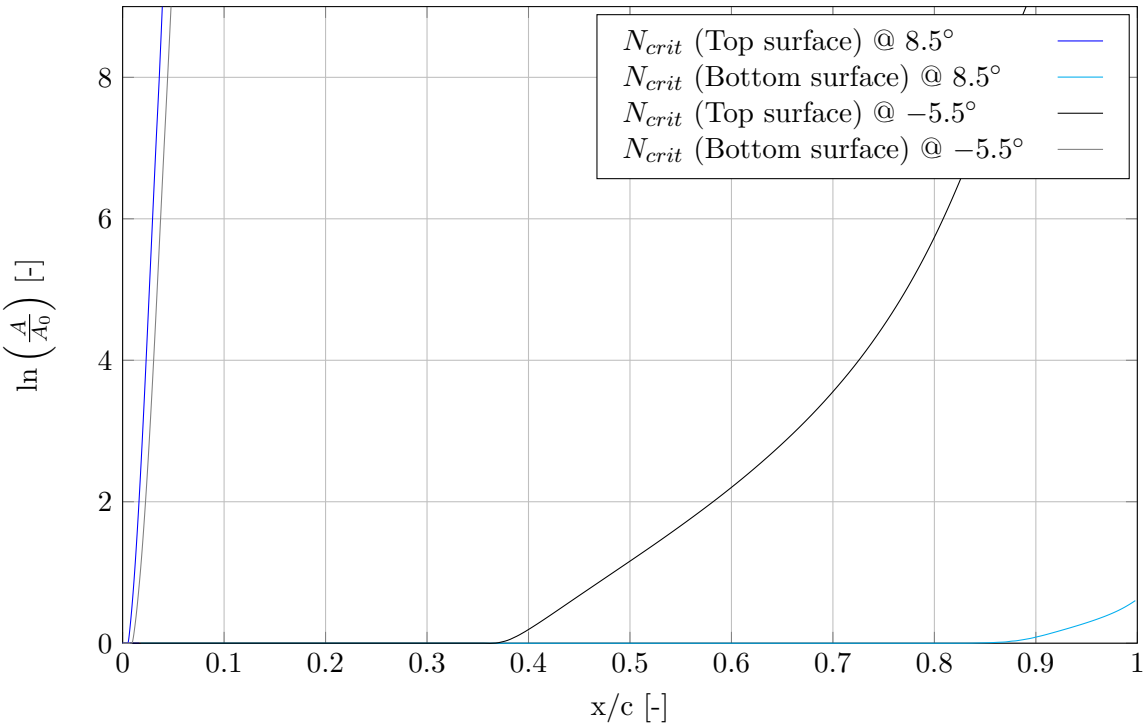


**Figure 4.3.** Amplification ratio with $Re = 2 \times 10^6$ and $N_{crit} = 9$

From Fig. 4.3, it can be observed that flow separation occurs at an angle of attack of 8.5°. The amplification of the wave amplitudes is characterised with a steep incline of the amplification ratio curve. At $x/c = 0.04$ the amplification ratio reaches the values of $N_{crit} = 9$ and the flow is separated from the top surface. It can be noted that the flow on the bottom surface is still attached to the airfoil surface. When the angle of attack was changed to −5.5° the flow become separated at both the top and bottom surfaces at $x/c = 0.85$ (top surface) and $x/c = 0.07$ (bottom surface).

### 4.5.1. Flow parameter study

When Fig. 4.4 is considered the effects of the improved method is clear and corresponds to what Ramanujam and Ozdemir (2017) found in their study and development of the improved XFOIL method. A clear reduction in the maximum predicted lift is observed. Ramanujam and Ozdemir (2017) expressed their concern that XFOIL uses the in-viscid solution to determine the viscous solution of the airfoil lift characteristics. Their proposal was to include a viscous edge velocity (resulting from the first flow solution) to update the vorticity strength distribution over the airfoil panels to obtain a viscous edge velocity (more detail in **Chapter 5**). The change in drag predictions are also apparent and the effects of the improved method was observed. The drag predictions of the improved method are shifted upwards, corresponding to the delta proposed by Ramanujam, Ozdemir, and Hoeijmakers (2016).

At 18° angle of attack a difference in lift and drag predictions is noticed from Fig. 4.4 and Fig. 4.5. To better understand what is causing this difference, the change in parameters at that point was investigated. An investigation was done to study the effects of the improved method on the momentum and displacement thickness and additionally the effect of the proposed method on the transition model of XFOIL.

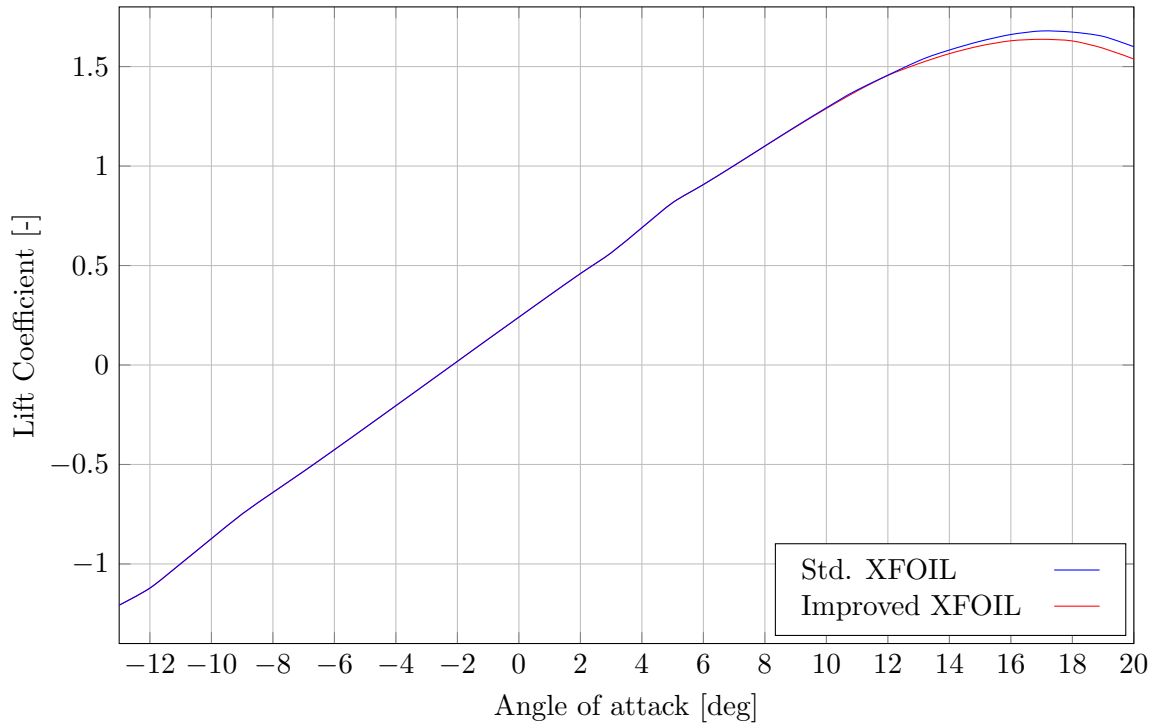


**Figure 4.4.** Standard vs Improved XFOIL method lift predictions with $Re = 2 \times 10^6$, $N_{crit} = 9$ and $\alpha = 18°$

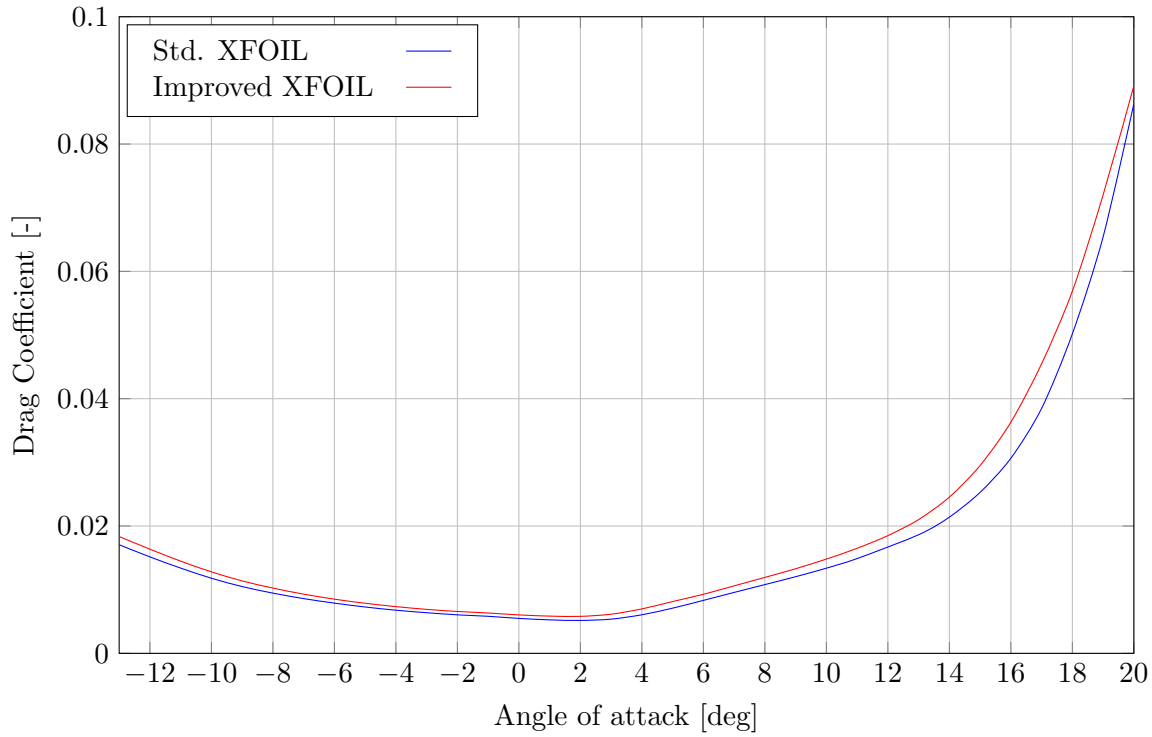


**Figure 4.5.** Standard vs Improved XFOIL method drag predictions with $Re = 2 \times 10^6$, $N_{crit} = 9$ and $\alpha = 18°$

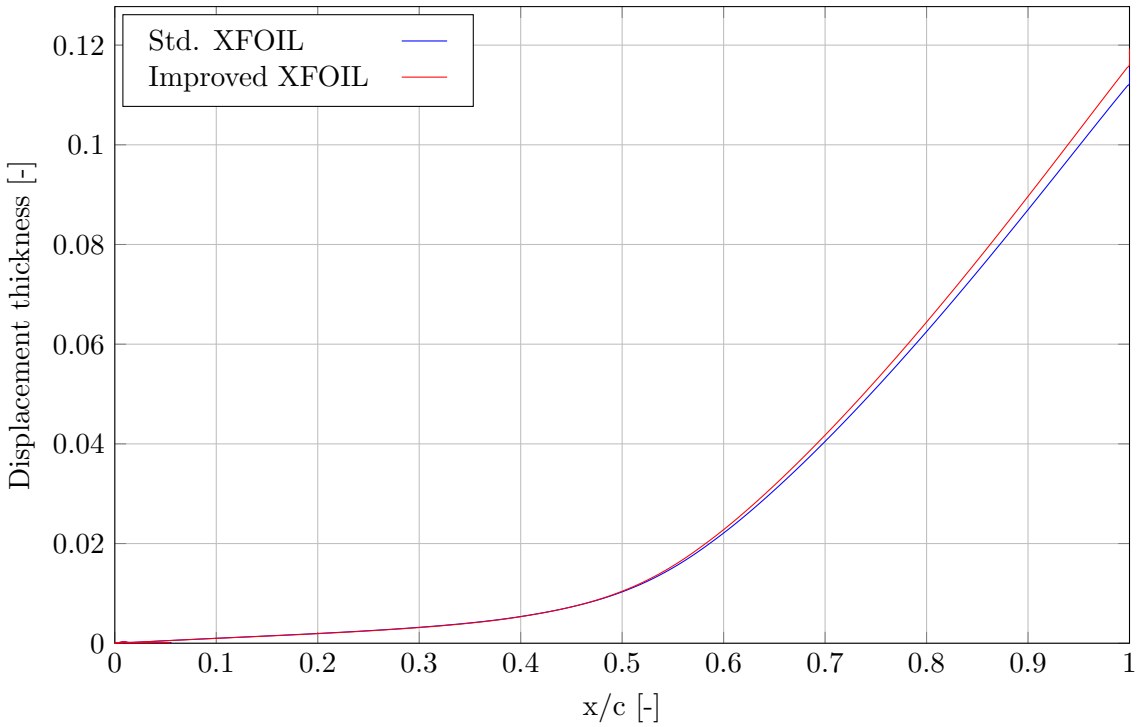


**Figure 4.6.** Displacement thickness (top surface) with $Re = 2 \times 10^6$, $N_{crit} = 9$ and $\alpha = 18°$

Displacement thickness is calculated using Eqn. (2.33). What was observe in Fig. 4.6 can be explained by the reduction of the edge velocity. A reduction in the edge velocity causes an increase in the displacement thickness, this can be explained by studying the displacement thickness equation. A reduction of the parameter $v_e$ will cause an increased predicted of the displacement of the air. The reduction of the edge velocity over the airfoil panels is observed in Fig. 4.9. The reduction in the edge velocity is due to the implementation of the improved lift method which reduces the edge velocity over the airfoil. It can also be observed that from x/c = 0.6, both methods divergence from one another and the divergence become more significant from this point. this is because the air has separated from the trailing edge. Ramanujam and Ozdemir (2017) argued that the XFOIL uses the in-viscid edge velocity distribution to calculate the lift at an angle of attack, this is further explained by Drela (1989) and was attributed to the unnecessarily long calculation time of the influence matrices in contrast to again in prediction accuracy. The effect of the improved drag prediction was not observed in the calculation of the displacement thickness. The reason being that the improved prediction of the momentum thickness was corrected in the Squire-Young drag calculation equation. The effect of the improved method has, less than 0.16% effect on the momentum thickness calculations. Fig. 4.7 shows the momentum thickness distribution over the airfoil panels. At around x/c = 0.6 a divergence in momentum thickness is observed, at the point where the flow has detached from the airfoil surface. The momentum thickness convergence to the same values at x/c = 0.8, with a difference of less than 0.1%. Thus, the effect of the lift improved method has a very small effect on the improved drag method, this was also observed in Ramanujam and Ozdemir (2017).

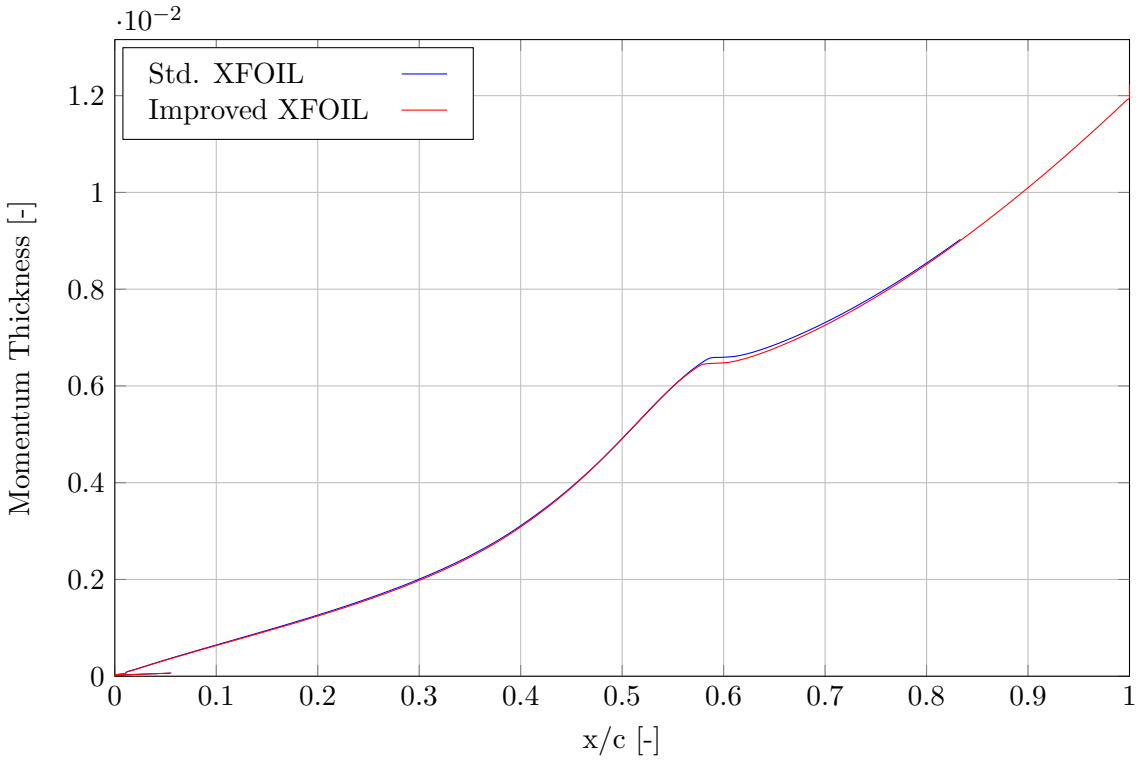


**Figure 4.7.** Momentum thickness (top surface) with $Re = 2 \times 10^6$, $N_{crit} = 9$ and $\alpha = 18°$

Flow separation is characterised with a jump in the momentum thickness predictions (Drela, 1989). This was observed at x/c = 0.0102 for the standard method and x/c = 0.0104 for the improved method. Also, a jump in the momentum thickness at around x/c = 0.6, in both methods, suggesting detached flow in this region. From Fig. 4.7, the difference in the location of detached flow is observed. Fig. 4.8 shows this occurrence in more detail. As with the previous case studies, the improved drag method imposes no effect on the prediction of the location of transition. This is not the case with the improved lift prediction as the edge velocity was influenced. According to Schlichting et al. (2003), transition occurs when flow waves in the boundary layer become unstable and flow separation is triggered (see **Chapter 2**). Flow velocity, flow turbulence intensity and angle of attack has a direct effect on the state of these waves. As previously mentioned, the new lift method reduces the edge velocity of the airfoil panels. This means that the method will also influence the separation point, which is determined from the amplification factor. Fig. 4.8 shows the amplification ratio of the waves in the boundary layer as predicted by the envelope $e^N$ method of transition prediction. The effect of the reduced edge velocity results in a lagged prediction of flow separation.

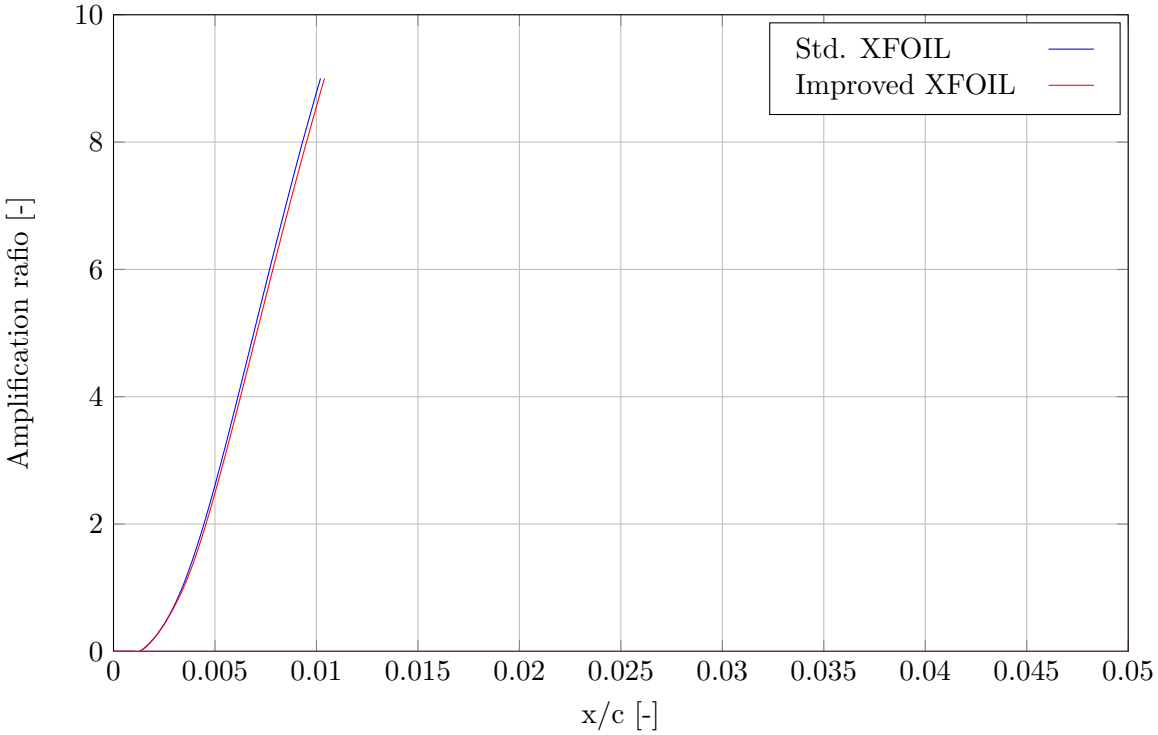


**Figure 4.8.** Amplification ratio (top surface) with $Re = 2 \times 10^6$, $N_{crit} = 9$ and $\alpha = 18°$

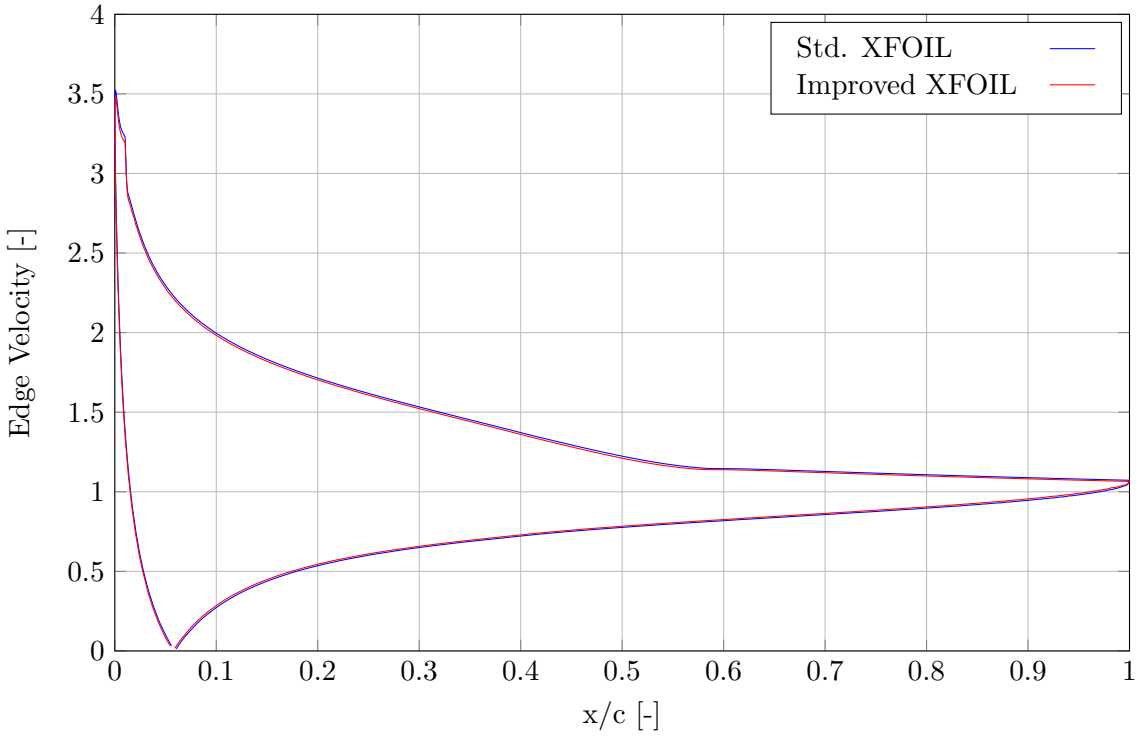


**Figure 4.9.** Edge Velocity with $Re = 2 \times 10^6$, $N_{crit} = 9$ and $\alpha = 18°$

# 5. Chapter 5: Results and discussion

After the implementation of the proposed improvement methods had been done, it was time to put this improved XFOIL to the test. The aerodynamic performance analysis was completed at the same calibration conditions as in **Chapter 3**. A panel number of 360 was used to simulate these airfoils, to ensure the highest order of accuracy.

It is important to note that the proposed lift improvements were developed for RFOIL, and the effects of the improvements were studied on XFOIL. Some deviation is expected as RFOIL utilises a different profile family, as previously mentioned. Nevertheless, an improvement in the current XFOIL predictions was expected and it will be shown to improve the maximum lift prediction. A vorticity strength study was also completed to study the effects of the new proposed approach.

Ramanujam and Ozdemir (2017) documented a change in the wake trajectory with the validation of the new approach that resulted in a reduced downwash of the wake. This was due to the fact that viscous effects will in general reduce the downwash effect at the trailing edge. A study was also completed to see if the same results were obtained regarding the improvement implementation. The results of all these studies can be found in this section of the report.

In aircraft development, it is important to reflect on an airfoil's lift-to-drag ratios. This gives clear indications of the airfoil's performance characteristics. From the experimental data a lift-to-drag vs angle of attack, curve was drawn up to investigate the accuracy of the improved XFOIL against experimental data.

## 5.1. NACA $63_3$-418: Improved XFOIL predictions

The most significant improvement between the lift and drag predictions will be the improvement made to the drag predictions, as changes in the lift are within the outer potential flow regions and the drag corrections are within the viscous boundary layer. This is evident from Fig. 5.1 that depicts the drag prediction of the improved method against experimental results.

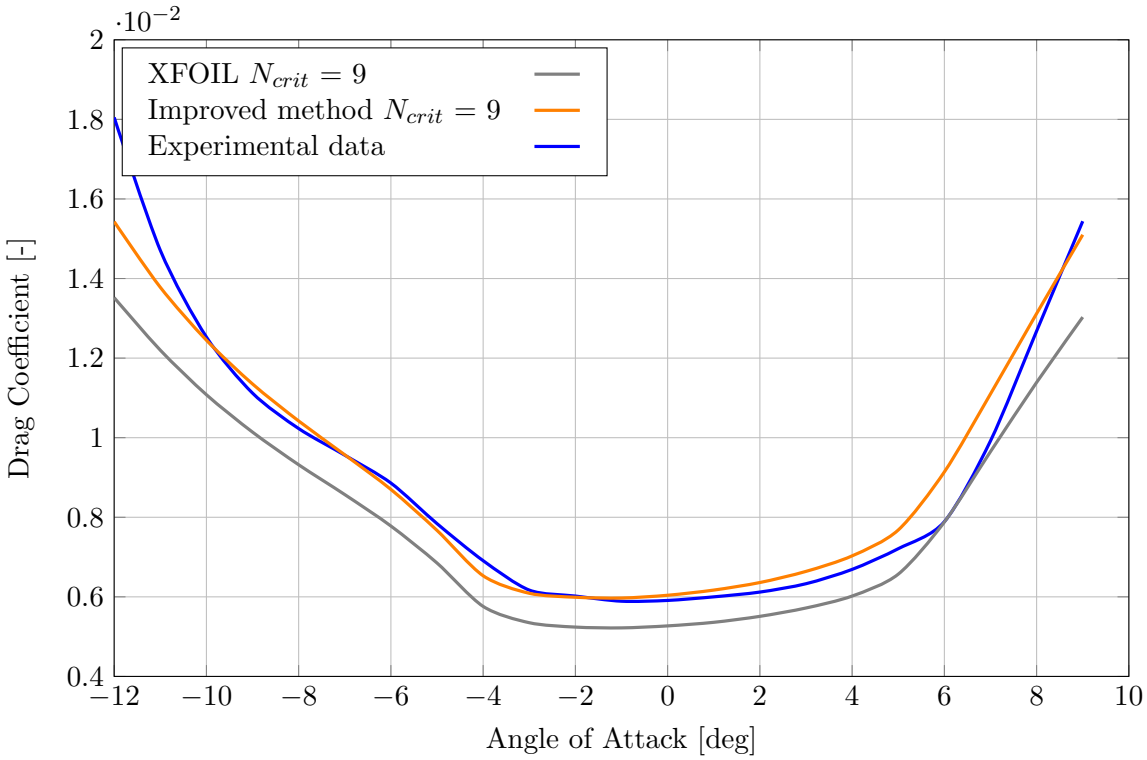


**Figure 5.1.** Improved NACA $63_3$-418 drag predictions with $N_{crit} = 9$ at Re = $3{\times}10^6$

From the figure the new method seems to shift the predictions with a 15% increase and produce values that coincide with the experimental data, with small deviations at $-9°$ and $-4°$. At angles from $-10°$ up to $5°$, the new method predicts the absolute value for the drag in closer proximity than the original method. This shift in the values of drag prediction is attributed to the corrected momentum thickness $\Delta\theta$. Major differences are observed at angles higher than 9° and lower than -12° due to the onset of flow separation (refer to the study in **Appendix D.1**). The proposed correction method leads to a major improvement in the standard XFOIL drag predictions. This also confirms what Ramanujam, Ozdemir, and Hoeijmakers (2016) found in their study. At an angle of attack ranging from 0° up to about 8° an overprediction of drag was observed, diverging from the experimental data. One can note that the standard XFOIL program was able to predict the drag prediction to between 6° and 7° in agreement with the experimental data. The proposed improved method leads to a less accurate prediction of drag in this range and shows that the new method is only a correction to the predicted momentum thickness at the far point in the wake (one chord length downstream) and does not contribute to changes in the calculation of the overall momentum thickness predictions on the airfoil.

The improved lift predictions are more subtle and less significant when compared to the standard XFOIL. This is because lift is calculated using the resulting vorticity strength distribution from the vortex panel flow method, which governs the outer flow region, where viscous effects are less dominant, thus having a smaller effect than viscous effects in the boundary layer. Nonetheless, an improvement to the lift predictions is observed in Fig. 5.2. The maximum lift is reduced and a less overpredicted maximum lift is obtained. Although both the original and new method

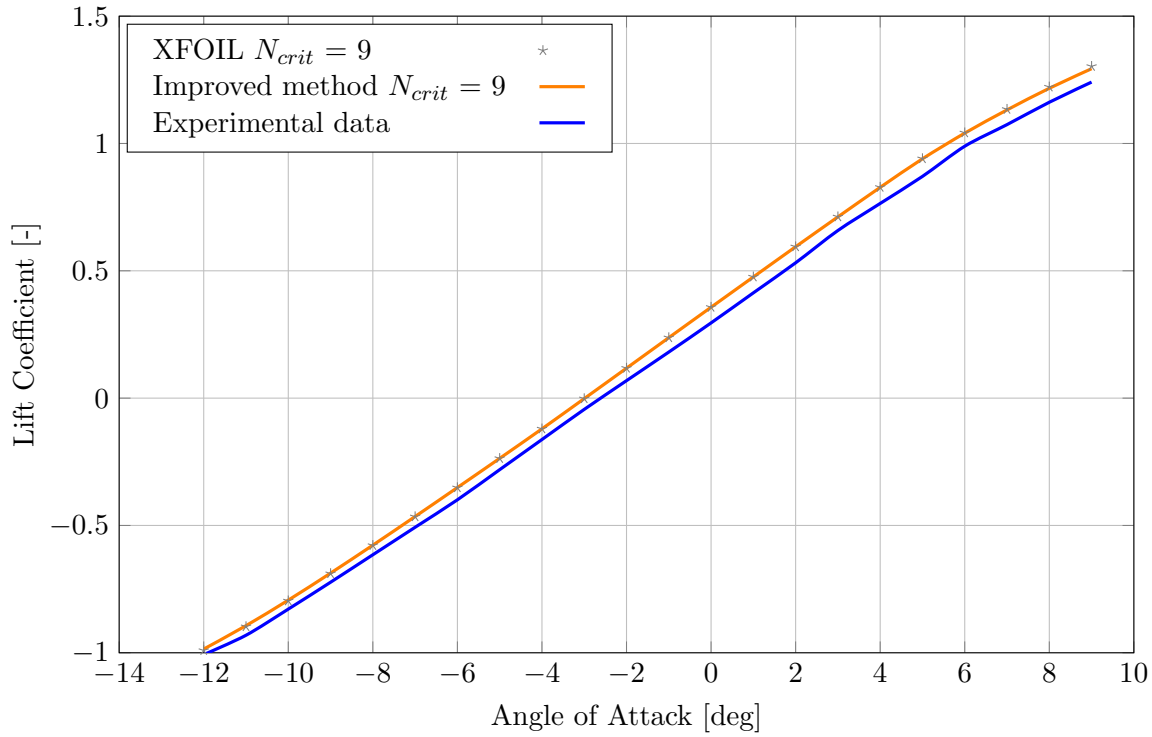


**Figure 5.2.** Improved NACA $63_3$-418 lift predictions with $N_{crit} = 9$ at Re = $3{\times}10^6$

show the same tendency of the slope of the lift curve, the absolute values of the methods differ from the experimental data. The cause of this can be traced back to the flaws in the numerical and experimental methods. Although these values do not line up exactly and absolute values differ, the tendency of the slope is equivalent. One can see clearly that as the angle of attack increases, so does the slope of the lift curve, which is still a problem with the panel methods to be studied (Ramanujam and Ozdemir, 2017).

The improvements to the lift and drag predictions of XFOIL are also noticeable when referring to Fig. 5.3. A significant corrected prediction of the curve is observed. Although the lift prediction is still overpredicted, the overall effect of the improved method is observed in the figure, with a reduction in the lift prediction at 9° by 0.7%. The major contribution being the improvements made to the drag prediction. Some inaccuracies are observed at a drag coefficient of 0.005 up to 0.013 at negative lift. The same can be said at a drag coefficient of 0.012 and higher, at positive lift.

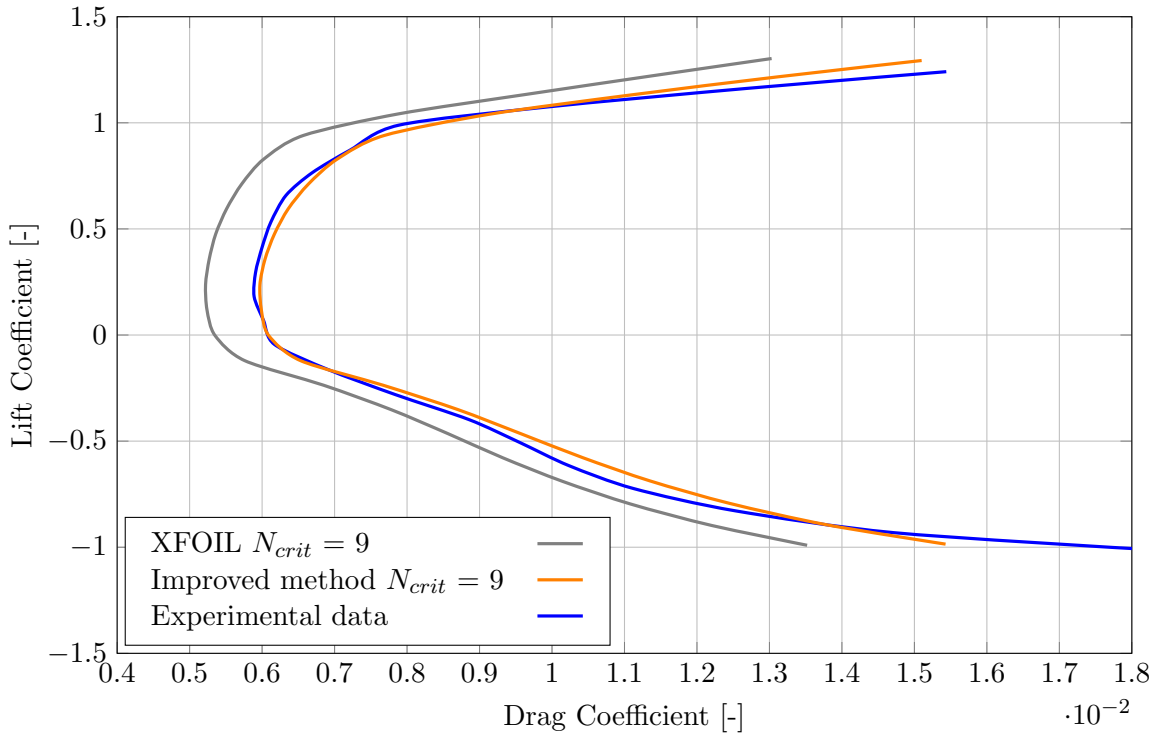


**Figure 5.3.** Improved NACA 63,3-418 $C_L$ vs $C_D$ with $N_{crit} = 9$ at Re = $3{\times}10^6$

Another way to visualise the improvements is to look at the lift-to-drag ratios at different angles of attack. This gives clear insight into how the lift and drag prediction has been improved upon at each angle of attack, as seen in Fig. 5.4. From this figure, the improvements are much clearer. As can be seen, XFOIL overpredicted the lift-to-drag ratios when referring to the experimental data. At high angles of attack XFOIL overpredicted the lift-to-drag ratio and at low angles of attack XFOIL underpredicts the lift-to-drag ratios. The improved method allows for more accurate predictions, which in turn results in higher accuracy of flight predictions. At angles of attack between -4° and 3° XFOIL was still inaccurately predicting the lift and drag ratio, but produced more accurate answers than the standard XFOIL program. From an angle of attack range of 5° up to 8°, this inaccuracy is observed, but once again the improved method produced more accurate predictions against the experimental data. From -4° up to -9° XFOIL trumps the improved method. From there on the improved method has corresponding tendencies than the experimental data. Also, the improved method slightly underpredicts the maximum lift-to-drag ratio.

The effect of using the resulting edge velocity distribution to update the vorticity strengths can be studied by investigating the vorticity distribution over the airfoil on each panel. This is shown in Fig. 5.5.

From Fig. 5.5 it is clear that using the edge velocity to update the vorticity distribution increases the magnitude of the vorticity distribution over the 360 panels. Conditions at the trailing edge remain the same. The difference is most significant at the leading edge of the airfoil and over

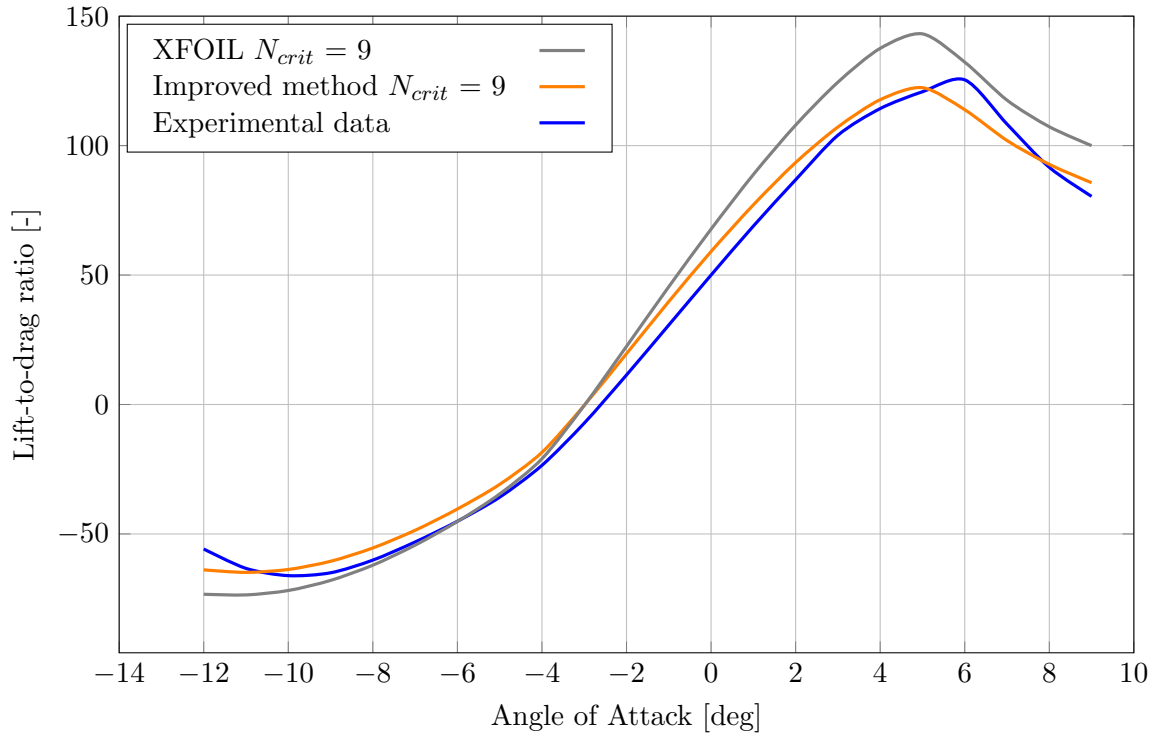


**Figure 5.4.** Lift-to-drag ratios at different angles of attack with $N_{crit} = 9$ at Re = $3{\times}10^6$

the top and bottom of it. Important to note, is that Drela (1989) calculates the value of the pressure coefficient, $C_p$ as $C_p = 1 - \left(\frac{\gamma_i}{U_\infty}\right)^2$ and $C_l = \int C_p d\vec{x}$. This means that an increase in the vorticity distribution will cause a decrease in the pressure coefficient distribution, which in turn will lower the value of the predicted lift coefficient, as is evident from the lift predictions from Fig. 5.2. In addition, this change in vorticity distribution will cause a change in the trailing edge region that calculate the wake trajectory. From Fig. 5.6 it is clear that the wake trajectory is changed, as expected from the study concluded by Ramanujam and Ozdemir (2017). The authors proposed that a reduced downwash of the wake trajectory will result in improved lift predictions.

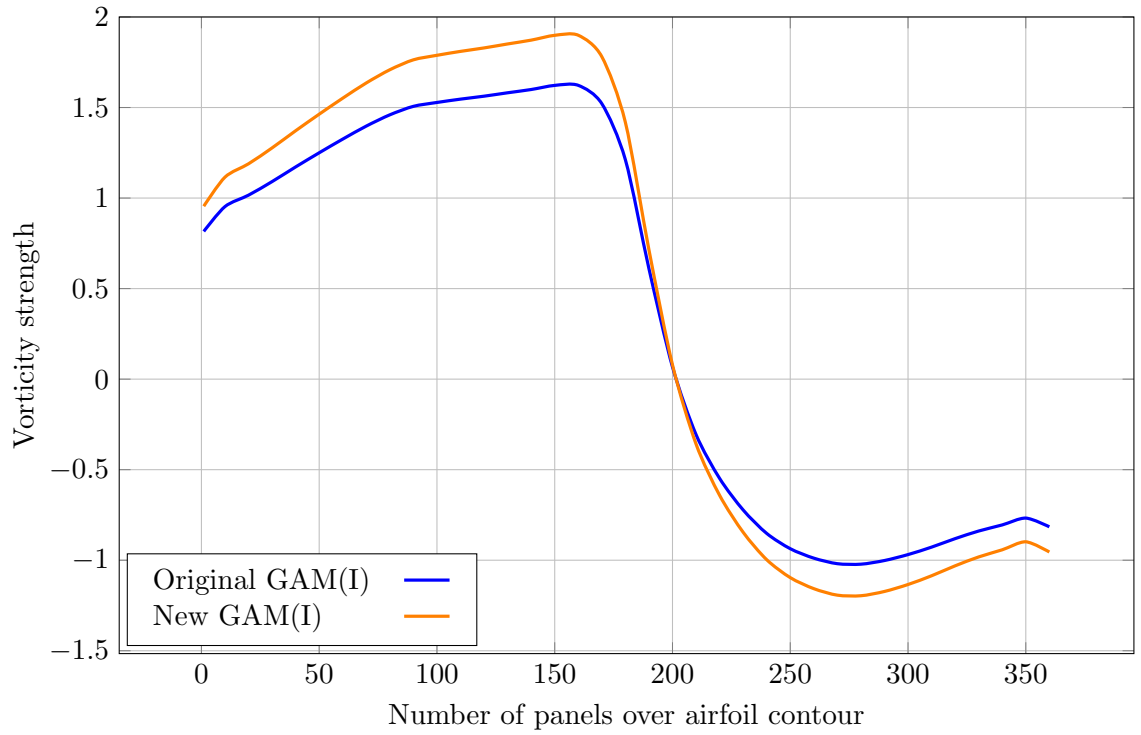


**Figure 5.5.** Vorticity strengh distribution over the airfoil panels at AoA 5 [deg] with $N_{crit} = 9$ and Re = $3{\times}10^6$

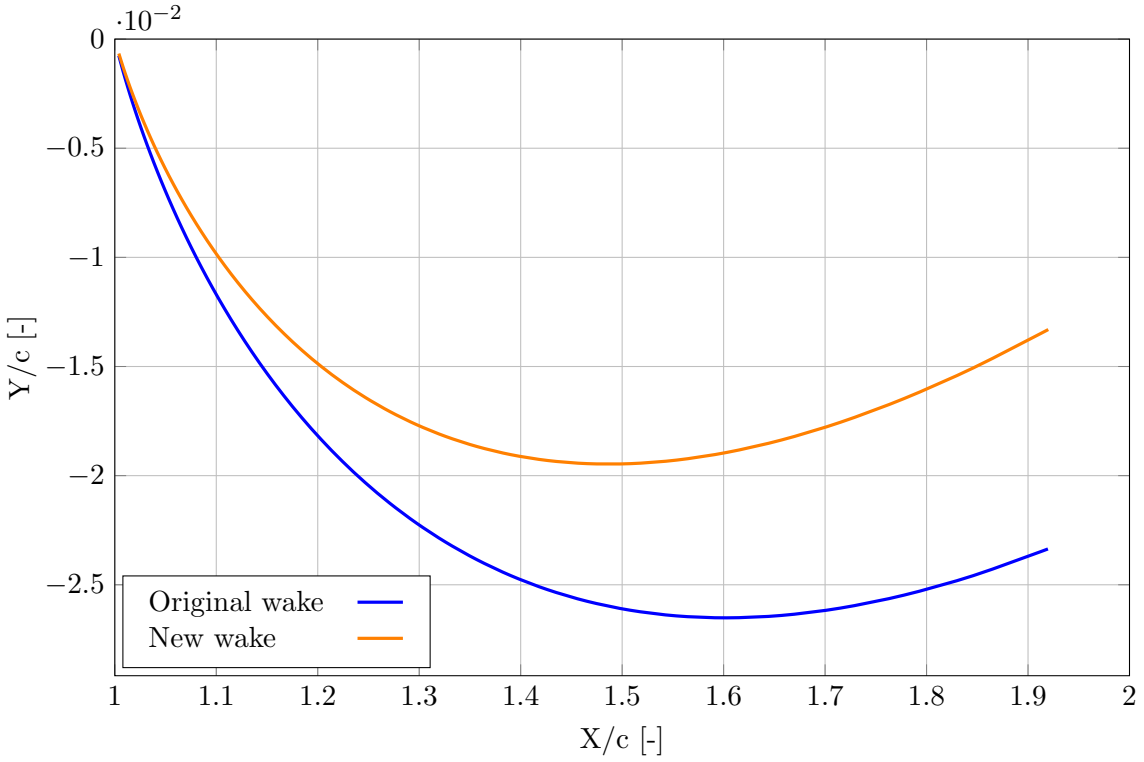


**Figure 5.6.** Wake trajectory of NACA 63,3-418 at AoA 5 [deg] with $N_{crit} = 9$ and Re = $3{\times}10^6$

## 5.2. FX61-163: Improved XFOIL predictions

In the case of this airfoil study, the improved method greatly improved upon the drag predictions of XFOIL, predicting almost exactly what the experimental data measured from $-2°$ up to $4°$. The improved method significantly (up to 11% increase) improved the accuracy of the drag prediction within the low angle of attack range, but still overpredicts the drag in higher angles of attack. Consider Fig. 5.7.

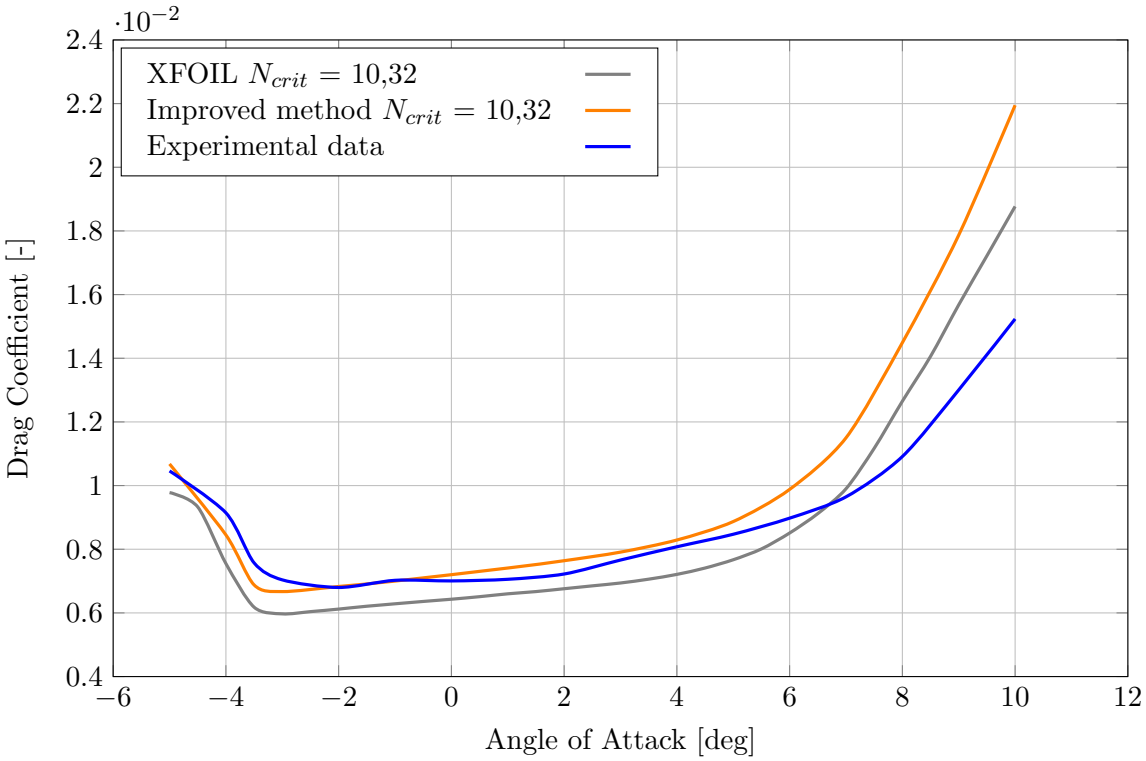


**Figure 5.7.** Improved FX61-163 drag predictions at Re = $1{,}5\times10^6$

From an angle of attack of $-5°$ up to $4°$ the new method significantly improved upon XFOIL standard predictions, with only small deviations from the experimental data. At around $0°$ and $4°$ the improved method slightly overpredicts the drag, compared with the experimental data. At $4°$ the method starts diverging considerably from the experimental data, with major differences noted from $8°$, where the drag is overpredicted. This is due to the inception of flow separation at this point (refer to study in **Appendix D.2**). This is evident from the standard XFOIL drag predictions and is still an issue that needs further study. Ramanujam, Ozdemir, and Hoeijmakers (2016) stated that a common issue with panel methods is the panel formulation that gives rise to the inaccurate predictions at higher angles of attack; the airfoil is broken up into smaller straight panels with no curvature..

The maximum lift prediction of this airfoil has been adjusted by the proposed method, and the overprediction has been reduced by a 2% decrease in prediction and the results are in better agreement with the experimental data. The improved method seems to have influenced the prediction of stall. This observation is made when considering the lift prediction at $10°$. As can be seen from Fig. 5.8, a maximum prediction has been reached by the new method that contradicts the original XFOIL predictions as the predicted lift has not yet reached a maximum.

The overall improvement of the data became clearer when considering the $C_l$ vs $C_d$ graph in Fig. 5.9, where within the linear lift region the new method better predicts the lift and

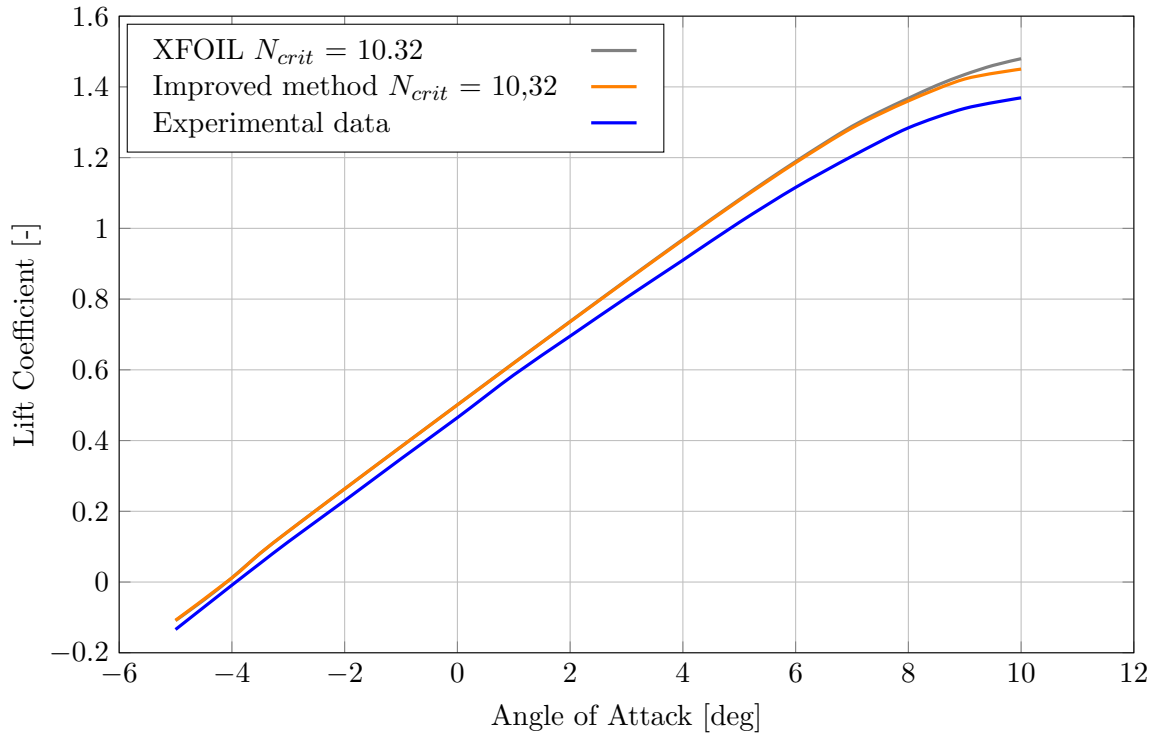


**Figure 5.8.** Improved FX61-163 lift predictions at Re = 1,5×$10^6$

drag and is in better agreement with the experimental data. Within the linear lift region the improved method better predicts the lift and drag and the results are in better agreement with the experimental data. The improved method does not give exact estimation in the linear lift region, as can be seen from $C_d = 0.007$ up to $C_d = 0.008$ but an overall improvement is documented. From this figure it is also possible to see the drag overprediction at the inception of stall conditions. This is characterised by the overextension of the improved method's predictions at around $C_d = 0.015$ up to $C_d = 0.022$. At low angles of attack the predictions have greatly improved in comparison with the experimental data.

The new method suggested that calculating momentum thickness with reference to the coordinate system along and normal to the streamwise direction and with the edge velocity as the reference flow velocity, is not consistent with the actual definition of the term. Momentum thickness is calculated along the x and y direction of the flow with the free-stream as the reference flow velocity. This definition originates from the flat plate theory, where the streamwise direction $\zeta = x$ - direction and $U_e = U_\infty$, for all values in the y-direction, which is not true for the case of an airfoil having a finite thickness. The statement can hold in the wake region where $\zeta = x$. As a result of having finite thickness with a curve, a pressure gradient over the airfoil surface is produced. Using the value of $U_e$ will result in an underprediction of the momentum thickness, as the value of $U_e$ is overpredicted because of the assumption that the value of the streamwise velocity, outside the boundary layer, is $U_e$ at all points normal to the airfoil surface. Thus is why a correction was developed, to make a correction to the current momentum thickness calculation. The actual definition of using the x- and y-coordinate system with $U_\infty$ as the reference flow velocity, will produce a larger value than the current formulation. This is because $U_\infty < U_e$ in the wake, and from the definition of momentum thickness, $\theta = f(\frac{1}{U})$, thus $\theta_\infty > \theta_e$ that results in $Drag_\infty > Drag_e$. So, to correct the value XFOIL predicts, one must add the value of difference between the actual definition and the current formulation $\Delta\theta$ to obtain the new corrected momentum thickness.

To illustrate this improved lift and drag prediction, consider the lift-to-drag ratio over a range

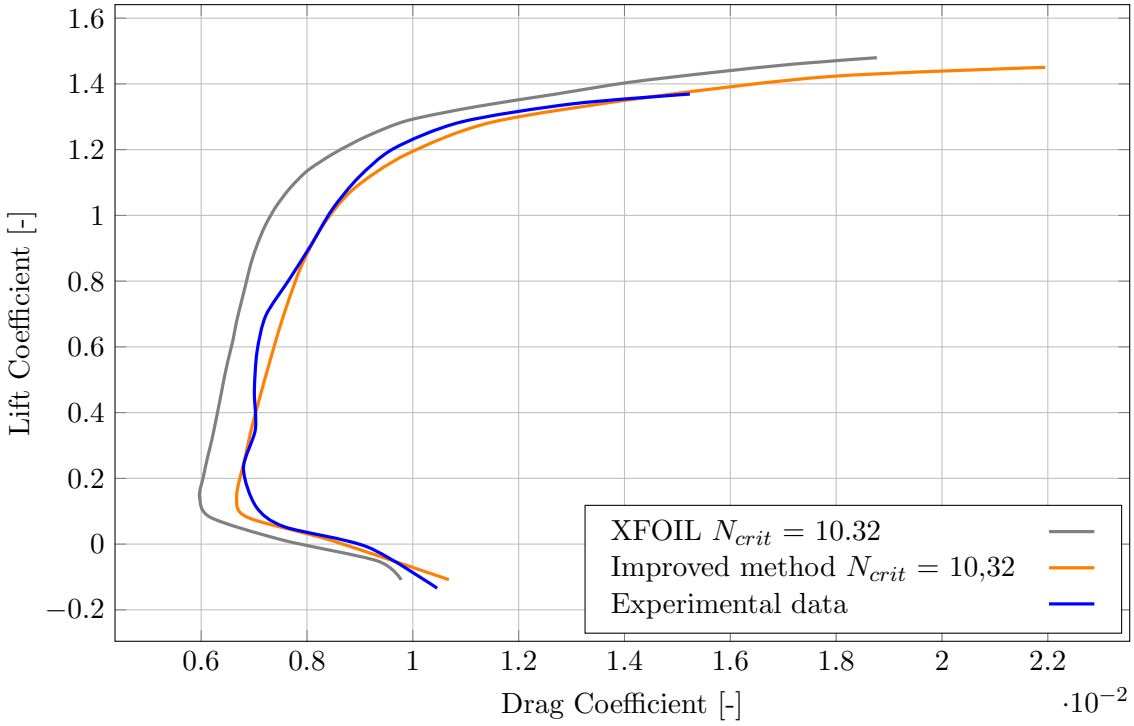


**Figure 5.9.** Improved FX61-163 lift vs drag graphs at Re = 1,5×10$^6$

of angles of attack, in Fig. 5.10. The most significant contribution to the improved lift-to-drag prediction is the improved drag prediction. From the previous figures it is clear that for this airfoil, the lift is overpredicted, and is only improved upon in a small range of values including the reduction of the maximum lift predictions. However, from the drag improvement predictions, it is clear the this method greatly improves upon the drag predictions with respect to the experimental results. The standard XFOIL predicts higher maximum lift-to-drag ratios at 4°, that have been corrected to a reduction in predicted maximum lift-to-drag ratio, that tend towards the experimental data. Both the standard XFOIL and the improved method overpredict the lift-to-drag ratios from −5° up to 5°. It can be seen that the improved method underpredicts the maximum lift-to-drag ratio and is predicted to be at its maximum at a lower angle of attack. It should be noted that between the angles of −5° up to 5° that the improved method is in better agreement with experimental data.

As seen in the previous airfoil case study, to improve on the standard XFOIL lift predictions, the proposed method is to update the vorticity distribution of the airfoil panels. This can also be seen in the case of this airfoil. The lift improvement method causes an increase in the vorticity distribution magnitude, that updates the stream function and changes the wake trajectory. as evident from Fig. 5.11 and Fig. 5.12.

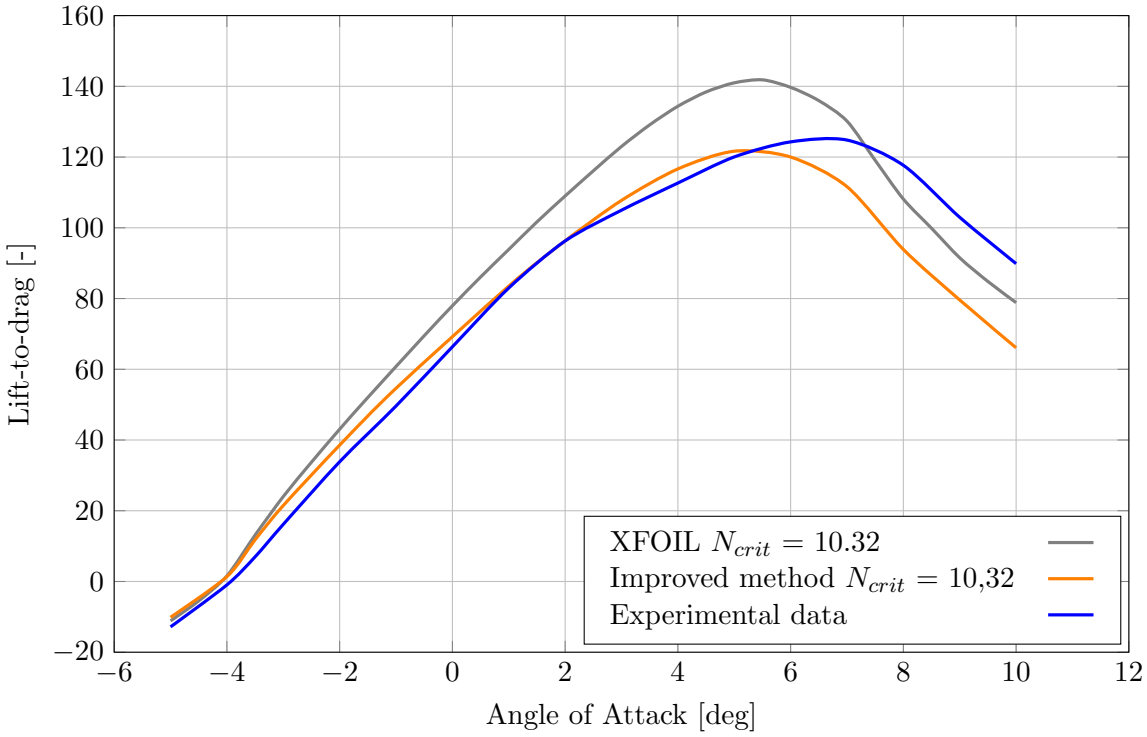


**Figure 5.10.** Lift-to-drag ratios at different angles of attack at Re = 1,5×10$^6$

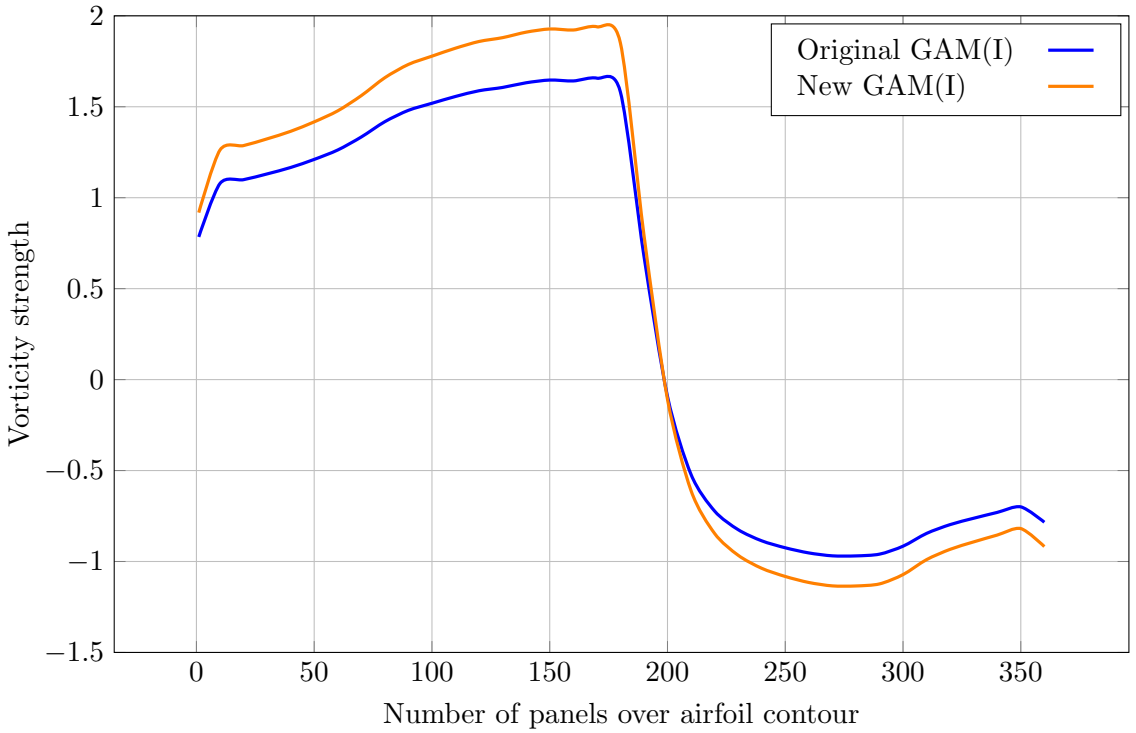


**Figure 5.11.** Vorticity distribution over the FX61-163 airfoil panels at AoA 5 [deg] with Re = 1,5×10$^6$

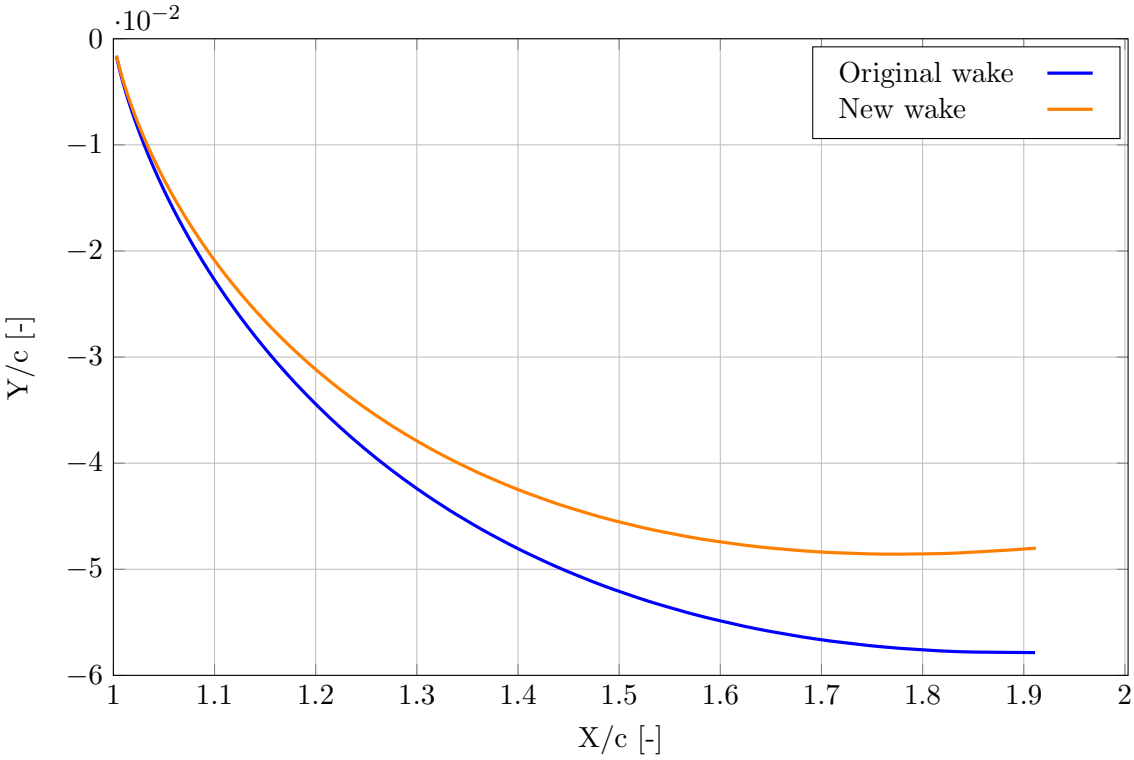


**Figure 5.12.** FX 61-163 updated wake trajectory at AoA 5 [deg] with Re = 1,5×$10^6$

## 5.3. FX66-S-196: Improved XFOIL predictions

The proposed improvement method seemed to be able to increase the inaccurate standard XFOIL predictions, as with the previous cases. For this airfoil the drag correction was able to improve the drag prediction with respect to the experimental measurements by an 18% increase. The improved method allowed for the shift of the offset values, showing that the results, as predicted by XFOIL, are in better agreement with the experimental results as seen in Fig. 5.13. From an observation of the data as predicted by the new method, a significant increase in the accuracy of the predicted drag, especially between $-5°$ and $8°$, is made, with respect to the experimental data. A small difference between the experimental data and the XFOIL improved method arise at $2°$ with the largest divergence from experimental data starting from $8°$. This steep incline of the drag is characterised by separated flow. Another factor that can influence this difference may be as a result of an inadequate capturing of the wake during experimental measurements as it is difficult to measure the wake at a high angle of attack with separation flow. Refer to the study by Fuglsang, Antoniou, and Sørensen (1998).

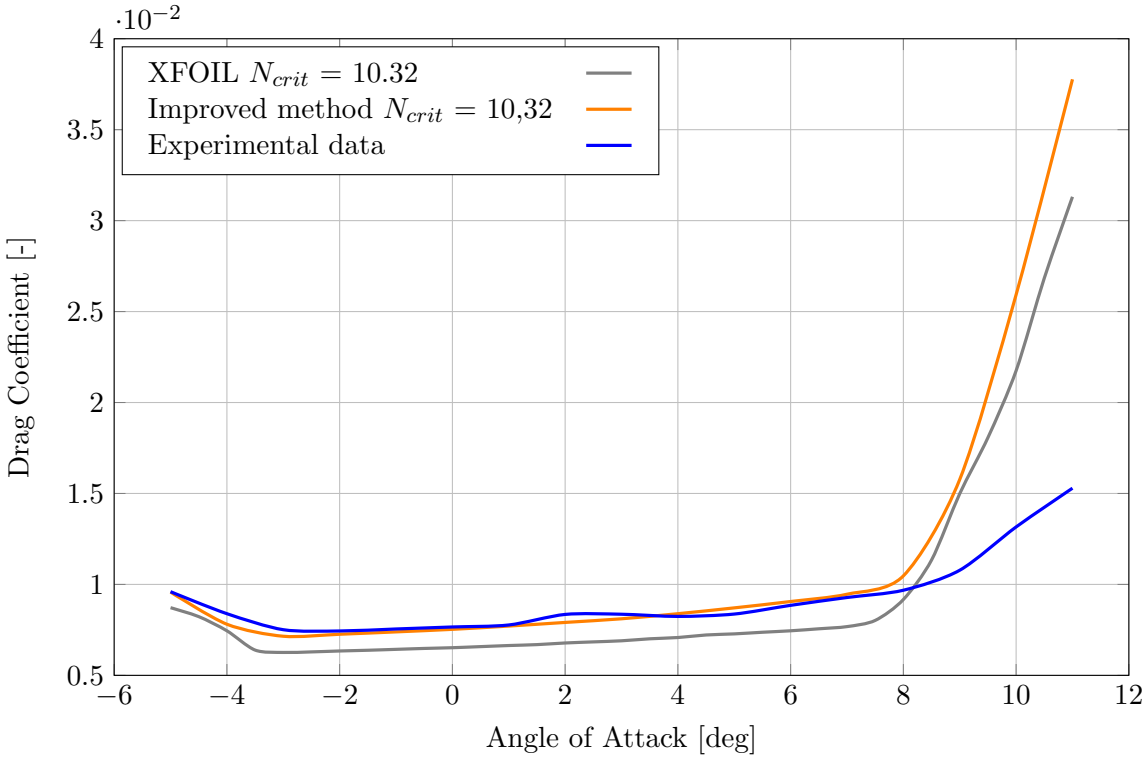


**Figure 5.13.** Improved drag predictions of the FX66-S-196 airfoil at Re = $2\times10^6$

Both the standard XFOIL and improved method, underpredict the lift coefficient from $-5°$ up to $5°$, as seen in Fig. 5.14, with the improved method underpredicting the maximum lift. An important observation can be made from the angle of attack of $8°$, which is the effect of the lift improvement. At this angle the improved XFOIL increased the value of the maximum predicted lift coefficient by 1%, resulting in an increase in the accuracy with better agreement with the experimental results.

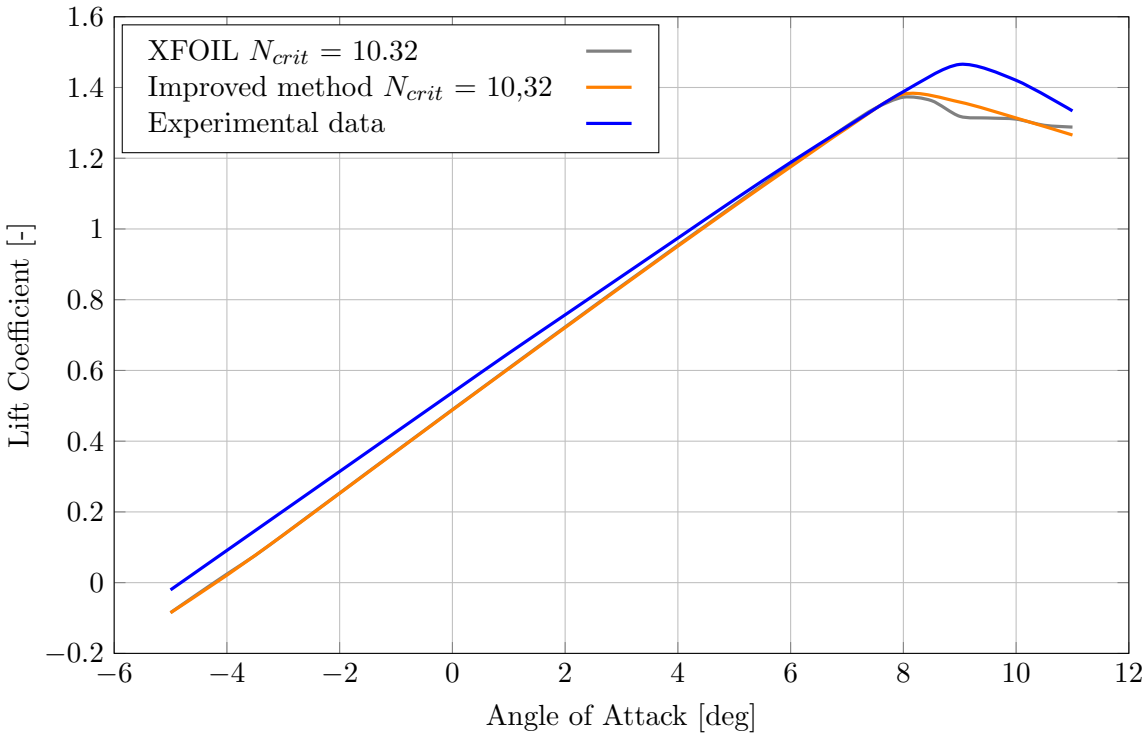


**Figure 5.14.** Improved FX66-S-196 lift predictions at Re = $2\times10^6$

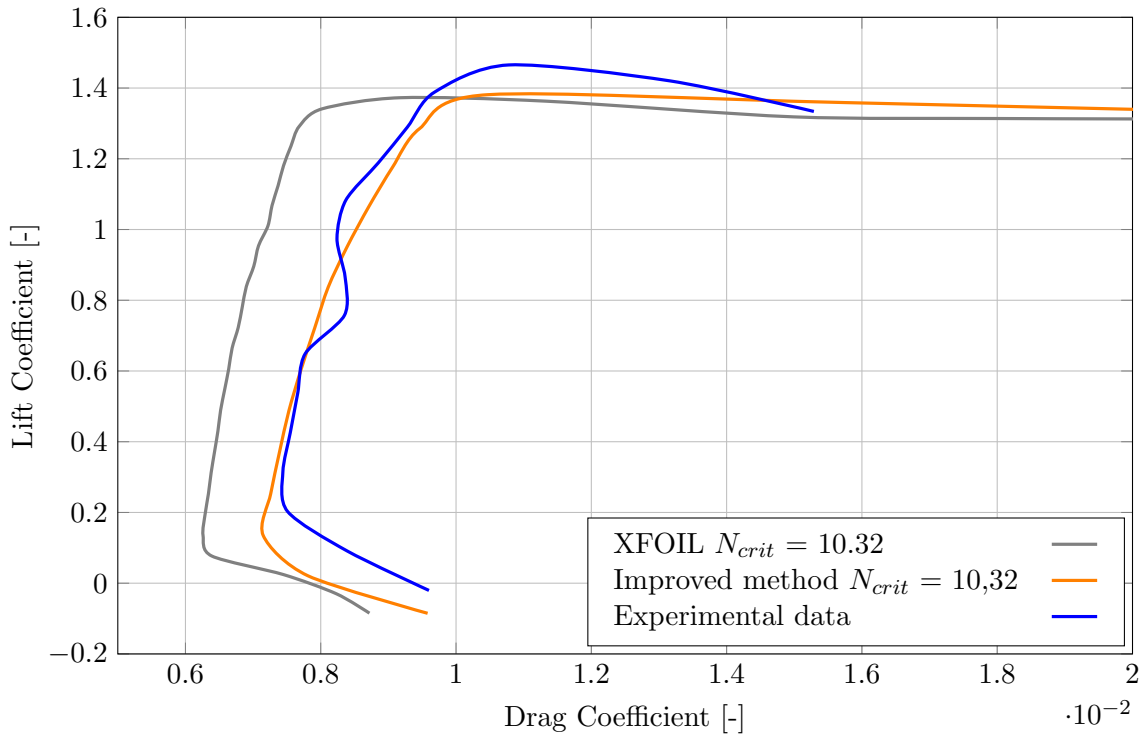


**Figure 5.15.** $C_l$ vs $C_d$ predictions of the FX66-S-196 airfoil at Re = $2\times10^6$

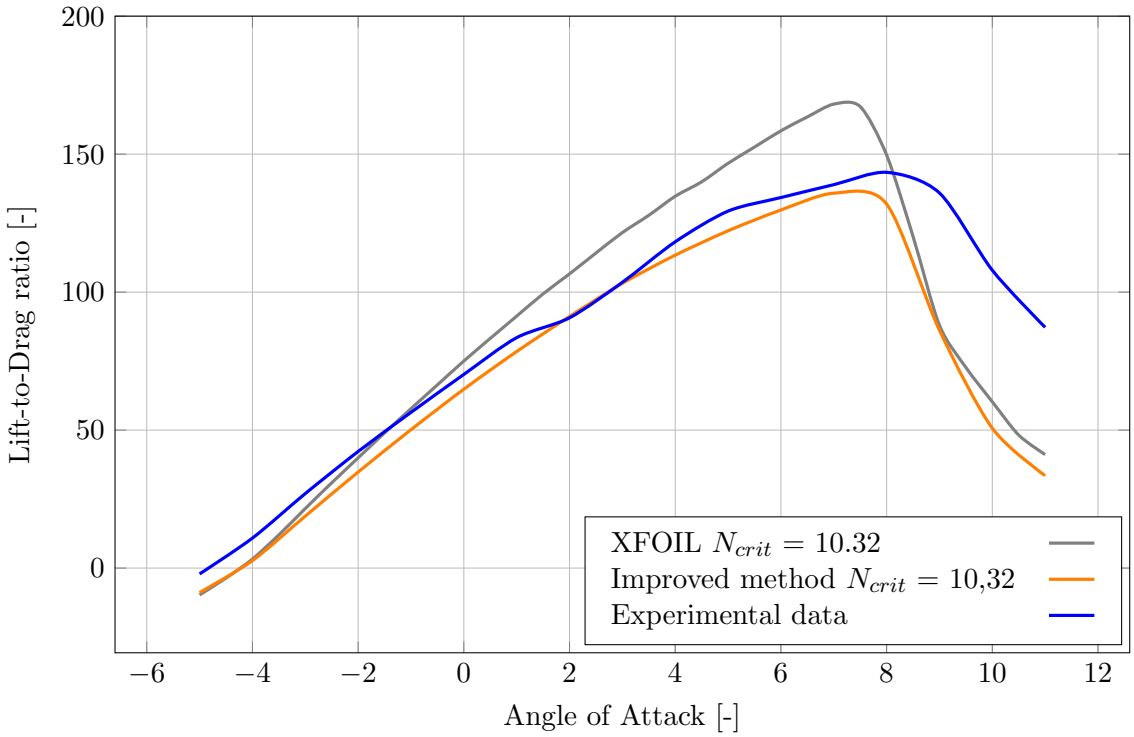


**Figure 5.16.** Lift-to-drag ratio vs angle of attack at Re = $2\times10^6$

When considering Fig. 5.15, it is clear that the improved XFOIL was better able to predict the lift and drag coefficients and the overall predictions are more in agreement with the experimental results with an 18% drag increase and 1% increase in maximum lift predictions. From Fig. 5.15 the improvement is clearly evident. The improved method was able to shift the predicted values in better agreement with the experimental data, with some inaccuracies arising at high and low angles of attack. The most accurate predictions were within the region from $-5°$ up to $7°$. This was due to the major contribution of an improved drag prediction method and the small contribution of the improved lift prediction method. Note from Fig. 5.16 and Fig. 5.14 that both the standard XFOIL and the improved XFOIL inaccurately predict the onset of stall, in comparison with the experimental data. The inception of stall conditions, according to the experimental data, is at $9°$, while the standard XFOIL and improved XFOIL stall conditions are reached at $8°$.

The result of the improved method is also visualised when considering the lift-to-drag ratio graph, in Fig. 5.16. Both the standard XFOIL and improved methods are less accurate at low angles of attack, when compared to the experimental results. But the improved method is more in agreement with the experimental data than the standard XFOIL predictions. At $-1°$, the standard method is able to better predict the lift-to-drag ratio than the improved XFOIL, and it is more in agreement with the experimental data at that angle. The maximum lift-to-drag ratio is much lower and has a tendency towards the experimental data, with the improved method. To match the wind tunnel quality results an amplification factor of 10.32 results in the predictions being in better agreement with the experimental results. Both the predicted value of the standard XFOIL and improved XFOIL decay from $7°$, with an underprediction of the lift-to-drag ratios from $8°$.

Once again it is clear that the improvement lift prediction method updates the vorticity strength and delivers greater vorticity strengths than the original XFOIL vorticity strength distribution. This correction is visualised in Fig. 5.17. The increase in the vorticity distribution affects the wake trajectory by changing the stream function, illustrated in Fig. 5.18. A clear reduced

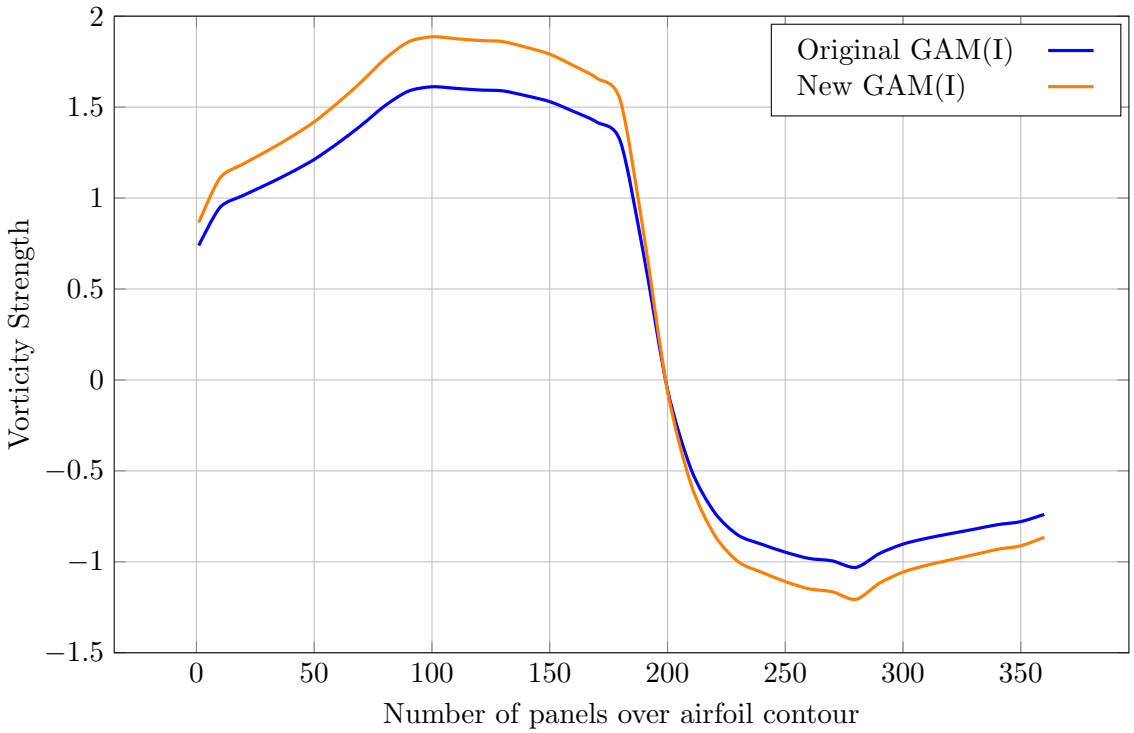


**Figure 5.17.** FX66-S-196 vorticity distribution update at AoA 5 [deg] with Re = 1,5×10$^6$

downwash of the wake trajectory is visible, reducing the maximum lift predictions.

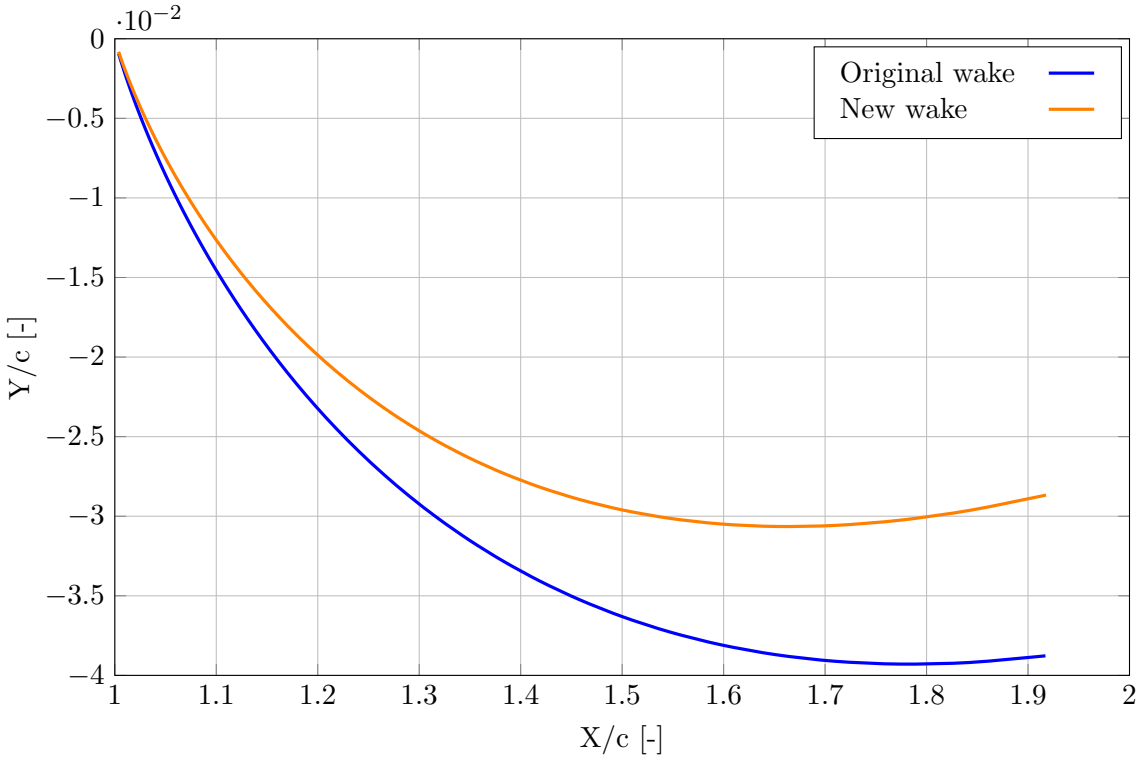


**Figure 5.18.** FX66-S-196 updated wake at AoA 5 [deg] with Re = 1,5×$10^6$

## 5.4. E603: Improved XFOIL predictions

Once again, the improved method proves to be superior to the standard XFOIL predictions and is more in agreement with the experimental measurements. The results of the improved drag correction are shown in Fig. 5.19. From first observation, it is clear that the improved method was able to increase the drag predictions by 16%, resulting in an overprediction of the drag, Although the drag is being overpredicted, the improved predictions are more in agreement with the experimental data, resulting in values that lie closer to the experimental data. At higher angles of attack standard XFOIL and the improved XFOIL both diverge from the experimental results, with the standard XFOIL at first underpredicting and then overpredicting the drag from 9.5°. The improved method overpredicts the drag in the same region.

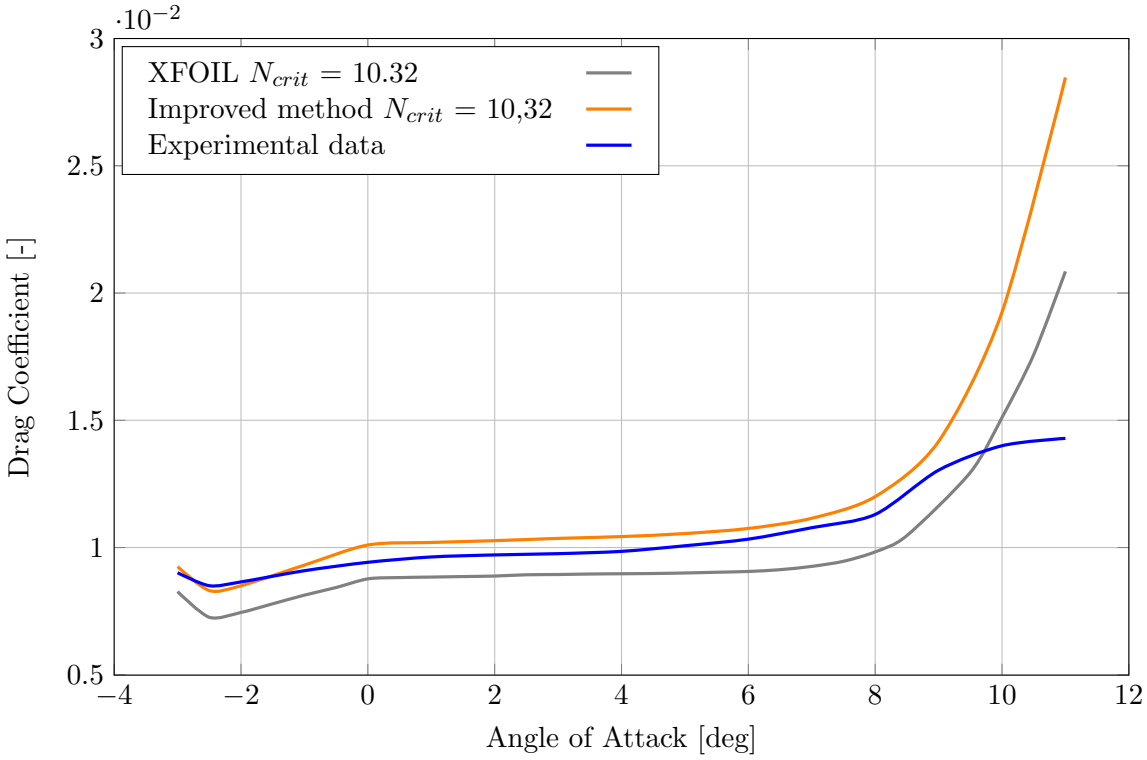


**Figure 5.19.** E603 airfoil improved drag prediction method at Re = $1\times10^6$

A considerable improvement to XFOIL maximum lift predictions is observed from Fig. 5.20. The improvement to the lift predictions causes a reduction of 6.5% in the maximum lift prediction. It is important to note that no observable improvement to the lift prediction is seen in the linear lift region. The linear lift region is overpredicted by both methods, with the exception of the prediction of the maximum lift. These methods also predict the inception of stall at an earlier stage (at 8.5° rather than at 10° as predicted by the original XFOIL) than the experimental results. This does not coincide with the experimental results as the same tendency was noticed as with the original XFOIL predictions, although the absolute lift values differ.

When considering the lift-to-drag ratio against the range of angles of attack, Fig. 5.22, the overprediction of the lift and drag results is clear. The improved method delivers results in better agreement with the experimental measurements, but still overpredicts the airfoil performance. It is observed in Fig. 5.22 that both the standard XFOIL and the improved method diverge from the experimental data at 9° and onwards. Maximum airfoil performance is predicted at 8° in all three cases, with the standard XFOIL predictions overpredicting the magnitude of the lift-to-drag ratios.

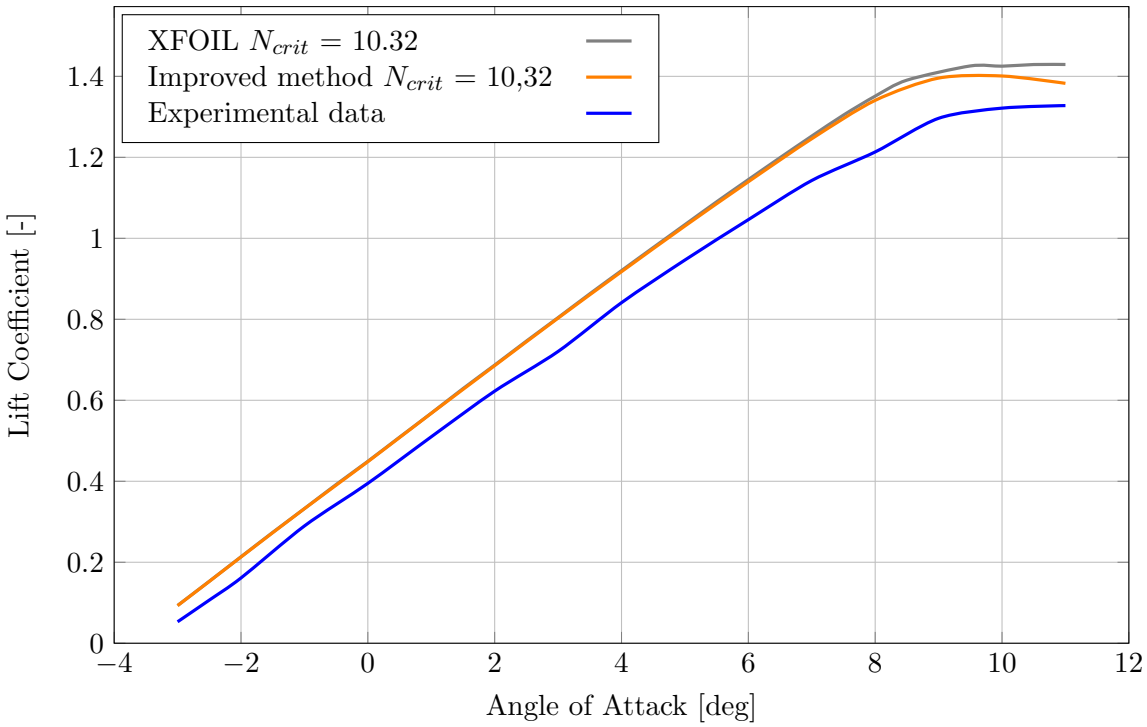


**Figure 5.20.** E603 airfoil improved lift prediction method at Re = $1{\times}10^6$

A correction in the wake trajectory is noticed as it is witnessed that an increase in the vorticity distribution results in reduced maximum lift predictions. Also, the wake has been updated to the expected reduced downwash of the wake trajectory to allow for the inclusion of the viscous wake. This has been illustrated in Fig. 5.23 and Fig. 5.24.

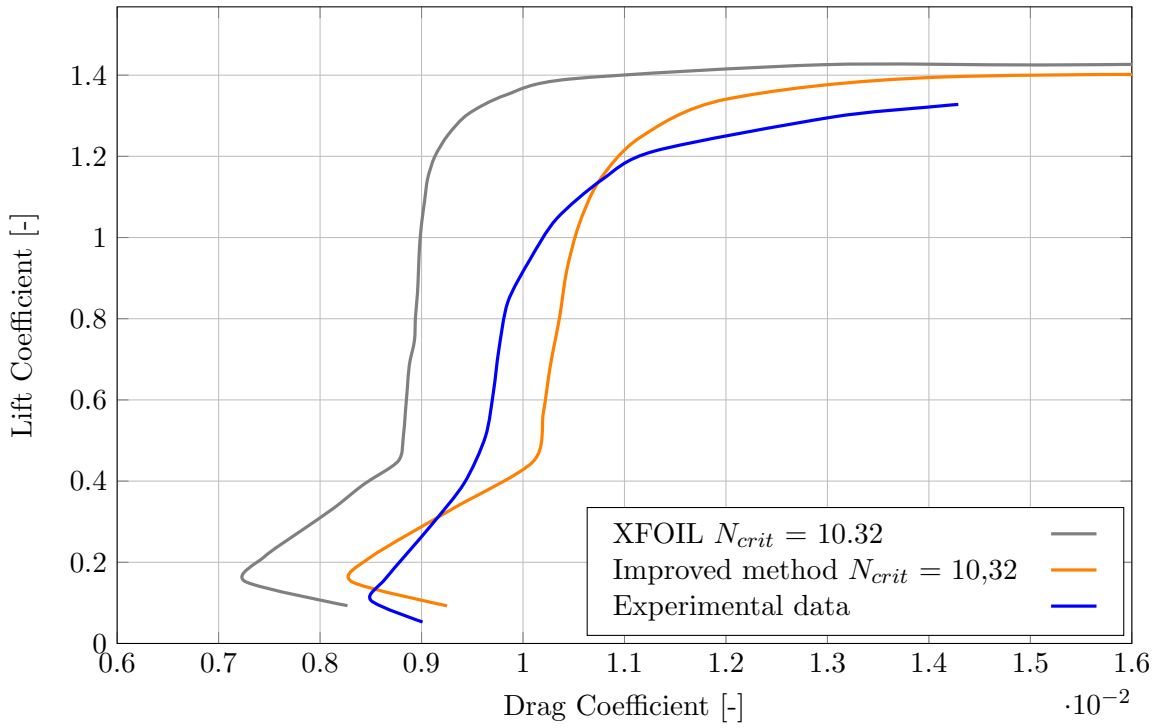


**Figure 5.21.** Improved $C_l$ vs $C_d$ of the E603 airfoil at Re = $1{\times}10^6$

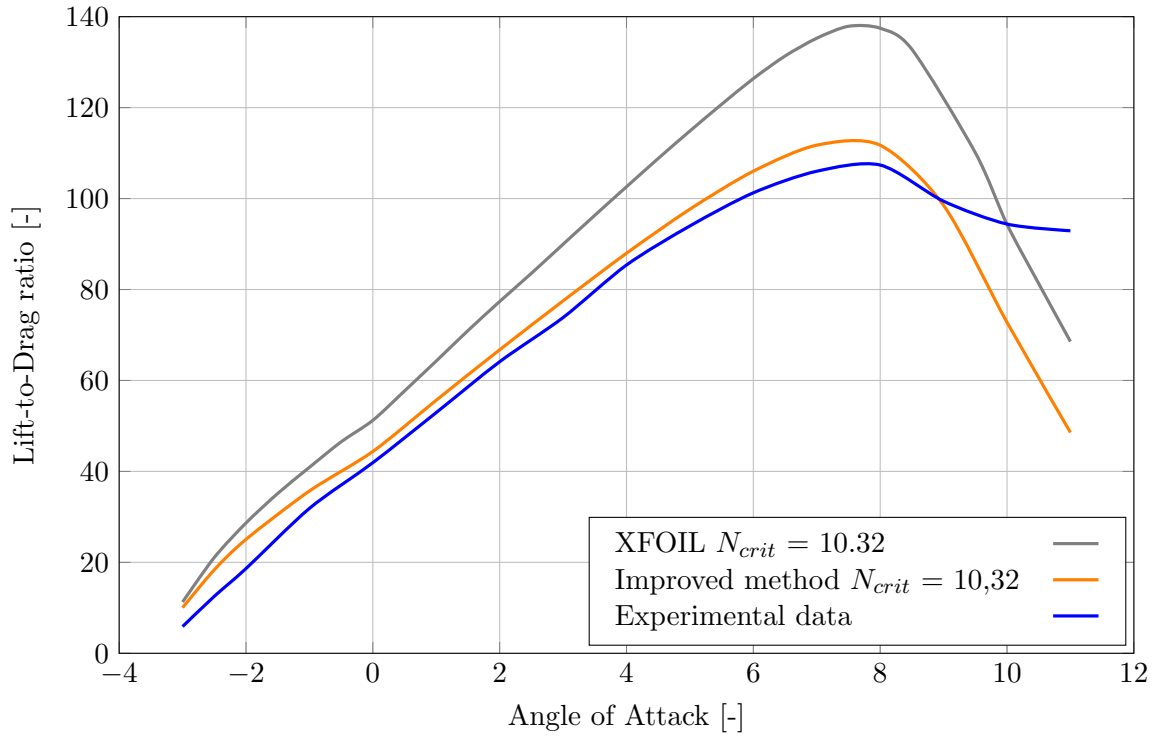


**Figure 5.22.** E603 lift-to-drag vs angle of attack at Re = $1{\times}10^6$

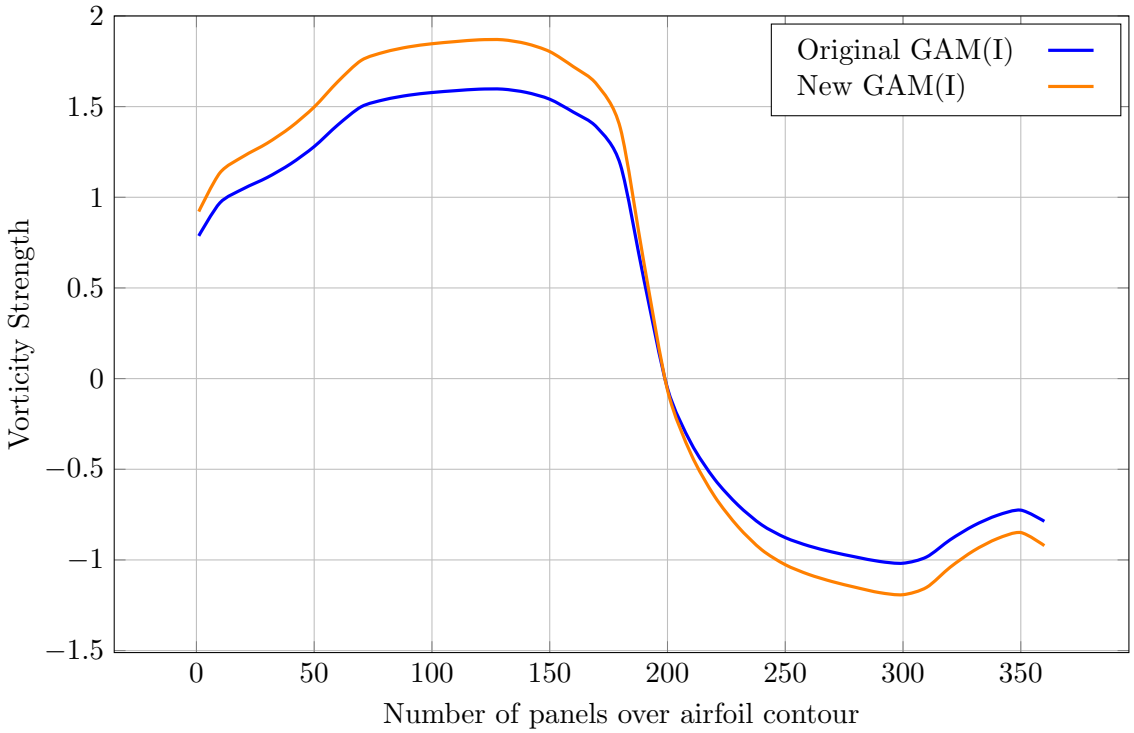


**Figure 5.23.** E603 updated vorticity distribution at AoA 5 [deg] with Re = $1\times10^6$

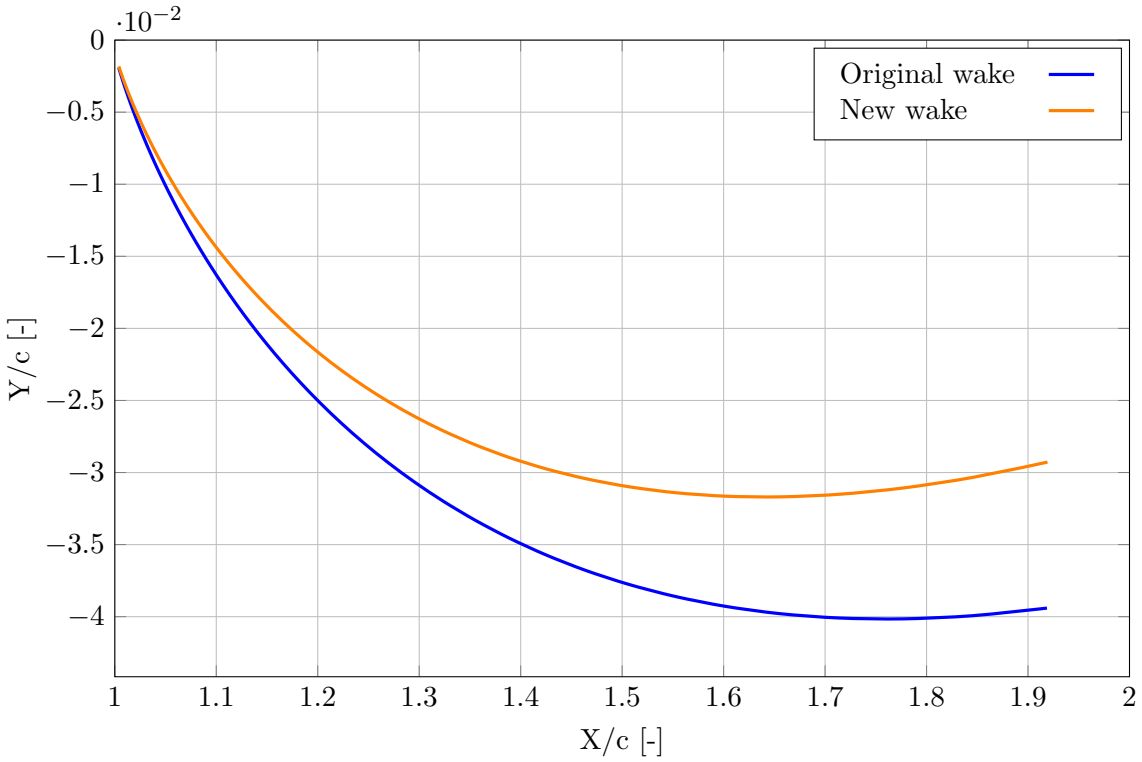


**Figure 5.24.** E603 updated wake trajectory at AoA 5 [deg] with Re = $1\times10^6$

## 5.5. Complementary study case

This study case was included in this report as it clearly shows an impressive improvement to the prediction of lift by the new method. The airfoil under investigation is the HPH yn1 type, manufactured by the HPH company (Pátek, Cervinka, and Vrchota, 2012). This airfoil finds its application in the sailplane industry. Wind tunnel tests were done on this airfoil at a Reynolds number of $1{,}5\times10^6$ and at an AoA range from $-6°$ up to $2°$. No indication of the wind tunnel turbulent intensity was given and it was thus decided to set the amplification factor to a value of 9, to meet standard XFOIL practice. This means the data is limited to the account of the wind tunnel turbulent intensity. The number of panels, generated over the airfoil contour, was set to 360 panels, to better capture the overall shape of the airfoil to allow XFOIL to be able to give reliable predictions. It will become clear that this value allows for accurate drag predictions in respect of the experimental data.

The improvement made to the XFOIL lift predictions is quite clear, when considering Fig. 5.25. The standard XFOIL program overpredicts lift from $-3°$. This overprediction of lift is observed up to stall conditions. The improved XFOIL program shows no significant change in lift predictions in the linear lift region and predicts the same values as the standard XFOIL predictions, diverging from the standard XFOIL predictions at $6°$. The most significant improvement is to maximum lift predictions, where the maximum lift value decreases by 3%, in better agreement with the experimental data, though lift in the stall region is overpredicted.

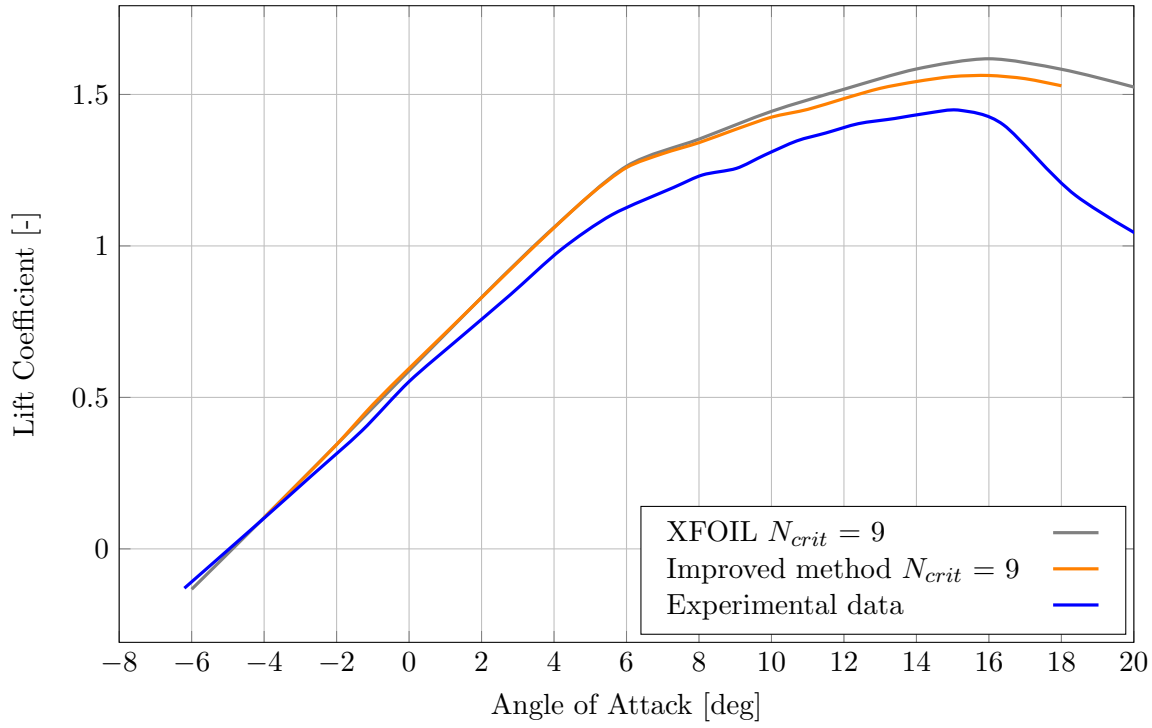


**Figure 5.25.** Improved lift predictions at Re = $1{,}5\times10^6$

Drag predictions of the standard XFOIL and the improved XFOIL are shown in comparison with experimental data in Fig. 5.26. In this study, XFOIL was already able to accurately predict the airfoil drag, according to the experimental data. A divergence from the experimental data is observed from $2°$, as is the common XFOIL issue. At lower angles of attack this is also noticed from $-4°$. The improved method shows overall better predictions that are more in agreement with the experimental data. An underprediction of drag is observed from $-2°$ up to $= 6°$ and at $13°$, where divergence from the experimental data is observed. This divergence from the experimental data at higher angles of attack, results in an underprediction of drag as

stall conditions are reached.

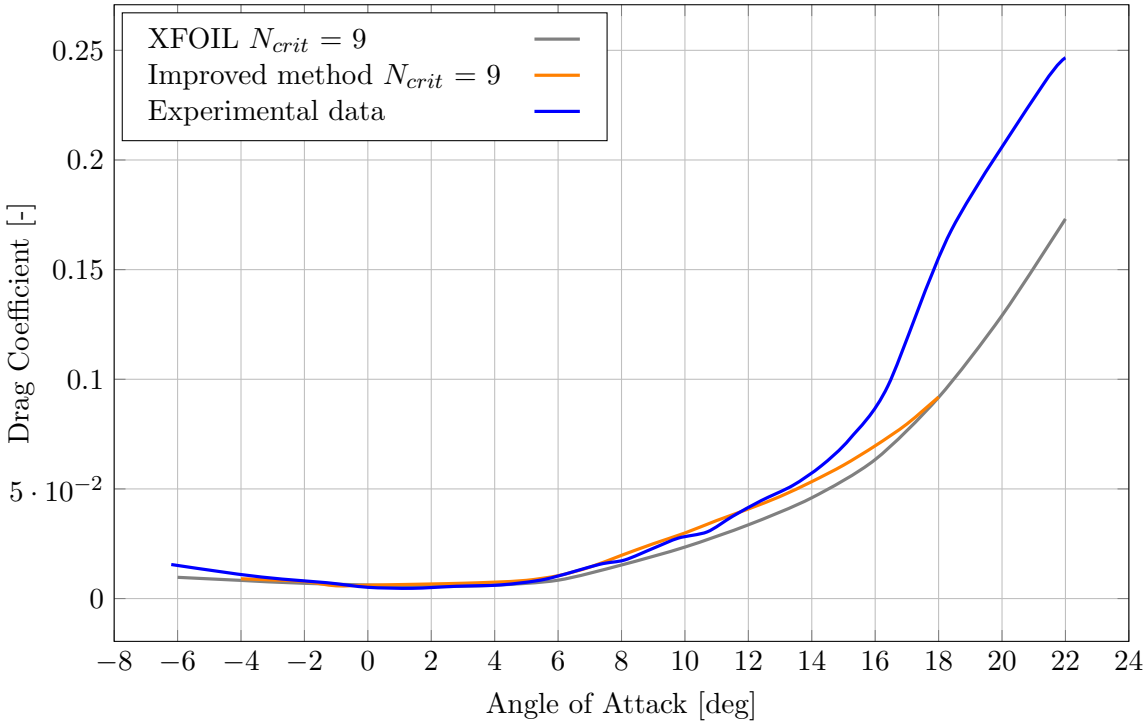


**Figure 5.26.** Improved drag predictions at Re = 1,5×10$^6$

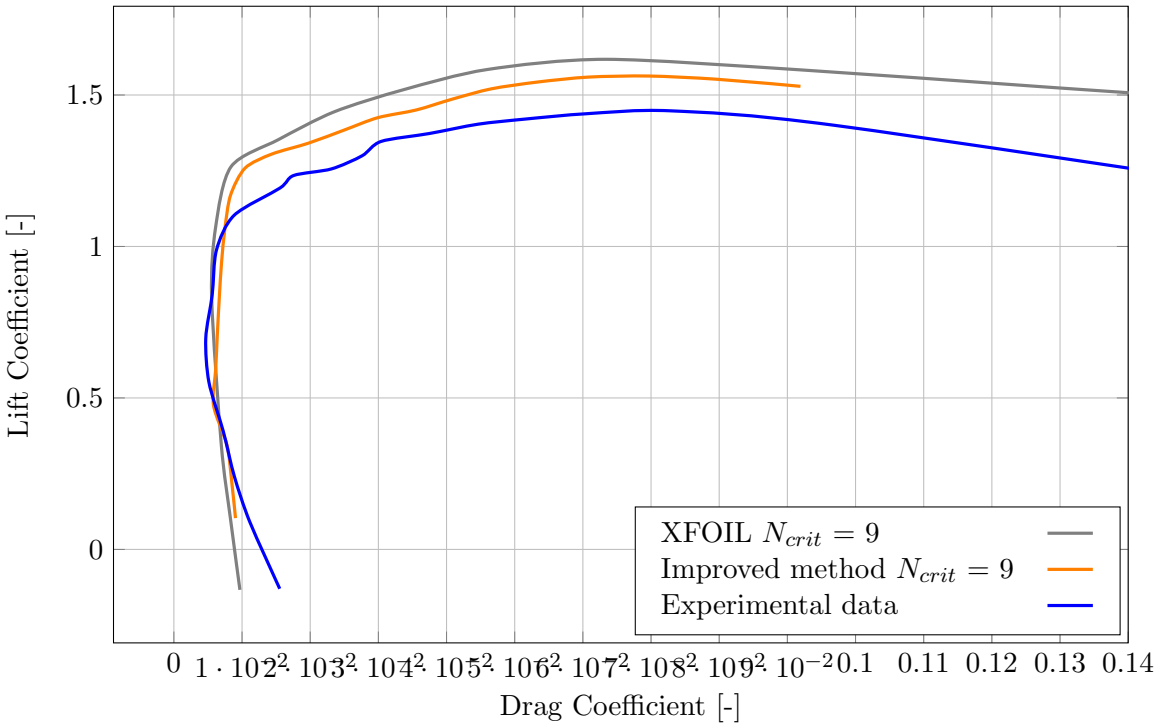


**Figure 5.27.** Improved $C_l$ vs $C_d$ prediction at Re = 1,5×10$^6$

When considering Fig. 5.28, an overall improvement to the lift and drag predictions is observed. Both the standard XFOIL and improved XFOIL overpredict the lift-to-drag ratio from −4° to 0°, with the improved method being in better agreement with the experimental results. An underprediction of the values is seen between 0° and 6° with XFOIL overprediction polars in this same region. The most significant improvement to the XFOIL lift-to-drag predictions is within the range of angles of attack from 6° up to near-stall conditions. The standard XFOIL overpredicts these values from 2° until stall condition is reached. Also, a divergence of the improved method from the experimental data is observed from 14° nearing stall conditions, which is characterised by a divergence form the linear lift region and it is clear from Fig. 5.25 that this is the case.

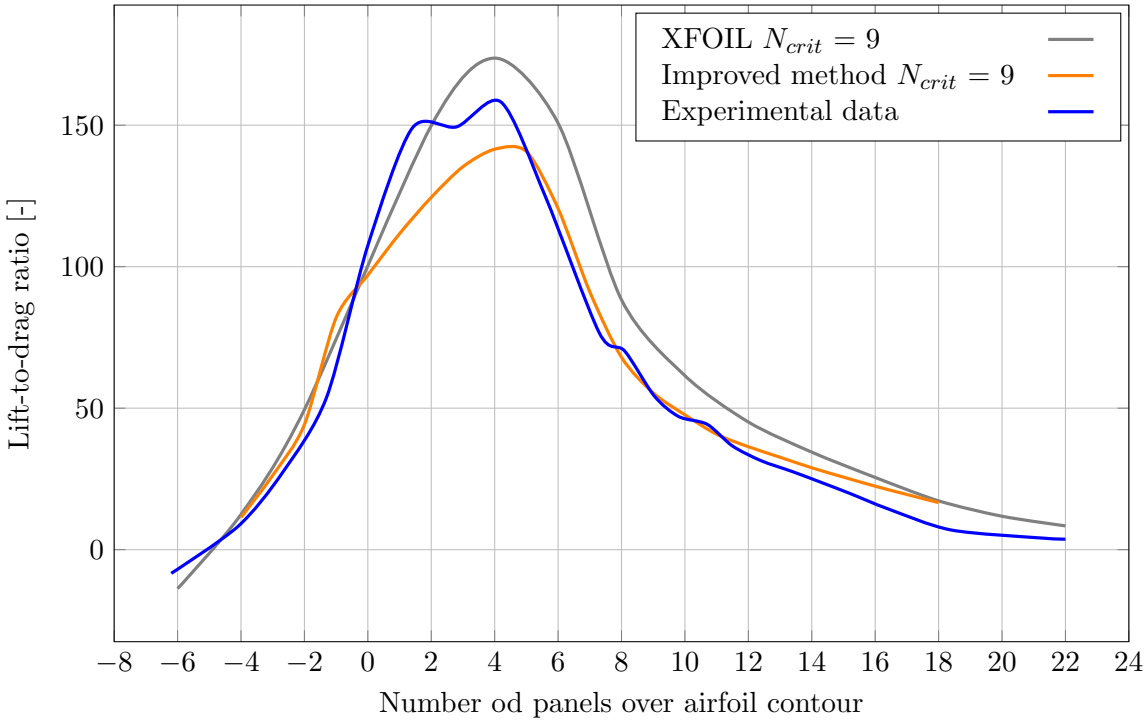


**Figure 5.28.** Improved Lift-to-Drag predictions at Re = 1,5×10$^6$

As mentioned previously, updating the vorticity distribution over the airfoil panels has a direct effect on XFOIL's lift predictions. This is evident from the study completed in this chapter. It can be shown that an increase in the magnitude of the vorticity strength distribution will lead to a decrease in the pressure coefficient prediction over the airfoil surface. Therefore, it was necessary to include a study to show this effect of the updated vorticity distribution. This airfoil was chosen the investigation showed the largest improvement to the lift predictions. At an AoA of 5°, there is no remarkable difference between the standard XFOIL lift predictions and the improved method. This means that no adverse differences in the pressure coefficient between the standard XFOIL and the improved XFOIL predictions is expected, as seen in Fig. 5.29. This figure also shows the reason for the inaccurate XFOIL lift prediction, as a higher pressure coefficient at the pressure side of the airfoil and a lower pressure on the suction side, are predicted. This can be attributed to the panel formulation used by XFOIL because the airfoil is broken up into small straight panels instead of curved panels, From Fig. 5.25 a difference between the improved method and the standard XFOIL prediction is noticed at an AoA of 8° and thus a difference in $C_p$ predictions of the two methods is expected. This can be shown in Fig. 5.30.

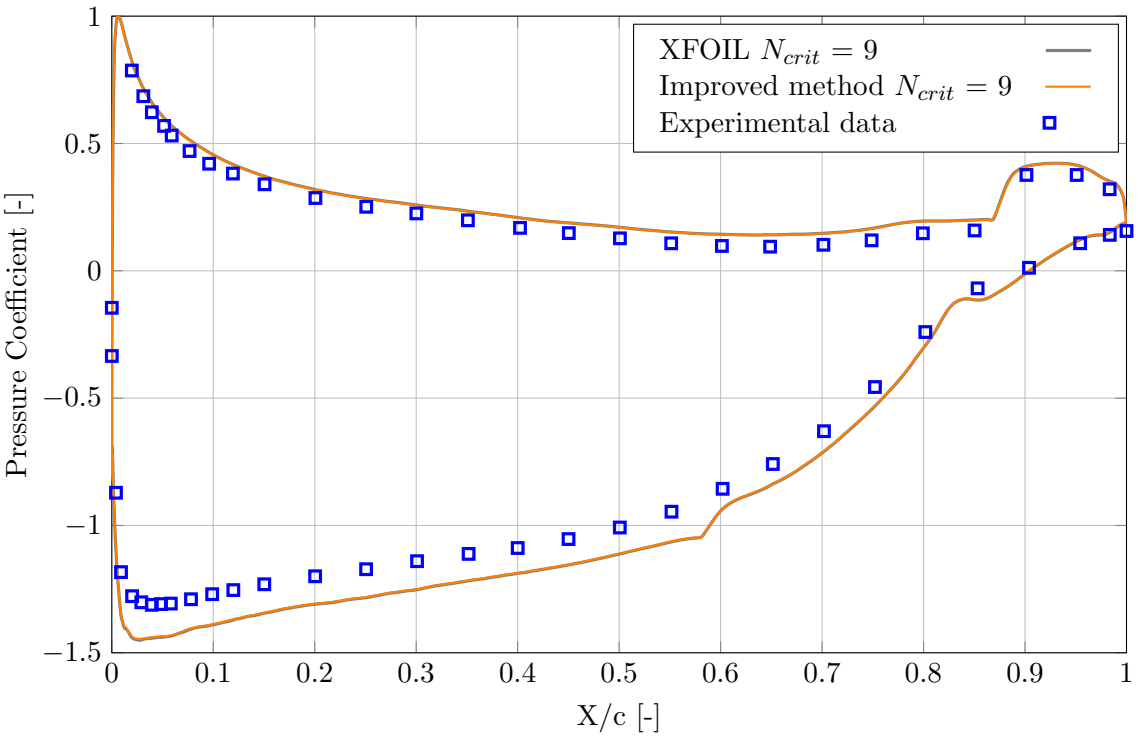


**Figure 5.29.** Updated $C_p$ distribution at AoA of 5° with Re = 1,5×10$^6$

Fig. 5.30 shows the difference in pressure coefficient prediction of the two methods. From this figure an improvement is shown as a reduced prediction of the pressure is visible on the pressure side of the airfoil. Also, on the suction side there are three things that can be noted. First, a reduction in the pressure predictions is most notable on the suction side, as the difference between the standard XFOIL predictions and the improved method at the leading edge differ the most significantly at this location. This is because a lower value of $c_p$ is obtained with the vorticity strength update method which explains what is found in the pressure side as well. For an inviscid analysis the value of $U_e$ is higher than the viscous $U_e$. By using the vorticity strength update method, a decrease in the $c_p$ distribution is obtained, indicating a reduction in the edge velocity that includes viscous effects. Secondly, the improved method predicts transition at a point further downstream than the standard XFOIL. The reason for this was introduced in the previous note on the suction side. A lower value of $U_e$ is obtained due to viscous effect having an influence on this value. This will cause a delay in the transition prediction method as the value of $U_e$ is lower and will thus cause transition at a position downstream in reference to the original predicted position. Thirdly, the improved method causes the pressure predictions at the trailing edge to become less accurate with reference to the standard XFOIL predictions and it overpredicts the pressure coefficient in this location. This is due to the overall decrease of the predicted $c_p$ value. The methods seem to decrease the value of $c_p$ that affects the predicted value in the trailing edge and causes this overprediction of $c_p$ in this region.

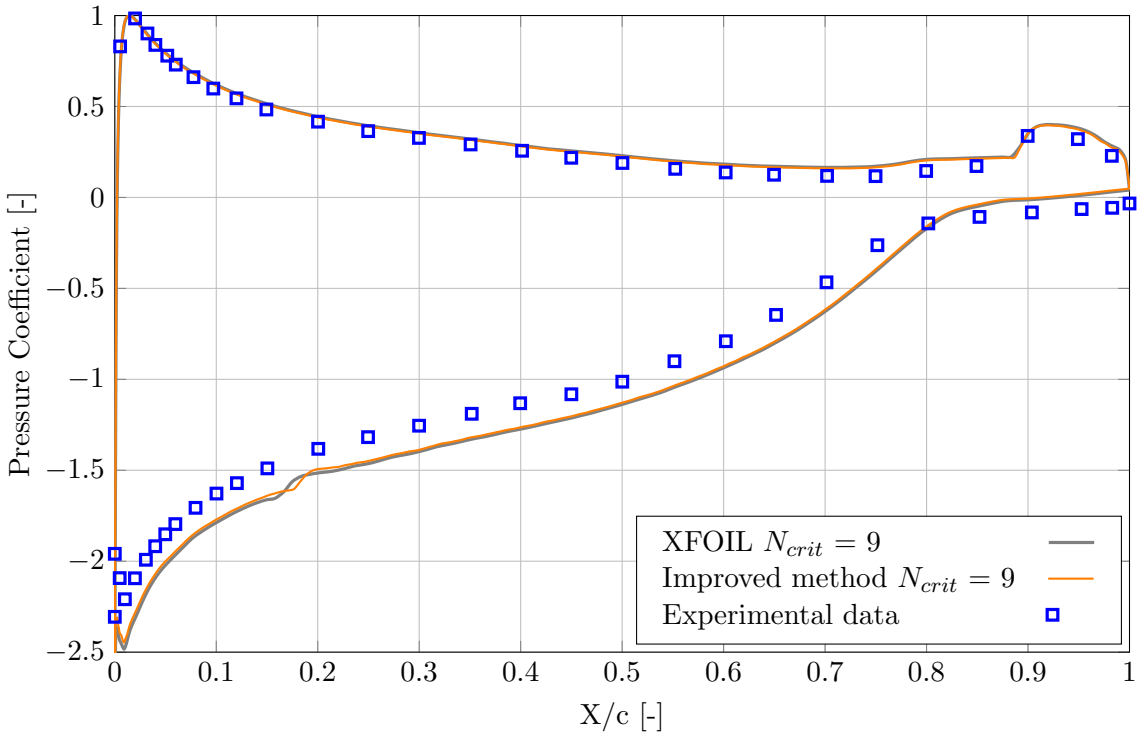


**Figure 5.30.** Improved $C_p$ distribution at AoA of 8° with Re = 1,5×10$^6$

## 5.6. Conclusion

### 5.6.1. Improved drag prediction conclusion

From the current study, it was found that XFOIL underpredicts drag because of the underpredictions of the integral boundary layer quantities. This was corrected by a study done by Ramanujam, Ozdemir, and Hoeijmakers (2016). The improvements were implemented to the standard XFOIL and the improvement in drag predictions was significant, ranging from 11% to 18%. The improved method was used to analyse the performance of four different airfoils, ranging from wind turbine to sailplane applications. The improved drag method has been shown to give results in better agreement with experimental data that was obtained from the literature. When considering the improvement against the standard XFOIL predictions, the improvement is quite clear. Over all four test cases, an improvement to the predictions of drag was observed. At very high angles of attack The improved methods, like the standard XFOIL predictions, diverge from the specific airfoil experimental data. This was observed in all cases that were studied. The same cannot be said in lower angles of attack. The only case where an adverse divergence from experimental data was observed was in the NACA $63_3 - 418$ case where absolute divergence at an angle of attack lower than $-10°$ was noticed. The FX61-163 study case significantly (up to 18%) improved the drag predictions and the results lie in excellent agreement with the experimental measurements. The complementary study case shows clearly that the improved method allows for more accurate maximum lift predictions, though still overpredicting lift. Nevertheless, the results are in better agreement with the experimental results.

The changes that were made to XFOIL enabled drag predictions that are in better agreement with the experimental results. This was observed where no significant flow separation was observed. At high and low angles of attack divergence from the data was noticed and this can be attributed to the separated flow that originates in those regions, This is due to the collapse of the Kutta condition at the trailing edge. The improved drag method does not cause an increase in calculation time, as variables used in the original XFOIL programming are used and corrected in a formula. Through the study cases, as mentioned previously, this proposed improvement method works excellently within the post-stall region.

### 5.6.2. Improved lift prediction conclusion

The lift improved method was a more complicated problem as the lift calculations can mostly be altered with the vorticity strength calculations. It can be seen in the relevant figures that to improve upon XFOIL lift predictions, an increase the vorticity distribution over the airfoil results in lower $c_p$ values. This influences the lift calculations by reducing the maximum predicted lift. This was achieved by allowing the edge velocity distribution to update the vorticity strengths to model the effects of the viscous edge velocity. The result of this is a reduced downwash of the wake at the trailing edge. With a vorticity distribution that is greater in magnitude, results in a lower pressure coefficient prediction, which results in a lower lift prediction. This improved method resulted in a lower maximum lift prediction when compared to the standard XFOIL predictions and tended to the experimental data. In all cases, a reduction in the predicted maximum lift was observed with lower post-stall predictions, tending towards the experimental data. This is clear when considering the lift coefficient graph of the HPH airfoil. Slight changes in the linear lift region were noticed, but the most significant improvement is in the maximum lift prediction where the improved method triumphed over the standard XFOIL calculations.

Within the stall region the improvement method also predicted much lower values and were in better agreement with the experimental results. In the FX66-S-196 case study, an interesting development occurred; both the standard XFOIL and the improved method underpredict the

lift of this airfoil. The improved method reduced the maximum lift predictions but caused an overall underprediction of the lift.

In the FX66-S-196 case, an increase in the maximum lift was observed, that is in better agreement with the experimental data. A persistent problem with the lift predictions is the prediction of the onset of stall, due to the Goldstein singularity. This requires further investigation as panel formulation discrepancies arise (Ramanujam and Ozdemir, 2017). Although the improved method reduced the maximum predicted lift, in some cases the improved method was not able to capture the onset of stall in agreement with the experimental results.

# 6. Chapter 6: Conclusion and recommendations

## 6.1. Conclusion

At the commencement of this study, a problem was given to improve upon XFOIL's lift and drag predictions. The necessary research has been completed and improvements to lift and drag predictions of vortex panel methods were identified. These improvements were implemented into XFOIL through a VirtualBox to enable editing of the XFOIL source code in a Linux OS environment. The standard XFOIL program was then used to calibrate the flow analysis to allow for accurate predictions of the airfoil performance. The inaccuracy of XFOIL was studied and documented in this report. It was clear that XFOIL underpredicts drag and has an overall tendency to overpredict lift and overpredict the onset of stall. Through the literature study it was realised how lift is predicted from panel methods and this knowledge was utilised to improve upon XFOIL lift predictions. The study done by Ramanujam and Ozdemir (2017) showed promise and the improvements were implemented to XFOIL. By first observation the new method improved upon the maximum lift prediction.

The methods researched by Ramanujam and Ozdemir (2017) and Ramanujam, Ozdemir, and Hoeijmakers (2016) were developed to allow for XFOIL predictions to produce values that took into account the effect of viscous flow and updated the wake trajectory, which were required to perform viscous calculations. The corrected momentum thickness, at the trailing edge was also taken into account. The drag method was mathematically formulated to allow for the prediction of the momentum thickness by using the actual definition of momentum thickness at a point (c=1) in the wake. Equivalent tendencies in the drag prediction between the improved method and XFOIL, were observed, with a shift of the absolute drag value towards the experimental data. This may be a good indication of actual flight performance as the same tendencies are observed but the new method was able to produce predictions that are in agreement with the experimental results, which may be closer to actual flight performance properties.

If the lift-to-drag versus the angle of attack graphs of each study case are considered, an increase in accuracy is observed at each angle. The observation shows that the improved XFOIL is better at predicting both the lift and drag in agreement with the experimental data. This improvement is greatly influenced by the corrected drag predictions. In addition, an improvement to the pressure distribution over the airfoil was observed and documented,

From the lift versus drag coefficient graphs the improvements are also clear and show that the improved XFOIL is better at predicting lift and drag in regions with no flow separation over the airfoil. The improved drag method become negative in stall regions where the predicted value of the velocity at the edge of the boundary layer exceeds the magnitude of the free stream, as found by Ramanujam, Ozdemir, and Hoeijmakers (2016). Also, the proposed correction improves the prediction of lift for airfoils with a low trailing edge thickness. This has also been documented by Ramanujam and Ozdemir (2017). As evident from this study and the study done by Ramanujam and Ozdemir (2017), the formulation of the trailing edge panels is identified as the cause of the overprediction of lift in XFOIL.

## 6.2. Recommendations

### 6.2.1. Improved XFOIL recommendations

As mentioned, this improved XFOIL produces predictions that are in better agreement for airfoils with a low trailing edge height ($h_{TE} < 3\%$). Also, the improved lift and drag predictions are in better agreement at regions between the onset of stall conditions. Keep in mind that if the distance from the trailing edge is increased, a recalibration of the drag correction is required as the value of $H_1$ becomes very large as the value of $H$ is close to unity, as recorded by Ramanujam, Ozdemir, and Hoeijmakers (2016).

### 6.2.2. Critical amplification ratio improvement

A study done by Bongers (2006), showed that the XFOIL version of predicting transition was only able to predict very limited damping of the amplification factor. Schlicting and Tollmien developed the idea of the linear stability theory. In some cases the developers saw that some disturbances in the boundary layer are able to be damped out within the boundary layer. Also, to reduce drag over an airfoil requires that the transition of the boundary layer be delayed. This has been achieved by means of boundary layer suction.

This is the case when considering sailplane airfoils where suction is used to reduce the drag. This method uses a forced transition to remedy the fact that convergence was not reached. The major advantage is that this so-called 'improved' $e^{N_{crit}}$ was able to account for the damping of disturbances within the boundary layer that postpone transition.

### 6.2.3. Double-wake method in XFOIL

According to Vaithiyanathasamy et al. (2018), the single-wake concept leads to inefficiencies in predictions for separated flows and stalled flows. To remedy this, the authors introduced the concept of a double-wake model formulation in an interactive boundary layer method. This concept models the pressure distribution in the separated region as a result of convected vorticity due to flow separation (Vaithiyanathasamy et al., 2018). With the implementation of this model, the authors were able to improve upon the lift predictions even further with panel methods like XFOIL and RFOIL.

# Bibliography


Abbott, A and Von Doenhoff A.H. (1959). *Theory of wing sections, including a summary of airfoil data*. New York : Dover Publications,

Althaus, Dieter (1996). "Niedriggeschwindigkeitsprofile :Profilentwicklungen und Polarenmessungen im Laminarwindkanal des Instituts für Aerodynamik und Gasdynamik der Universität Stuttgart/ Dieter Althaus". In:

Anderson, J.D. (2016). *Fundamentals of Aerodynamics*. McGraw-Hill Education. ISBN: 9781259129919. URL: https://books.google.co.za/books?id=D1ZojgEACAAJ.

Blasius, Heinrich (1907). *Grenzschichten in Flussigkeiten mit kleiner Reibung*. Druck von BG Teubner.

Bongers, J. (Aug. 2006). "Implementation of a new transition prediction method in xfoil: Predicting transition in suction boundary layers". In: URL: http://resolver.tudelft.nl/uuid:f04b7f3e-7df6-4132-9037-50b48b431523.

Coder, James and Mark Maughmer (Jan. 2013). "Numerical Validation of the Squire-Young Formula for Profile Drag Prediction". In: vol. 52. ISBN: 978-1-62410-181-6. DOI: 10.2514/6.2013-966.

DAVARI, Ali R. (2017). "Wake structure and similar behavior of wake profiles downstream of a plunging airfoil". In: *Chinese Journal of Aeronautics* 30.4, pp. 1281–1293. ISSN: 1000-9361. DOI: https://doi.org/10.1016/j.cja.2017.05.007. URL: https://www.sciencedirect.com/science/article/pii/S1000936117301127.

De Oliveira Andrade, Gael et al. (June 2018). "Improved airfoil polar predictions with data-driven boundary-layer closure relations". In: *Journal of Physics: Conference Series* 1037, p. 022009. DOI: 10.1088/1742-6596/1037/2/022009.

De Tavernier, Delphine, Daniel Baldacchino, and Carlos Ferreira (May 2018). "An integral boundary layer engineering model for vortex generators implemented in XFOIL". In: *Wind Energy* 21. DOI: 10.1002/we.2204.

Drela, Mark (June 1989). "XFOIL: An Analysis and Design System for Low Reynolds Number Airfoils". In: vol. 54. ISBN: 978-3-540-51884-6. DOI: 10.1007/978-3-642-84010-4_1.

Drela, Mark and Michael Giles (Oct. 1987). "Viscous-Inviscid Analysis of Transonic and Low Reynolds Number Airfoils". In: *Aiaa Journal - AIAA J* 25, pp. 1347–1355. DOI: 10.2514/3.9789.

Eppler, R. (2003a). "About classical problems of airfoil drag". In: *Aerospace Science and Technology* 7.4, pp. 289–297. ISSN: 1270-9638. DOI: https://doi.org/10.1016/S1270-9638(03)00029-4. URL: https://www.sciencedirect.com/science/article/pii/S1270963803000294.

– (2003b). "About classical problems of airfoil drag". In: *Aerospace Science and Technology* 7.4, pp. 289–297. ISSN: 1270-9638. DOI: https://doi.org/10.1016/S1270-9638(03)00029-4. URL: https://www.sciencedirect.com/science/article/pii/S1270963803000294.

Fuglsang, Peter, Ioannis Antoniou, and Niels Sørensen (Jan. 1998). "Validation of a Wind Tunnel Testing Facility for Blade Surface Pressure Measurements". In: *Electronic Networking: Research, Applications and Policy - EN*.

Fuglsang, Peter and Stefano Bove (Jan. 2008). "Wind Tunnel Testing Of Airfoils Involves More Than Just Wall Corrections". In:

Ghadimi, Parviz, Ali Bakhshandeh Rostami, and Farzad Jafarkazemi (2012). "Aerodynamic analysis of the boundary layer region of symmetric airfoils at ground proximity". In: *Aerospace*

*Science and Technology* 17.1, pp. 7–20. ISSN: 1270-9638. DOI: https://doi.org/10.1016/j.ast.2011.02.008. URL: https://www.sciencedirect.com/science/article/pii/S1270963811000435.

Gooden, J. (1979). "EXPERIMENTAL LOW-SPEED AERODYNAMIC CHARACTERISTICS OF THE WORTMANN FX 66-S-196 V1 AIRFOIL". In: *Technical Soaring An International Journal* 5, pp. 21–31.

Ingram, Taylor Geoffrey (Aug. 1936). "Statistical theory of turbulence V-Effect of turbulence on boundary layer theoretical discussion of relationship between scale of turbulence and critical resistance of spheres". In: *Proceedings of the Royal Society of London. Series A, Mathematical and Physical Sciences* 156, pp. 307–317. DOI: 10.1098/rspa.1936.0149.

Katz, Joseph and Allen Plotkin (2001). "The Laminar Boundary Layer". In: *Low-Speed Aerodynamics*. 2nd ed. Cambridge Aerospace Series. Cambridge University Press, pp. 448–482. DOI: 10.1017/CBO9780511810329.016.

Lamport, Leslie (1994). *LaTeX: A Document Preparation System (2nd Edition)*. 2nd. Addison Wesley. 288 pp. ISBN: 0-201-52983-1.

Lasauskas, Eduardas and Laurynas Naujokaitis (Mar. 2009). "Analysis of three wing sections". In: *Aviation* 13, pp. 3–10. DOI: 10.3846/1648-7788.2009.13.3-10.

Le Roux, Vincent and Johannes Jacobus Bosman (2019). *CFD airfoil profile drag calculation using far-field wake analysis.* URL: https://nwulib.nwu.ac.za/login?url=https://search.ebscohost.com/login.aspx?direct=true&db=cat01185a&AN=nwu.b2328904&site=eds-live.

Loek Boermans, H. Selen (Sept. 1981). "On the design of some airfoils for sailplane application". In: *Technical Soaring An International Journal* 7, pp. 13–35.

Miley, S J (Feb. 1982). "Catalog of low-Reynolds-number airfoil data for wind-turbine applications". In: DOI: 10.2172/5044823. URL: https://www.osti.gov/biblio/5044823.

Ozdemir, Huseyin et al. (Jan. 2017). "Unsteady Interacting Boundary Layer Method". In: DOI: 10.2514/6.2017-2003.

Pátek, Z., Cervinka, and Petr Vrchota (Sept. 2012). "WIND TUNNEL AND CFD STUDY OF AIRFOIL WITH AIRBRAKE". In:

Purevsuren, Enkhdavaa (May 2018). "Aerodynamic CFD study of Wortmann FX66-S-196 Airfoil". In: *International Journal of Engineering Research and* V7. DOI: 10.17577/IJERTV7IS040380.

Ramanujam, Giridhar and Huseyin Ozdemir (Jan. 2017). "Improving Airfoil Lift Prediction". In: DOI: 10.2514/6.2017-1999.

Ramanujam, Giridhar, Huseyin Ozdemir, and H. Hoeijmakers (Jan. 2016). "Improving Airfoil Drag Prediction". In: DOI: 10.2514/6.2016-0748.

Reid, Michael and Jeffrey Kozak (Aug. 2006). "Thin/Cambered/Reflexed Airfoil Development for Micro Air Vehicle Applications at Reynolds Numbers of 60,000 to 100,000". In: vol. 2. ISBN: 978-1-62410-045-1. DOI: 10.2514/6.2006-6832.

Schlichting, H. et al. (2003). *Boundary-Layer Theory*. Physic and astronomy. Springer Berlin Heidelberg. ISBN: 9783540662709. URL: https://books.google.co.za/books?id=8YugVtom1y4C.

Smith, Lelanie et al. (Nov. 2011). "An interactive boundary layer modelling methodology for aerodynamic flows." In:

Štorch, Vıt and J Nožička (2015). "On viscous-inviscid interaction for boundary layer calculation using two-equation integral method". In: *Studentská tvrčı činnost 2015*.

Swafford, T. W. (1983). "Analytical approximation of two-dimensional separated turbulent boundary-layer velocity profiles". In: *AIAA Journal* 21.6, pp. 923–926. DOI: 10.2514/3.8177. eprint: https://doi.org/10.2514/3.8177. URL: https://doi.org/10.2514/3.8177.

Timmer, W. and R.P.J.O.M. Rooij (Jan. 2003). "Summary of the Delft University Wind Turbine Dedicated Airfoils". In: *Journal of Solar Energy Engineering-transactions of The Asme - J SOL ENERGY ENG* 125. DOI: 10.1115/1.1626129.

Tollmien, W. (1930). "Über die Entstehung der Turbulenz". In: *Vorträge aus dem Gebiete der Aerodynamik und verwandter Gebiete: Aachen 1929*. Ed. by A. Gilles, L. Hopf, and Th. v. Kármán. Berlin, Heidelberg: Springer Berlin Heidelberg, pp. 18–21. ISBN: 978-3-662-33791-2. DOI: 10.1007/978-3-662-33791-2_4. URL: https://doi.org/10.1007/978-3-662-33791-2_4.

Vaithiyanathasamy, Rajesh et al. (Jan. 2018). "A double wake model for interacting boundary layer methods". In: DOI: 10.2514/6.2018-0516.

Weyburne, David (Jan. 2020). *THE UNBOUNDED AND BOUNDED BOUNDARY LAYER MODELS FOR FLOW ALONG A WALL*.

# A. Appendix A

## A.1. XFOIL execution and implemented improvements

In this part of the report, a detailed view of how the improvements were implemented into XFOIL is given. It is also important to understand the procedure as described in Fig. 4.1. This figure gives the reader an idea of how XFOIL performs its calculations. The coding will be explained here. Something that is not explained in Fig. 4.1, is the source files that XFOIL uses to execute its calculations. XFOIL is created out of various source files, each with its own specific function. The source files under inspection are the 'xfoil.f' and the 'xoper.f' files. The 'xfoil.f' performs all of the XFOIL calculations. Subroutines and parameters are then called into this file to enable the calculation of polars like lift, drag and momentum coefficients. The 'xoper.f' file handles most of the potential flow calculations. This is the file from which the wake trajectory is calculated. The stream functions and the viscous calculation are also carried out in this file. Other source files, like the 'xpanel.f' source file, are used to perform the panel generation and manipulations.

In the proposed drag prediction improvements method, changes have been brought into the 'xfoil.f' source file. As mentioned, this is where polar predictions are calculated. Drela (1989) used the momentum thickness definition of drag, as described in Eqn. (2.82), and then applied the Squire-Young method, as described in Eqn. (2.81), to calculate the total drag of the airfoil at a downstream position in the wake (generally set at one chord length position behind the airfoil trailing edge).

For the implementation of the new proposed lift prediction approach, the source file 'xoper.f' is edited to account for a viscous wake trajectory. This process was sufficiently described by Fig. 4.1. Detailed descriptions will be provided here to better understand how the new approach is implemented in XFOIL.

### A.1.1. 'xfoil.f' with improved drag predictions method

The 'xfoil.f' source file is the governing file that brings all the other files and their calculations together. In this file, drag is calculated by recalling parameters, calculated by other source files, into this file. These parameters include the momentum thickness in the wake and trailing edge, described by 'THWAKE', the edge velocity in the wake, described by 'UEWAKE' and the shape factor at the trailing edge of the airfoil.

The subroutine 'CDCALC' is called upon to calculate the drag coefficient. During the editing of this file, it was noticed that FORTRAN does not allow for a long line and results in an incomplete line when the code is too long. Thus, the equation was broken up into smaller pieces to calculate the drag coefficient. The original drag coefficient calculation is commented out with standard FORTRAN practise with a letter 'c' and the start of the line, as seen in the source code below.

File Edit View Projects Bookmarks Sessions Tools Settings Help

Documents Projects Filesystem Browser

xfoil.f

```
1193
1194        SUBROUTINE CDCALC
1195        INCLUDE 'XFOIL.INC'
1196  C
1197        SA = SIN(ALFA)
1198        CA = COS(ALFA)
1199  C
1200        IF(LVISC .AND. LBLINI) THEN
1201  C----- set variables at the end of the wake
1202         THWAKE = THET(NBL(2),2)
1203         URAT   = UEDG(NBL(2),2)/QINF
1204         UEWAKE = (UEDG(NBL(2),2) * (1.0-TKLAM)/(1.0 - TKLAM*URAT**2))
1205         SHWAKE = DSTR(NBL(2),2)/THET(NBL(2),2)
1206  C
1207  C----- extrapolate wake to downstream infinity using Squire-Young relation
1208  C      (reduces errors of the wake not being long enough)
1209  C       Cd = 2.0*( THWAKE )*(UEWAKE/QINF)**(0.5*(5.0+SHWAKE))
1210
1211  c------- Ue/Uinf
1212          UETINF = (UEWAKE)/QINF
1213
1214  c------- g
1215          gCorVal = 0.4
1216  c------- H1
1217          ValH1 = 3.15 + (1.72/(SHWAKE-1))
1218
1219  c------- gH1
1220          gH1Val = gCorVal*ValH1
1221
1222  c------- gH1 - 1
1223          gH1Valmin1 = gH1Val-1.0
1224
1225  c------- (Ue/Uinf)(gH1 - 1)
1226          UEgH1min1 = UETINF * gH1Valmin1
1227
1228  c------- (Ue/Uinf)(gH1 - 1) -1
1229          Trm3 =(UEgH1min1-1.0)
1230
1231  c------- (1 - Ue/inf)
1232          Trm2 = 1.0-UETINF
1233
1234  c-------Improved Momentum Thickness
1235          THITTRY =  THWAKE * (1.0 + Trm2*Trm3)
1236
1237  c-------Improved total drag coefficient
1238          T_impr_Cd = 2.0 * THITTRY
1239
1240  c-------Improved Squire Young drag prediction
1241         CD = 2.0*(THITTRY)*( UETINF )**(0.5*(5.0+SHWAKE))
1242
1243         WRITE(*,2010) CD
1244   2010 FORMAT (' Improved Drag prediction:         ',  F9.5)
```

**Figure A.1.** XFOIL drag improvement code

The improved code is evident from line 1211 in Fig. A.1. The final equation for calculating the corrected drag prediction is found in line 1241 of Fig. A.1. No further editing of the code was necessary as a correction value was added to the equation. Eqn. (4.5) was also implemented into this code as this was given a value in XFOIL; rather, it was calculated in this formula each

time this equation was needed. It proved to be simple enough to add it into this part of the code and then assign it to a variable to use in this code.

### A.1.2. 'xoper.f' with improved lift predictions method

As previously mentioned, to improve upon the lift predictions of XFOIL Eqn. (2.72) was used to update the vorticity strengths of the airfoil. The figure below illustrates what was changed in the XFOIL to allow for this to happen.

```
2796  C============================================ LIFT IMPROVEMENTS ========================================
2797            SUBROUTINE SPECAL
2798  C---------------------------------
2799  C     Converges to specified alpha.
2800  C---------------------------------
2801        INCLUDE 'XFOIL.INC'
2802        REAL MINF_CLM, MSQ_CLM
2803        LOGICAL :: COQVISB
2804  C---- calculate surface vorticity distributions for alpha = 0, 90 degrees
2805         IF(.NOT.LGAMU .OR. .NOT.LQAIJ) CALL GGCALC
2806        COSA = COS(ALFA)
2807        SINA = SIN(ALFA)
2808        COQVISB = .FALSE.
2809  C---- superimpose suitably weighted  alpha = 0, 90  distributions
2810        DO 50 I=1, N
2811  C=========='IF' Condition to check if final value of SPECAL calculation is calculated
2812            IF(ABS(QVIS(I)) .GT. 0) THEN
2813              COQVISB = .TRUE.
2814            ELSE
2815              COQVISB = .FALSE.
2816            ENDIF
2817
2818          IF(.not. COQVISB) THEN
2819              GAM(I)   =  COSA*GAMU(I,1) + SINA*GAMU(I,2)
2820              GAM_A(I) = -SINA*GAMU(I,1) + COSA*GAMU(I,2)
2821          ELSE
2822              GAM(I) =  COSA*QINV(I) + SINA*QINV(I)
2823              GAM_A(I) = -SINA*QINV(I)+ COSA*QINV(I)
2824          ENDIF
2825  C=============================================================================================================
```

**Figure A.2.** XFOIL lift improvement code

The approach followed by Ramanujam and Ozdemir (2017) was to initially determine the solution with an inviscid wake. This is accomplished by including an 'IF' condition into the code, as can be seen in line 2818 in Fig. A.2. In line 2817 the existence of the viscous edge velocity is determined with another 'IF' condition.This condition checks if the corresponding viscous edge velocity exists by checking if a value greater than zero exists. If it does, it should be used to update the vorticity strengths, as seen in lines 2819 and 2820, and lines 2822 and 2823. This viscous edge velocity, QVIS(I), is used to determine whether the inviscid solution, QINV(I), exists. This was done because when the condition checks for the existence of QINV(I), no convergance is reached. Checking the QVIS(I) value will deliver the same result as checking for the QVIS(I), but it seems that checking for QVIS(I) results in less complications. This then means that the subroutine 'SPECAL' has to be run a second time to include the edge velocity.

This was achieved by adding code to the angle of attack declaration as illustrated by Fig. A.3 in line 464. This loop function then allows for the second recall of the subroutine 'SPECAL' (The same was done when a sequence of angle of attacks was specified).

From these two illustrations it becomes clear that when an angle of attack is prompted, the code is instructed to run a normal XFOIL program execution. This is where the inviscid wake is determined by the initial calculations. This is the first run in the 'Do' loop, The value of QINV(I) does not yet exist as this value is calculated later. The 'IF' condition then allows for standard XFOIL calculations. When the subroutine 'SPECAL' is completed, the program then continues to the subroutine 'VISCAL' to determine and calculate the viscous edge velocity. When this is completed, the 'DO' loop then goes into its final loop. At this point the value of

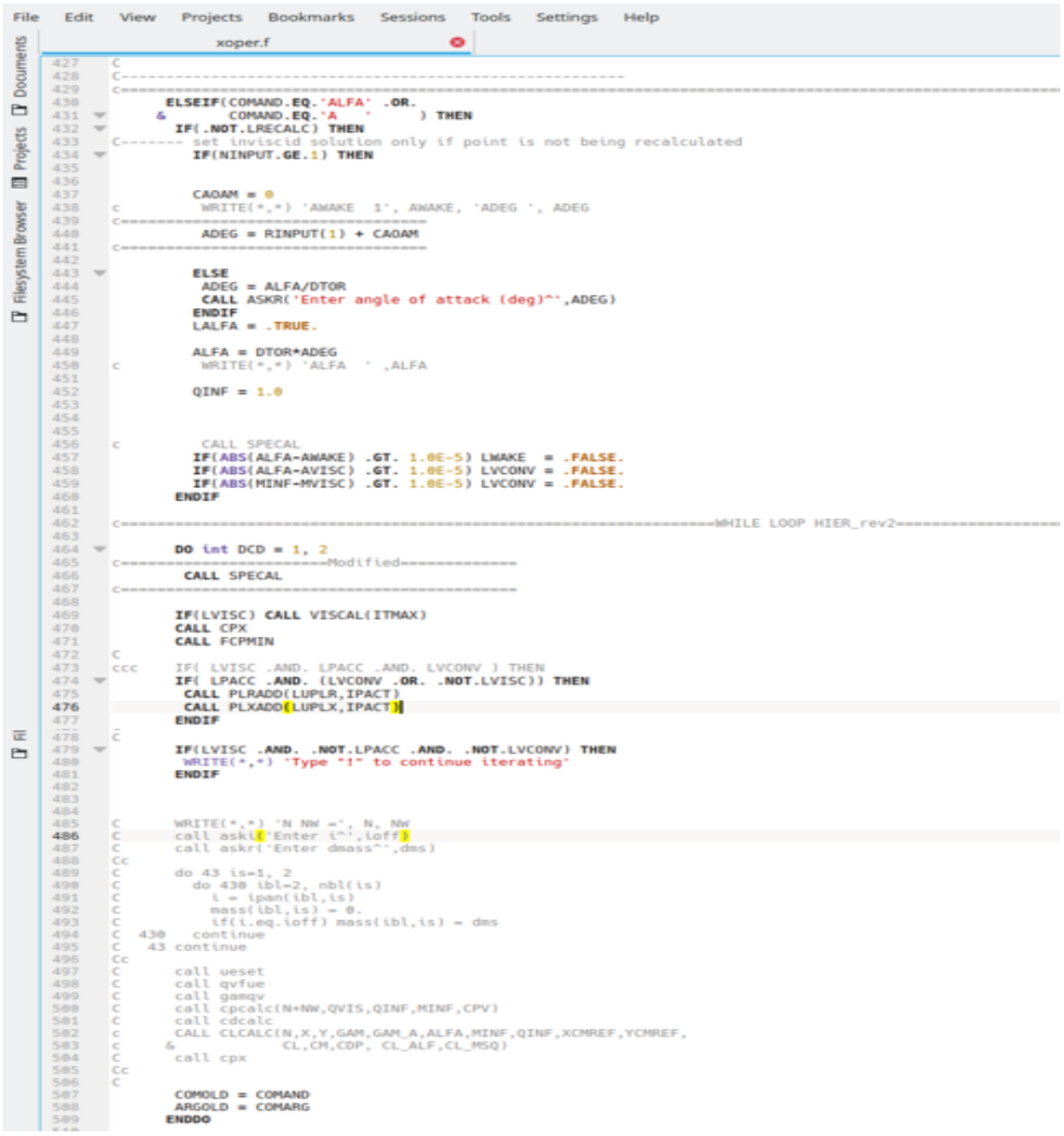


**Figure A.3.** XFOIL loop addition

QINV(I) exists for the same angle of attack at each I$^{th}$ position. The condition in line 2824 is then met. XFOIL then updates the vorticity strength with the edge velocity, QINV(I).

# B. Appendix B

## B.1. XFOIL validation data

### B.1.1. NACA0012 data

| AoA | 160 panels | | 200 panels | | 260 panels | | 300 panels | | 360 panels | |
|---|---|---|---|---|---|---|---|---|---|---|
| [deg] | Cl | Cd | Cl | Cd | Cl | Cd | Cl | Cd | Cl | Cd |
| 0 | 0 | 0,00509 | 0 | 0,00511 | 0 | 0,00512 | 0 | 0,00512 | 0 | 0,00512 |
| 1 | 0,112 | 0,00517 | 0,1119 | 0,00518 | 0,1119 | 0,00518 | 0,1118 | 0,00518 | 0,1118 | 0,00519 |
| 2 | 0,2234 | 0,00536 | 0,2233 | 0,00537 | 0,2232 | 0,00538 | 0,2232 | 0,00539 | 0,2231 | 0,00539 |
| 3 | 0,3337 | 0,00571 | 0,3336 | 0,00572 | 0,3335 | 0,00573 | 0,3335 | 0,00573 | 0,3334 | 0,00573 |
| 4 | 0,4428 | 0,00619 | 0,4427 | 0,00621 | 0,4426 | 0,00623 | 0,4425 | 0,00623 | 0,4424 | 0,00623 |
| 5 | 0,5503 | 0,0068 | 0,5503 | 0,00683 | 0,5503 | 0,00684 | 0,55 | 0,00685 | 0,5501 | 0,00684 |
| 6 | 0,6559 | 0,0075 | 0,6557 | 0,00753 | 0,6555 | 0,00753 | 0,6553 | 0,00754 | 0,6553 | 0,00754 |
| 7 | 0,7699 | 0,00831 | 0,769 | 0,00833 | 0,7674 | 0,00832 | 0,7679 | 0,00833 | 0,7676 | 0,00835 |
| 8 | 0,8956 | 0,00924 | 0,895 | 0,00924 | 0,8942 | 0,00926 | 0,8947 | 0,00928 | 0,8948 | 0,00927 |
| 9 | 1,0225 | 0,01024 | 1,0223 | 0,01027 | 1,0221 | 0,01029 | 1,022 | 0,0103 | 1,0218 | 0,0103 |
| 10 | 1,1177 | 0,01126 | 1,1174 | 0,01128 | 1,117 | 0,01132 | 1,1171 | 0,01132 | 1,1168 | 0,01135 |
| 11 | 1,2082 | 0,0124 | 1,2079 | 0,01243 | 1,2071 | 0,01249 | 1,2071 | 0,01248 | 1,207 | 0,01249 |
| 12 | 1,3009 | 0,01385 | 1,3013 | 0,01379 | 1,3008 | 0,01384 | 1,3008 | 0,01382 | 1,3005 | 0,01384 |

**Table B.1.** NACA 0012 panel sensitivity test

| AoA | Ncrit = 9 | | Ncrit = 11 | |
|---|---|---|---|---|
| [deg] | Cl | Cd | Cl | Cd |
| 0 | 0 | 0,00512 | 0 | 0,00473 |
| 1 | 0,1118 | 0,00519 | 0,1117 | 0,00479 |
| 2 | 0,2231 | 0,00539 | 0,2228 | 0,00499 |
| 3 | 0,3334 | 0,00573 | 0,3328 | 0,00536 |
| 4 | 0,4424 | 0,00623 | 0,4411 | 0,00594 |
| 5 | 0,5501 | 0,00684 | 0,5469 | 0,00665 |
| 6 | 0,6553 | 0,00754 | 0,6525 | 0,00744 |
| 7 | 0,7676 | 0,00835 | 0,7782 | 0,00836 |
| 8 | 0,8948 | 0,00927 | 0,909 | 0,00932 |
| 9 | 1,0218 | 0,0103 | 1,0318 | 0,01037 |
| 10 | 1,1168 | 0,01135 | 1,1165 | 0,01138 |
| 11 | 1,207 | 0,01249 | 1,2061 | 0,0126 |
| 12 | 1,3005 | 0,01384 | 1,2996 | 0,01395 |

**Table B.2.** NACA 0012: Std XFOIL Ncrit value vs test conditions

### B.1.2. NACA $63_3$-418 data

| AoA | 160 panels | | 200 panels | | 260 panels | | 300 panels | | 360 panels | |
|---|---|---|---|---|---|---|---|---|---|---|
| [deg] | Cl | Cd | Cl | Cd | Cl | Cd | Cl | Cd | Cl | Cd |
| -6 | -0,35 | 0,00774 | -0,3505 | 0,00774 | -0,3511 | 0,00777 | -0,3513 | 0,00778 | -0,3516 | 0,00778 |
| -5 | -0,236 | 0,00678 | -0,2361 | 0,0068 | -0,2366 | 0,00682 | -0,2366 | 0,00682 | -0,2367 | 0,00685 |
| -4 | -0,1205 | 0,00573 | -0,1205 | 0,00573 | -0,1207 | 0,00575 | -0,1207 | 0,00575 | -0,1207 | 0,00576 |
| -3 | -0,0018 | 0,00531 | -0,0018 | 0,00531 | -0,002 | 0,00533 | -0,0019 | 0,00534 | -0,0019 | 0,00535 |
| -2 | 0,1178 | 0,00519 | 0,1179 | 0,0052 | 0,1176 | 0,00523 | 0,1178 | 0,00523 | 0,1177 | 0,00524 |
| -1 | 0,2375 | 0,00518 | 0,2376 | 0,00518 | 0,2374 | 0,00521 | 0,2375 | 0,00521 | 0,2375 | 0,00522 |
| 0 | 0,357 | 0,00522 | 0,3568 | 0,00525 | 0,3569 | 0,00525 | 0,3571 | 0,00526 | 0,357 | 0,00527 |
| 1 | 0,4761 | 0,00531 | 0,4761 | 0,00532 | 0,4759 | 0,00536 | 0,4761 | 0,00536 | 0,476 | 0,00536 |
| 2 | 0,5947 | 0,00544 | 0,5945 | 0,00547 | 0,5943 | 0,00549 | 0,5948 | 0,00549 | 0,5946 | 0,00551 |
| 3 | 0,7118 | 0,00566 | 0,7119 | 0,00568 | 0,7119 | 0,00569 | 0,7122 | 0,00571 | 0,7121 | 0,00572 |
| 4 | 0,8275 | 0,00596 | 0,8274 | 0,006 | 0,8277 | 0,00601 | 0,8281 | 0,00602 | 0,8281 | 0,00602 |
| 5 | 0,9397 | 0,00648 | 0,9398 | 0,00651 | 0,9402 | 0,00654 | 0,9407 | 0,00655 | 0,9407 | 0,00656 |
| 6 | 1,039 | 0,00781 | 1,0399 | 0,00783 | 1,041 | 0,00785 | 1,0419 | 0,00787 | 1,042 | 0,00788 |
| 7 | 1,1285 | 0,00954 | 1,1304 | 0,00956 | 1,1325 | 0,0096 | 1,134 | 0,00962 | 1,1343 | 0,00965 |
| 8 | 1,2114 | 0,01122 | 1,2145 | 0,01129 | 1,2184 | 0,01132 | 1,2205 | 0,01138 | 1,2219 | 0,01139 |
| 9 | 1,2794 | 0,0128 | 1,2876 | 0,01288 | 1,296 | 0,01295 | 1,3004 | 0,01299 | 1,3029 | 0,01303 |
| 10 | 1,3317 | 0,01452 | 1,3419 | 0,0146 | 1,3541 | 0,01462 | 1,3608 | 0,01464 | 1,3655 | 0,01468 |
| 11 | 1,3821 | 0,0169 | 1,3952 | 0,01693 | 1,409 | 0,01697 | 1,4167 | 0,01698 | 1,4236 | 0,01697 |

**Table B.3.** NACA 63,3-418 panel sensitivity test

| AoA | Ncrit = 9 | |
|---|---|---|
| [deg] | Cl | Cd |
| -6 | -0,3516 | 0,00778 |
| -5 | -0,2367 | 0,00685 |
| -4 | -0,1207 | 0,00576 |
| -3 | -0,0019 | 0,00535 |
| -2 | 0,1177 | 0,00524 |
| -1 | 0,2375 | 0,00522 |
| 0 | 0,357 | 0,00527 |
| 1 | 0,476 | 0,00536 |
| 2 | 0,5946 | 0,00551 |
| 3 | 0,7121 | 0,00572 |
| 4 | 0,8281 | 0,00602 |
| 5 | 0,9407 | 0,00656 |
| 6 | 1,042 | 0,00788 |
| 7 | 1,1343 | 0,00965 |
| 8 | 1,2219 | 0,01139 |
| 9 | 1,3029 | 0,01303 |
| 10 | 1,3655 | 0,01468 |
| 11 | 1,4236 | 0,01697 |

**Table B.4.** NACA 63,3-418: Std XFOIL Ncrit value

### B.1.3. FX61-163

| AoA | 160 panels | | 260 panels | | 360 panels | |
|---|---|---|---|---|---|---|
| [deg] | Cl | Cd | Cl | Cd | Cl | Cd |
| -5 | -0,1109 | 0,00972 | -0,1085 | 0,00963 | -0,1097 | 0,00977 |
| -4,5 | -0,054 | 0,00936 | -0,051 | 0,00928 | -0,0513 | 0,00934 |
| -4 | 0,0042 | 0,00888 | 0,0072 | 0,00877 | 0,0077 | 0,0086 |
| -3,5 | 0,0689 | 0,00725 | 0,0751 | 0,00685 | 0,0766 | 0,0066 |
| -3 | 0,1378 | 0,00598 | 0,1434 | 0,00592 | 0,1431 | 0,00597 |
| -2,5 | 0,1983 | 0,00595 | 0,2036 | 0,00595 | 0,2037 | 0,00598 |
| -2 | 0,2583 | 0,006 | 0,2634 | 0,00602 | 0,2638 | 0,00602 |
| -1,5 | 0,3178 | 0,00607 | 0,3234 | 0,00607 | 0,3233 | 0,0061 |
| -1 | 0,3764 | 0,00616 | 0,3829 | 0,00611 | 0,3829 | 0,00616 |
| -0,5 | 0,4359 | 0,00621 | 0,4415 | 0,00625 | 0,4425 | 0,00622 |
| 0 | 0,4951 | 0,00627 | 0,5014 | 0,00631 | 0,5012 | 0,00634 |
| 0,5 | 0,5534 | 0,00636 | 0,5608 | 0,00634 | 0,561 | 0,0064 |
| 1 | 0,6122 | 0,00644 | 0,6194 | 0,00644 | 0,6196 | 0,00647 |
| 1,5 | 0,6709 | 0,00652 | 0,6783 | 0,00653 | 0,6786 | 0,00654 |
| 2 | 0,7286 | 0,00667 | 0,7373 | 0,00662 | 0,7371 | 0,00667 |
| 2,5 | 0,7873 | 0,00668 | 0,7953 | 0,00673 | 0,7959 | 0,00672 |
| 3 | 0,8444 | 0,00682 | 0,8539 | 0,0068 | 0,8538 | 0,00685 |
| 3,5 | 0,9012 | 0,00699 | 0,9114 | 0,00696 | 0,9111 | 0,00702 |
| 4 | 0,9557 | 0,00731 | 0,9668 | 0,00727 | 0,9676 | 0,00726 |
| 4,5 | 1,0088 | 0,00777 | 1,0204 | 0,00775 | 1,0228 | 0,00758 |
| 5 | 1,0563 | 0,0086 | 1,073 | 0,00829 | 1,0751 | 0,00815 |
| 5,5 | 1,1015 | 0,00958 | 1,1233 | 0,00901 | 1,1262 | 0,00883 |
| 6 | 1,1432 | 0,01076 | 1,1685 | 0,01013 | 1,174 | 0,00972 |
| 6,5 | 1,1742 | 0,01257 | 1,2052 | 0,01184 | 1,2116 | 0,01138 |
| 7 | 1,2029 | 0,01434 | 1,2397 | 0,01361 | 1,2492 | 0,01293 |
| 7,5 | 1,2404 | 0,01539 | 1,2755 | 0,01511 | 1,2799 | 0,01485 |
| 8 | 1,2816 | 0,01608 | 1,314 | 0,01627 | 1,3155 | 0,01622 |
| 8,5 | 1,3142 | 0,0168 | 1,3553 | 0,01711 | 1,3564 | 0,01711 |

**Table B.5.** FX61-163 panel sensitivity test

| AoA | Ncrit = 9 | | Ncrit = 10,32 | |
|---|---|---|---|---|
| [deg] | Cl | Cd | Cl | Cd |
| -5 | -0,1097 | 0,00977 | -0,1091 | 0,00988 |
| -4,5 | -0,0513 | 0,00934 | -0,0515 | 0,00937 |
| -4 | 0,0077 | 0,0086 | 0,0096 | 0,00805 |
| -3,5 | 0,0766 | 0,0066 | 0,0802 | 0,00623 |
| -3 | 0,1431 | 0,00597 | 0,1429 | 0,00598 |
| -2,5 | 0,2037 | 0,00598 | 0,2033 | 0,00604 |
| -2 | 0,2638 | 0,00602 | 0,2631 | 0,00612 |
| -1,5 | 0,3233 | 0,0061 | 0,3227 | 0,0062 |
| -1 | 0,3829 | 0,00616 | 0,3822 | 0,00627 |
| -0,5 | 0,4425 | 0,00622 | 0,4415 | 0,00635 |
| 0 | 0,5012 | 0,00634 | 0,5007 | 0,00643 |
| 0,5 | 0,561 | 0,0064 | 0,5598 | 0,00651 |
| 1 | 0,6196 | 0,00647 | 0,6187 | 0,00659 |
| 1,5 | 0,6786 | 0,00654 | 0,6773 | 0,00666 |
| 2 | 0,7371 | 0,00667 | 0,7359 | 0,00676 |
| 2,5 | 0,7959 | 0,00672 | 0,7943 | 0,00684 |
| 3 | 0,8538 | 0,00685 | 0,8524 | 0,00694 |
| 3,5 | 0,9111 | 0,00702 | 0,9101 | 0,00707 |
| 4 | 0,9676 | 0,00726 | 0,9665 | 0,00727 |
| 4,5 | 1,0228 | 0,00758 | 1,0224 | 0,00755 |
| 5 | 1,0751 | 0,00815 | 1,0748 | 0,00807 |
| 5,5 | 1,1262 | 0,00883 | 1,1264 | 0,00869 |
| 6 | 1,174 | 0,00972 | 1,1738 | 0,00959 |
| 6,5 | 1,2116 | 0,01138 | 1,2123 | 0,01117 |
| 7 | 1,2492 | 0,01293 | 1,2492 | 0,01293 |
| 7,5 | 1,2799 | 0,01485 | 1,2821 | 0,01447 |
| 8 | 1,3155 | 0,01622 | 1,3125 | 0,01616 |
| 8,5 | 1,3564 | 0,01711 | 1,3524 | 0,01708 |

**Table B.6.** FX61-163: Std XFOIL Ncrit value vs test conditions

### B.1.4. FX66-S-196

| AoA | 160 panels | | 200 panels | | 260 panels | | 300 panels | | 360 panels | |
|---|---|---|---|---|---|---|---|---|---|---|
| [deg] | Cl | Cd | Cl | Cd | Cl | Cd | Cl | Cd | Cl | Cd |
| -6 | -0,1931 | 0,00953 | -0,1933 | 0,00953 | -0,1943 | 0,00955 | -0,195 | 0,00956 | -0,1953 | 0,00956 |
| -5 | -0,0831 | 0,00873 | -0,0839 | 0,00874 | -0,0843 | 0,00872 | -0,0849 | 0,00874 | -0,0848 | 0,00872 |
| -4 | 0,0253 | 0,00766 | 0,0255 | 0,00761 | 0,0245 | 0,00751 | 0,0242 | 0,00748 | 0,0243 | 0,00744 |
| -3 | 0,1341 | 0,00616 | 0,1339 | 0,00621 | 0,1343 | 0,00623 | 0,1347 | 0,00623 | 0,135 | 0,00626 |
| -2 | 0,2524 | 0,0063 | 0,2526 | 0,0063 | 0,2527 | 0,00631 | 0,253 | 0,00634 | 0,2532 | 0,00634 |
| -1 | 0,3694 | 0,00638 | 0,3697 | 0,00642 | 0,3701 | 0,00641 | 0,3707 | 0,00642 | 0,3714 | 0,00643 |
| 0 | 0,4872 | 0,00645 | 0,4876 | 0,00649 | 0,488 | 0,00649 | 0,4886 | 0,00651 | 0,4893 | 0,00653 |
| 1 | 0,6041 | 0,00657 | 0,6042 | 0,00659 | 0,6046 | 0,00664 | 0,6052 | 0,00665 | 0,6062 | 0,00664 |
| 2 | 0,7193 | 0,00679 | 0,7202 | 0,00673 | 0,7215 | 0,00675 | 0,7222 | 0,00674 | 0,7228 | 0,00678 |
| 3 | 0,8355 | 0,00684 | 0,8361 | 0,00685 | 0,8364 | 0,00692 | 0,8377 | 0,00691 | 0,8388 | 0,0069 |
| 4 | 0,9493 | 0,00701 | 0,95 | 0,00707 | 0,9517 | 0,00705 | 0,9522 | 0,00711 | 0,9539 | 0,00708 |
| 5 | 1,0626 | 0,00719 | 1,0634 | 0,00723 | 1,0653 | 0,00724 | 1,0659 | 0,00729 | 1,0678 | 0,00728 |
| 6 | 1,1742 | 0,00734 | 1,1744 | 0,00744 | 1,1663 | 0,00741 | 1,1789 | 0,00743 | 1,1805 | 0,00745 |
| 7 | 1,2769 | 0,00784 | 1,2838 | 0,00767 | 1,2859 | 0,00771 | 1,2885 | 0,00769 | 1,2912 | 0,00768 |
| 8 | 1,2909 | 0,01081 | 1,3567 | 0,00928 | 1,3494 | 0,00977 | 1,3562 | 0,00966 | 1,3726 | 0,00917 |
| 9 | 1,2492 | 0,01574 | 1,3127 | 0,01378 | 1,3008 | 0,0149 | 1,3116 | 0,01481 | 1,3185 | 0,01499 |

**Table B.7.** FX66-S-196 panel sensitivity test

| AoA | Ncrit = 9 | | Ncrit = 10,32 | |
|---|---|---|---|---|
| [deg] | Cl | Cd | Cl | Cd |
| -6 | -0,1953 | 0,00956 | -0,1954 | 0,00952 |
| -5 | -0,0848 | 0,00872 | -0,0856 | 0,0086 |
| -4 | 0,0243 | 0,00744 | 0,021 | 0,00693 |
| -3 | 0,135 | 0,00626 | 0,1349 | 0,00629 |
| -2 | 0,2532 | 0,00634 | 0,2532 | 0,00639 |
| -1 | 0,3714 | 0,00643 | 0,371 | 0,00653 |
| 0 | 0,4893 | 0,00653 | 0,4891 | 0,0066 |
| 1 | 0,6062 | 0,00664 | 0,6063 | 0,00672 |
| 2 | 0,7228 | 0,00678 | 0,7229 | 0,00687 |
| 3 | 0,8388 | 0,0069 | 0,8389 | 0,00699 |
| 4 | 0,9539 | 0,00708 | 0,9542 | 0,00715 |
| 5 | 1,0678 | 0,00728 | 1,0681 | 0,00735 |
| 6 | 1,1805 | 0,00745 | 1,1807 | 0,0075 |
| 7 | 1,2912 | 0,00768 | 1,292 | 0,00768 |
| 8 | 1,3726 | 0,00917 | 1,3894 | 0,00839 |
| 9 | 1,3185 | 0,01499 | 1,3851 | 0,01237 |

**Table B.8.** FX66-S-196: Std XFOIL Ncrit value vs test conditions

### B.1.5. E603

| AoA | 160 panels | | 200 panels | | 260 panels | | 300 panels | | 360 panels | |
|---|---|---|---|---|---|---|---|---|---|---|
| [deg] | Cl | Cd | Cl | Cd | Cl | Cd | Cl | Cd | Cl | Cd |
| -3 | 0,1009 | 0,01015 | 0,099 | 0,00997 | 0,098 | 0,0099 | 0,0966 | 0,00969 | 0,0958 | 0,00953 |
| -1 | 0,328 | 0,00755 | 0,3281 | 0,00755 | 0,329 | 0,00764 | 0,3293 | 0,00765 | 0,2102 | 0,00718 |
| 0 | 0,4423 | 0,00841 | 0,4437 | 0,00835 | 0,4455 | 0,00833 | 0,4465 | 0,00837 | 0,3303 | 0,00769 |
| 1 | 0,561 | 0,00853 | 0,5627 | 0,00848 | 0,5648 | 0,00841 | 0,5655 | 0,00837 | 0,5666 | 0,00836 |
| 2 | 0,679 | 0,00864 | 0,6805 | 0,00845 | 0,6823 | 0,0085 | 0,6828 | 0,00845 | 0,6845 | 0,00845 |
| 3 | 0,7949 | 0,00853 | 0,7962 | 0,00856 | 0,7986 | 0,00855 | 0,8 | 0,00855 | 0,8018 | 0,00853 |
| 4 | 0,9088 | 0,0086 | 0,9107 | 0,00864 | 0,914 | 0,00864 | 0,9149 | 0,00858 | 0,9159 | 0,00859 |
| 5 | 1,0207 | 0,00872 | 1,0231 | 0,00873 | 1,0259 | 0,00868 | 1,0274 | 0,00868 | 1,0297 | 0,00869 |
| 6 | 1,1298 | 0,00884 | 1,1322 | 0,00881 | 1,1353 | 0,00884 | 1,1369 | 0,00882 | 1,1397 | 0,00882 |
| 7 | 1,2224 | 0,00937 | 1,2271 | 0,00928 | 1,2338 | 0,0093 | 1,2368 | 0,00927 | 1,2421 | 0,00922 |
| 8 | 1,2819 | 0,01059 | 1,284 | 0,0108 | 1,2951 | 0,01088 | 1,3029 | 0,01088 | 1,3158 | 0,01066 |
| 9 | 1,289 | 0,01341 | 1,2841 | 0,0141 | 1,308 | 0,01384 | 1,3205 | 0,01371 | 1,3423 | 0,01329 |

**Table B.9.** E603 panel sensitivity test

| AoA | Ncrit = 10,32 | | Ncrit = 9 | |
|---|---|---|---|---|
| [deg] | Cl | Cd | Cl | Cd |
| -3 | 0,0948 | 0,00898 | 0,0958 | 0,00953 |
| -2,5 | 0,1519 | 0,00726 | 0,1502 | 0,00813 |
| -2 | 0,2123 | 0,00738 | 0,2102 | 0,00718 |
| -1,5 | 0,2728 | 0,0077 | 0,27025 | 0,007435 |
| -1 | 0,3319 | 0,00804 | 0,3303 | 0,00769 |
| -0,5 | 0,3902 | 0,00839 | 0,3892 | 0,00796 |
| 0 | 0,4476 | 0,00884 | 0,4477 | 0,00834 |
| 0,5 | 0,5073 | 0,00883 | 0,5075 | 0,00833 |
| 1 | 0,5677 | 0,00887 | 0,5666 | 0,00836 |
| 1,5 | 0,6257 | 0,00887 | 0,6254 | 0,00841 |
| 2 | 0,6853 | 0,00893 | 0,6845 | 0,00845 |
| 2,5 | 0,7436 | 0,00894 | 0,7433 | 0,0085 |
| 3 | 0,8033 | 0,00898 | 0,8018 | 0,00853 |
| 3,5 | 0,86 | 0,00896 | 0,8589 | 0,00855 |
| 4 | 0,9168 | 0,00897 | 0,9159 | 0,00859 |
| 4,5 | 0,9738 | 0,00899 | 0,9729 | 0,00863 |
| 5 | 1,0307 | 0,00902 | 1,0297 | 0,00869 |
| 5,5 | 1,086 | 0,00902 | 1,085 | 0,00873 |
| 6 | 1,1405 | 0,00906 | 1,1397 | 0,00882 |
| 6,5 | 1,1939 | 0,00913 | 1,1931 | 0,00895 |
| 7 | 1,2448 | 0,00927 | 1,2421 | 0,00922 |
| 7,5 | 1,2889 | 0,00968 | 1,2798 | 0,00993 |
| 8 | 1,3295 | 0,01024 | 1,3158 | 0,01066 |
| 8,5 | 1,3545 | 0,01118 | 1,3322 | 0,01177 |
| 9 | 1,3647 | 0,01255 | 1,3423 | 0,01329 |

**Table B.10.** E603: Std XFOIL Ncrit value vs test conditions

# C. Appendix C

## C.1. Improved XFOIL prediction data

### C.1.1. NACA 63,3-418

| NACA 63,3-418 | | | | | |
|---|---|---|---|---|---|
| Experimental data | | | Improved method (Ncrit 9) | | |
| AoA | Cl | Cd | AoA | Cl | Cd |
| 9 | 1,241 | 0,01544 | 9 | 1,2936 | 0,0151 |
| 8 | 1,1619 | 0,01268 | 8 | 1,2168 | 0,01312 |
| 7 | 1,0741 | 0,00992 | 7 | 1,1318 | 0,0111 |
| 6 | 0,9892 | 0,00789 | 6 | 1,0406 | 0,00914 |
| 5 | 0,87068 | 0,00721 | 5 | 0,9398 | 0,00768 |
| 4 | 0,76449 | 0,00669 | 4 | 0,8276 | 0,00703 |
| 3 | 0,6583 | 0,00633 | 3 | 0,7117 | 0,00664 |
| 2 | 0,5314 | 0,00612 | 2 | 0,5944 | 0,00636 |
| 1 | 0,4134 | 0,006 | 1 | 0,4758 | 0,00617 |
| 0 | 0,29540 | 0,00591 | 0 | 0,3569 | 0,00604 |
| -1 | 0,18086 | 0,00589 | -1 | 0,2374 | 0,00597 |
| -2 | 0,06862 | 0,00602 | -2 | 0,1176 | 0,00599 |
| -3 | -0,044235 | 0,00617 | -3 | -0,0019 | 0,00609 |
| -4 | -0,16259 | 0,006909 | -4 | -0,1207 | 0,00653 |
| -5 | -0,28095 | 0,00784 | -5 | -0,2366 | 0,00767 |
| -6 | -0,3993 | 0,00886 | -6 | -0,3512 | 0,0087 |
| -7 | -0,5072 | 0,00956 | -7 | -0,465 | 0,00957 |
| -8 | -0,6151 | 0,01023 | -8 | -0,5774 | 0,01042 |
| -9 | -0,723 | 0,01112 | -9 | -0,6873 | 0,01135 |
| -10 | -0,82853 | 0,01253 | -10 | -0,7933 | 0,01245 |
| -11 | -0,93118 | 0,01471 | -11 | -0,8936 | 0,01378 |
| -12 | -1,0072 | 0,01805 | -12 | -0,9854 | 0,01543 |

**Table C.1.** Improved method predictions: NACA63,3-418

### C.1.2. FX 61-163

| FX 61-163 | | | | | | | | |
|---|---|---|---|---|---|---|---|---|
| Experimental data | | | Improved method (Ncrit 9) | | | Improved method (Ncrit 10.32) | | |
| AoA | Cl | Cd | AoA | Cl | Cd | AoA | Cl | Cd |
| 10 | 1,3691 | 0,01523 | 10 | 1,4615 | 0,02177 | 10 | 1,4503 | 0,02195 |
| 9 | 1,3391 | 0,01301 | 9 | 1,4239 | 0,01801 | 9 | 1,4223 | 0,01787 |
| 8 | 1,2842 | 0,01091 | 8 | 1,357 | 0,01488 | 8 | 1,3603 | 0,01449 |
| 7 | 1,2039 | 0,00965 | 7 | 1,2808 | 0,01186 | 7 | 1,2837 | 0,0115 |
| 6 | 1,1158 | 0,00898 | 6 | 1,1855 | 0,00998 | 6 | 1,1857 | 0,00988 |
| 5 | 1,0169 | 0,00847 | 5 | 1,0791 | 0,00895 | 5 | 1,0791 | 0,00887 |
| 4 | 0,9100 | 0,00808 | 4 | 0,9677 | 0,00826 | 4 | 0,967 | 0,00829 |
| 3 | 0,8042 | 0,00766 | 3 | 0,8534 | 0,00784 | 3 | 0,8523 | 0,00791 |
| 2 | 0,6953 | 0,00722 | 2 | 0,7368 | 0,00754 | 2 | 0,7358 | 0,00764 |
| 1 | 0,5856 | 0,00706 | 1 | 0,6194 | 0,00729 | 1 | 0,6188 | 0,00741 |
| 0 | 0,4648 | 0,00701 | 0 | 0,5015 | 0,00708 | -1 | 0,3824 | 0,007 |
| -1 | 0,3485 | 0,00702 | -1 | 0,383 | 0,00689 | -2 | 0,2633 | 0,00683 |
| -2 | 0,2302 | 0,00680 | -2 | 0,2639 | 0,00674 | -3 | 0,1433 | 0,00667 |
| -3 | 0,1137 | 0,00704 | -3 | 0,1433 | 0,00668 | -3,5 | 0,0811 | 0,00688 |
| -3,5 | 0,05281 | 0,007572 | -3,5 | 0,0786 | 0,00718 | -4 | 0,0116 | 0,00845 |
| -4 | -0,0088 | 0,00914 | -4 | 0,0091 | 0,00917 | -5 | -0,1081 | 0,01068 |
| -5 | -0,1342 | 0,01046 | -5 | -0,1086 | 0,01063 | | | |

**Table C.2.** Improved method predictions: FX 61-163

### C.1.3. FX66-S-196

| FX66-S-196 | | | | | | | | |
|---|---|---|---|---|---|---|---|---|
| Experimental data | | | Improved method (Ncrit 9) | | | Improved method (Ncrit 10.32) | | |
| AoA | Cl | Cd | AoA | Cl | Cd | AoA | Cl | Cd |
| 11 | 1,33382 | 0,01529 | 11 | 1,26 | 0,03894 | 11 | 1,2656 | 0,03777 |
| 10 | 1,42031 | 0,01316 | 10 | 1,2801 | 0,02893 | 10 | 1,3138 | 0,02593 |
| 9 | 1,46532 | 0,01078 | 9 | 1,298 | 0,01923 | 9 | 1,3588 | 0,01577 |
| 8 | 1,38813 | 0,00968 | 8 | 1,3627 | 0,01132 | 8 | 1,3812 | 0,01047 |
| 7 | 1,28931 | 0,00928 | 7 | 1,2868 | 0,00937 | 7 | 1,2851 | 0,00946 |
| 6 | 1,18827 | 0,00885 | 6 | 1,1766 | 0,00897 | 6 | 1,1757 | 0,00906 |
| 5 | 1,08267 | 0,00837 | 5 | 1,0649 | 0,00864 | 5 | 1,0645 | 0,00871 |
| 4 | 0,9742 | 0,00824 | 4 | 0,9514 | 0,00832 | 4 | 0,9513 | 0,00839 |
| 3 | 0,86572 | 0,00836 | 3 | 0,8369 | 0,00804 | 3 | 0,8368 | 0,00811 |
| 2 | 0,75725 | 0,00835 | 2 | 0,7214 | 0,00781 | 2 | 0,7211 | 0,00791 |
| 1 | 0,64877 | 0,00777 | 1 | 0,6048 | 0,00764 | 1 | 0,605 | 0,00771 |
| 0 | 0,5375 | 0,00766 | 0 | 0,4881 | 0,00745 | 0 | 0,4881 | 0,00753 |
| -1 | 0,42591 | 0,00755 | -1 | 0,3708 | 0,00732 | -1 | 0,3705 | 0,00739 |
| -2 | 0,31432 | 0,00744 | -2 | 0,2527 | 0,00722 | -2 | 0,2526 | 0,00726 |
| -3 | 0,20273 | 0,00751 | -3 | 0,1344 | 0,00712 | -3 | 0,1346 | 0,00715 |
| -4 | 0,09115 | 0,00839 | -4 | 0,0242 | 0,00836 | -4 | 0,021 | 0,00781 |
| -5 | -0,02044 | 0,0096 | -5 | -0,0845 | 0,0097 | -5 | -0,0851 | 0,00958 |

**Table C.3.** Improved method predictions: FX66-S-196

### C.1.4. Eppler603 (E603)

| E603 | | | | | | | | |
|---|---|---|---|---|---|---|---|---|
| Experimental data | | | Improved method (Ncrit 9) | | | Improved method (Ncrit 10.32) | | |
| AoA | Cl | Cd | AoA | Cl | Cd | AoA | Cl | Cd |
| 11 | 1,3278 | 0,01429 | 11 | 1,3851 | 0,02892 | 11 | 1,3827 | 0,02847 |
| 10 | 1,3215 | 0,014 | 10 | 1,3861 | 0,02035 | 10 | 1,4009 | 0,01925 |
| 9 | 1,2964 | 0,01304 | 9 | 1,3849 | 0,01463 | 9 | 1,3957 | 0,01417 |
| 8 | 1,2133 | 0,0113 | 8 | 1,3367 | 0,01208 | 8 | 1,3407 | 0,012 |
| 7 | 1,1428 | 0,01078 | 7 | 1,246 | 0,01097 | 7 | 1,2459 | 0,01115 |
| 6 | 1,04608 | 0,01033 | 6 | 1,1404 | 0,01045 | 6 | 1,1397 | 0,01075 |
| 5 | 0,9464 | 0,01007 | 5 | 1,0301 | 0,01017 | 5 | 1,0304 | 0,01055 |
| 4 | 0,84106 | 0,00985 | 4 | 0,9169 | 0,00998 | 4 | 0,9176 | 0,01043 |
| 3 | 0,72061 | 0,00976 | 3 | 0,8023 | 0,00985 | 3 | 0,8029 | 0,01036 |
| 2 | 0,62263 | 0,00971 | 2 | 0,6853 | 0,00972 | 2 | 0,6855 | 0,01027 |
| 1 | 0,50986 | 0,00963 | 1 | 0,5675 | 0,00961 | 1 | 0,5677 | 0,0102 |
| 0 | 0,39487 | 0,00942 | 0 | 0,4481 | 0,0095 | 0 | 0,4483 | 0,0101 |
| -1 | 0,28965 | 0,00909 | -1 | 0,3309 | 0,00886 | -1 | 0,3323 | 0,00931 |
| -2 | 0,16122 | 0,00865 | -2 | 0,2109 | 0,00824 | -2 | 0,213 | 0,0085 |
| -2,5 | 0,10651 | 0,0085 | -2,5 | 0,1507 | 0,00819 | -2,5 | 0,1526 | 0,00831 |
| -3 | 0,05298 | 0,00901 | -3 | 0,0933 | 0,0101 | -3 | 0,0929 | 0,00925 |

**Table C.4.** Improved method predictions: E603

# D. Appendix D: Separation of flow study

As recognised from Chapter 2, the numerical method of flow prediction has limitations in predicting flow separation. Drela (1989) stated that separation bubbles have steep gradients in $U_e$ and $\theta$ at reattachment that result in jumps $\delta u_e$ and $\delta\theta$. An equation to relate these jumps is obtained by integrating the integral momentum equation over a small streamwise distance.

$$\frac{\Delta\theta}{\theta} = -(2 + H - M_e^2)\frac{\Delta u_e}{u_e} \tag{D.1}$$

This method was validated by Drela (1989) and deemed a reliable and relatively accurate method to predict separation and transition. Separation is characterised by an initial flattening of the $U_e$ or $c_p$ curve before a steep declining gradient that indicates reattachment. This investigation was done on the original version of XFOIL.

## D.1. NACA $6_3$3-418

As mentioned, the NACA $6_3$3-418 airfoil has a camber of 2% at 35% of $x/c$ and thickness of 18%. The current investigation is to check for flow separation at the trailing edge, which may indicate where XFOIL is less robust or accurate in these flow conditions due to the collapse of the Kutta condition and other singularities that may arise.

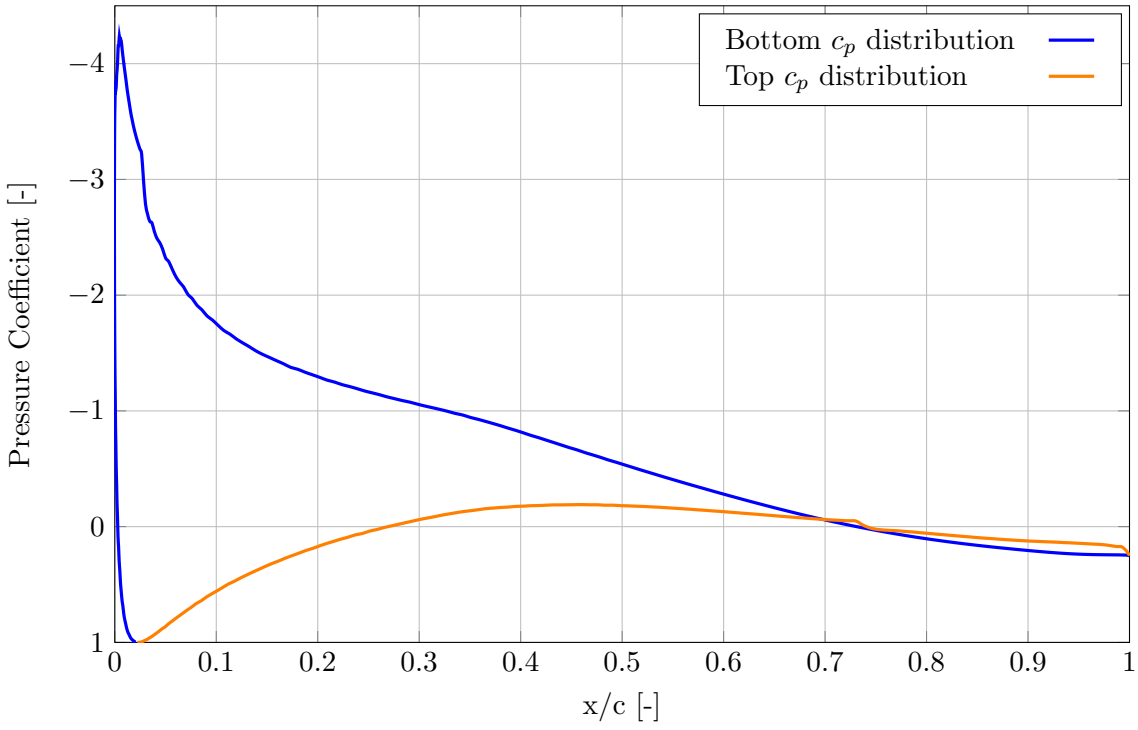


**Figure D.1.** NACA $63_3$-418 $C_p$ distribution with $N_{crit} = 9$ and Re = $3{\times}10^6$ at -10°

Fig. D.1 shows the XFOIL analysis of the pressure coefficient distribution at -10° with compressible flow conditions and $N_{crit} = 9$. At this angle of attack separation is more likely to occur, considering the bottom $c_p$ distribution. One can observe that from $x/c = 0.55$ the curve starts to flatten out. This is even clearer at $x/c = 0.9$, with reference to the top, which shows reattachment at the trailing edge flow, with a steep decline in the $c_p$ curve at the trailing edge. This suggests that the flow at the bottom of the trailing edge is nearing flow separation. This is even more evident when considering the XFOIL rendering of the flow around the airfoil (Fig. D.3) which shows a large displacement of the flow. Flow separation can also be identified by a skin friction coefficient ($C_f$) equal to zero. From Fig. D.2, it is clear that from -10° flow separation is becoming more apparent with full flow separation at the trailing edge at -12°. At x/c = 0.9 with $\alpha$ = -10°, the skin friction coefficient is very close to zero, indicating that the airflow at that location is nearing separation due to the slowing down of the air nearing circulation conditions. These conditions show that the onset of flow separation is reached.

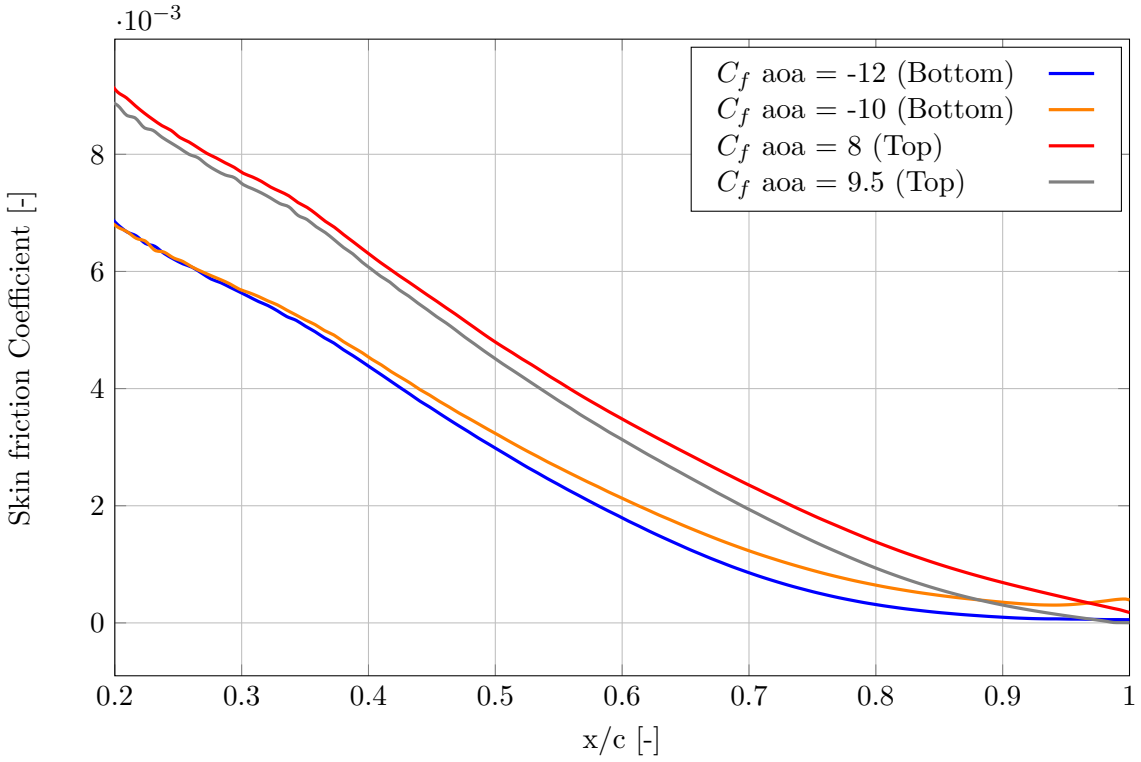


**Figure D.2.** NACA $63_3$-418 $C_f$ distribution with $N_{crit} = 9$ and Re = $3{\times}10^6$

When considering the case of an angle of attack of 8°, one can observe the onset of flow separation at the trailing edge, on the top of the airfoil. This is evident from Fig. D.4, with the flattening of the curve occurring at this location. One can note that reattached flow has occurred at the bottom at the trailing edge with a steep gradient.

This is even further confirmed when considering Fig. D.2. Here the onset of flow separation is observed at $-10°$, with full flow separation reached at an angle of attack of 9.5° where $C_f = 0$

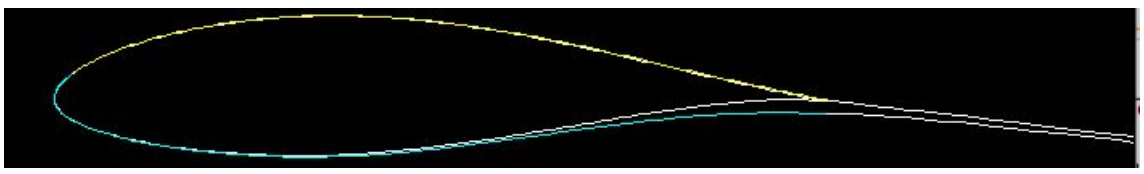

**Figure D.3.** XFOIL rendering of the flow around the NACA $63_3$-418 at $Re = 3 \times 10^6$

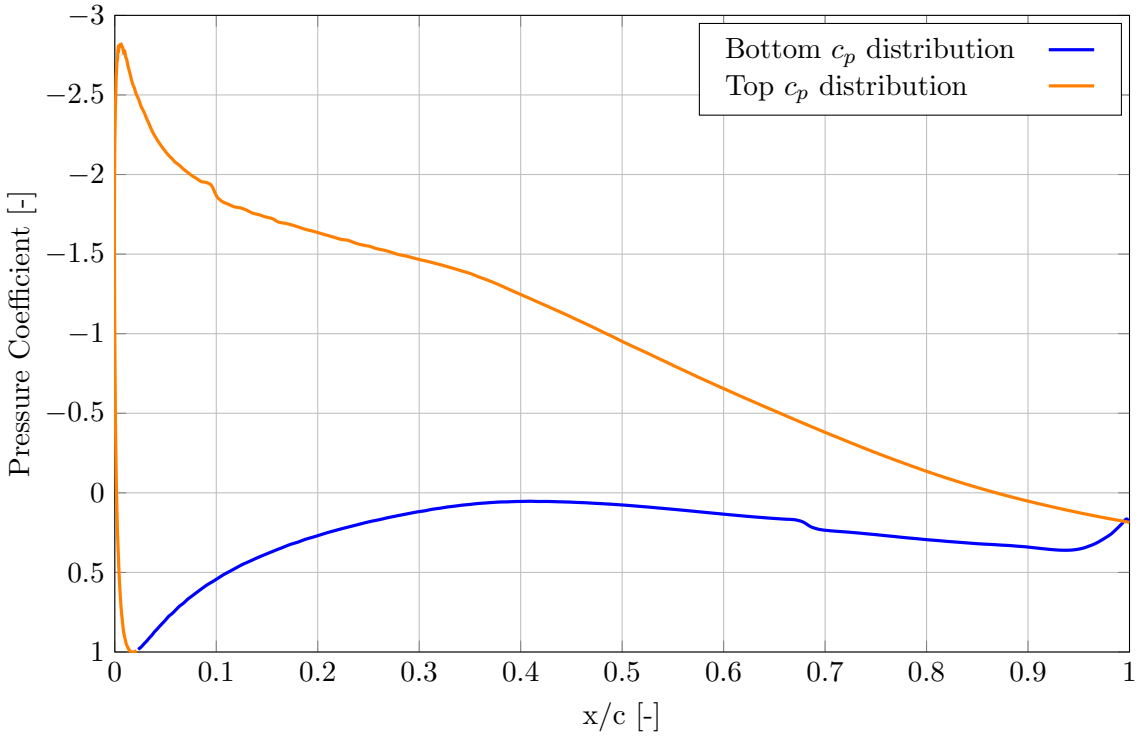


**Figure D.4.** NACA $63_3$-418 $C_p$ distribution with $N_{crit} = 9$ and Re = $3{\times}10^6$ at 8°

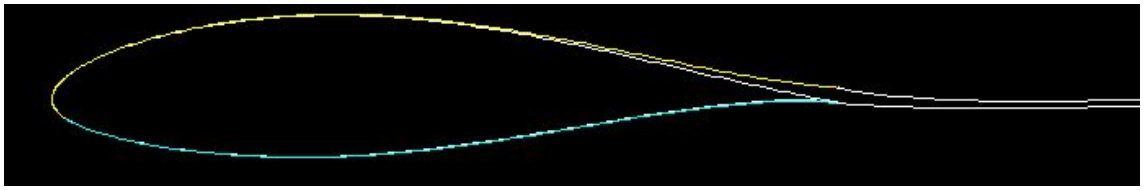

**Figure D.5.** XFOIL rendering of the flow around the NACA $63_3$-418 at $Re = 3 \times 8^6$

starting from x/c = 0.98.

## D.2. FX61-163

This study was completed to comment on the flow presence at the trailing edge of the current airfoil. An XFOIL anaylsis was completed at $Re = 1,5 \times 10^6$ with $N_{crit} = 10.32$. The analysis was done at 5 angle of attack increments, to investigate the point of onset of flow separation, ranging from attached to separated flow conditions. Consider Fig. D.6 below for the results of the analysis.

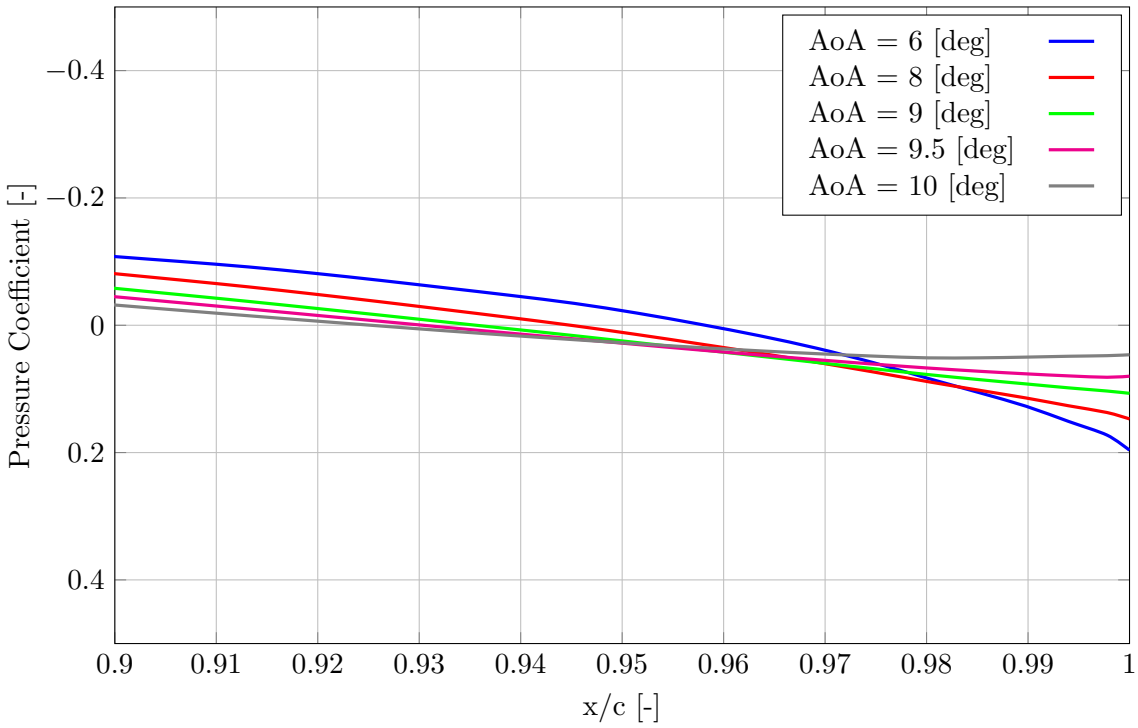


**Figure D.6.** FX61-163 top surface $C_p$ distribution with $N_{crit} = 10.32$ and Re = $1.5 \times 10^6$

From Fig. D.6, it is evident that flow separation is present and becomes more apparent with the increase in angle of attack. At an angle of 6° the flow is attached to the surface at the trailing edge. From 9.5°, the onset of flow separation is observed with fully-detached flow at 10°. Also note that at an angle of 10°, separation occurs and can be observed from Fig. D.7, with the value of $C_f = 0$ at x/c = 0.985.

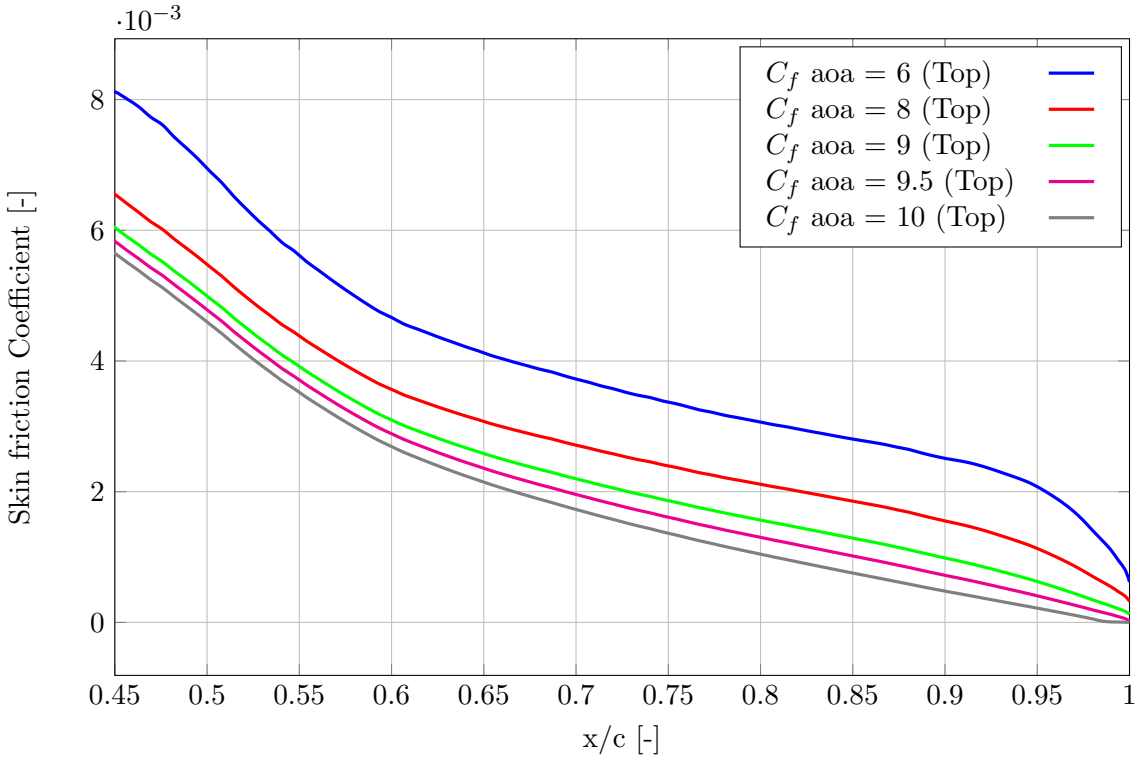


**Figure D.7.** FX61-163 top surface $C_f$ distribution with $N_{crit} = 10.32$ and Re = $1.5{\times}10^6$